Cr-tolerance of the IT-SOFC $La(Ni,Fe)O_3$ material

Maciej K. Stodolny

Cover
The cover shows digitally processed SEM micrograph of the $La(Ni,Fe)O_3$ (LNF) porous layer used in solid oxide fuel cells (SOFCs). The orange area in this micrograph represents the Cr-intrusion into the LNF material (black area) after exposure to Cr-poisoning conditions. The Cr-incorporation into the LNF perovskite and its consequences is the main theme of this thesis.

Ph.D. committee

Chairman and Secretary
Prof. dr. G. van der Steenhoven (University of Twente)

Promotor
Prof. dr. ing. D. H. A. Blank (University of Twente)

Assisent-promotor
Dr. B. A. Boukamp (University of Twente)
Dr. F. P. F. van Berkel (Energy research Centre of the Netherlands)

Members
Prof. dr. ing. E. Ivers-Tiffée (Karlsruhe Institute of Technology)
Prof. dr. J. T. S. Irvine (University of St Andrews)
Prof. dr. J. Schoonman (Technical University Delft)
Prof. dr. ing. L. Lefferts (University of Twente)
Dr. H. J. M. Bouwmeester (University of Twente)

The research presented in this thesis was carried out within the SOFC group, Hydrogen and Clean Fossil Fuels unit at the Energy research Centre of the Netherlands (ECN) in cooperation with the Inorganic Materials Science group, Department of Science and Technology, MESA+ Institute for Nanotechnology at the University of Twente, the Netherlands.

Maciej K. Stodolny
Cr-tolerance of the IT-SOFC $La(Ni,Fe)O_3$ material
Ph.D. thesis University of Twente, Enschede, the Netherlands.

ISBN: 978-90-365-3358-4
DOI: 10.3990/1.9789036533584
URL: http://dx.doi.org/10.3990/1.9789036533584
Printed by Off Page, Amsterdam, The Netherlands

Cr-TOLERANCE OF THE IT-SOFC $La(Ni,Fe)O_3$ MATERIAL

DISSERTATION

to obtain
the degree of doctor at the University of Twente,
on the authority of the rector magnificus,
prof. dr. H. Brinksma,
on account of the decision of the graduation committee,
to be publicly defended
on Wednesday May 16^{th}, 2012 at 12.45 hrs

by

Maciej Krzysztof Stodolny

born on June 8^{th}, 1984
in Sokolka, Poland

This dissertation has been approved by:

Prof. dr. ing. D. H. A. Blank (promotor)

Dr. B. A. Boukamp (assistent-promotor)

Dr. F. P. F. van Berkel (assistent-promotor)

Contents

Thesis highlights

$La(Ni,Fe)O_3$ stability in the presence of chromia – A solid-state reactivity study (Chapter 2)

Published in: *Journal of The Electrochemical Society* **158** (2) B112-B116 (2011)
ECS Transactions **25** (2) 2915-2922 (2009)

Highlights:

- $LaNi_{0.6}Fe_{0.4}O_3$ (LNF) is chemically unstable at 800°C when exposed to a direct contact with Cr_2O_3:
  - Cr-cations enters the perovskite phase, replacing first Ni- and then Fe-cations
  - the perovskite transforms from the rhombohedral to an orthorhombic symmetry on the exchange of Ni and Fe with Cr

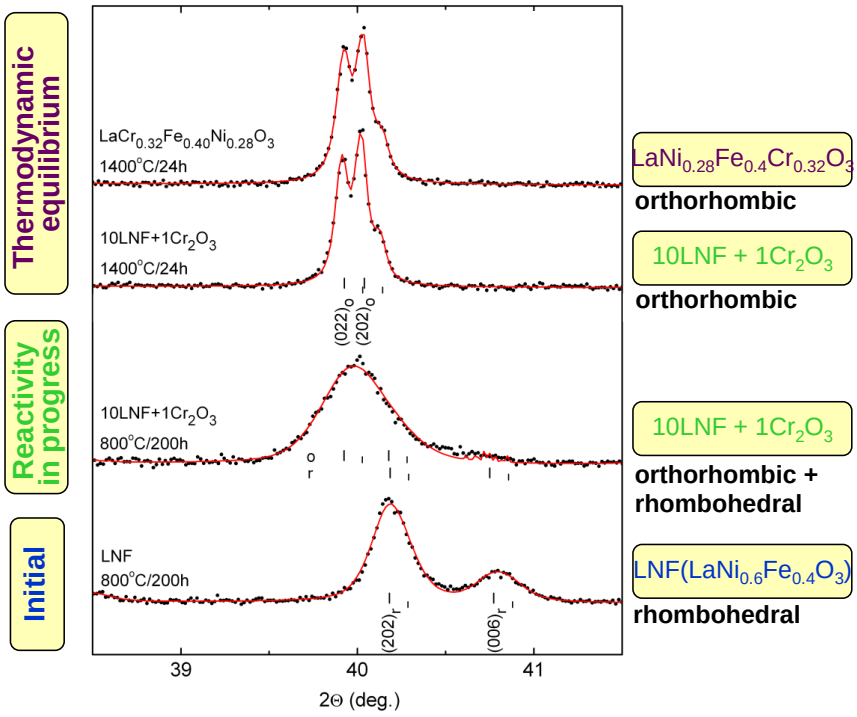

Impact of Cr-poisoning on the conductivity of $LaNi_{0.6}Fe_{0.4}O_3$ (Chapter 3)

Published in: *Journal of Power Sources* **196** 9290-9298 (2011) – **Key Scientific Article** (*Renewable Energy Global Innovations*) *ECS Transactions* **35** (1) 2035-2043 (2011)

Highlights:

- Cr vapor species poison $LaNi_{0.6}Fe_{0.4}O_3$ (LNF) at IT-SOFC operating temperatures (600-800°C)
- The Cr-attack results in a replacement of Ni by Cr in the LNF perovskite lattice
- The Cr-rich phase transforms from a rhombohedral to an orthorhombic crystal structure
- The drop in the electronic conductivity of LNF is due to formation of a low-conductive Cr-rich phase
- The Cr-poisoning impact on the LNF conductivity is smaller at 600°C than at 800°C

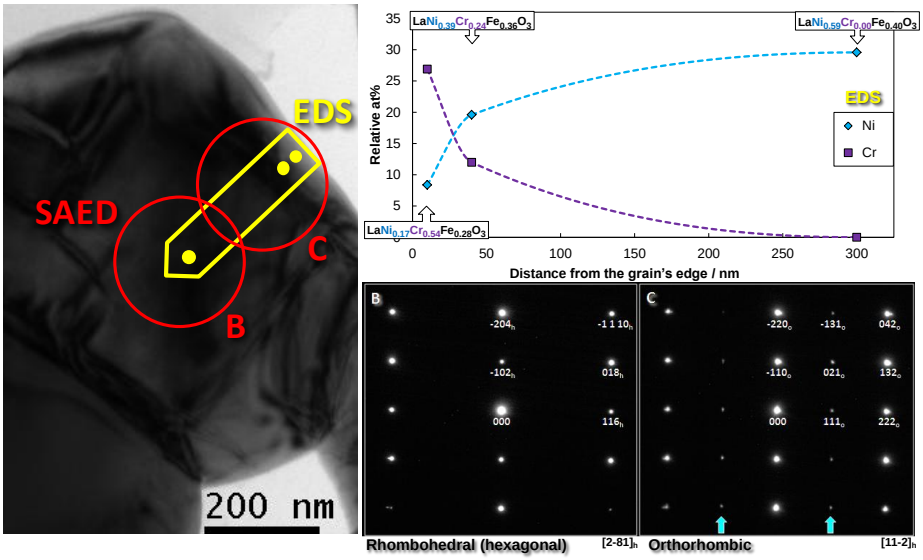

Impact of Cr-poisoning on the conductivity of different $LaNi_{0.6}Fe_{0.4}O_3$ cathode microstructures (Chapter 4)

Published in: *Solid State Ionics* (accepted for publication, DOI: 10.1016/j.ssi.2012.04.004)

Highlights:

- Cr vapor species directly react with different $LaNi_{0.6}Fe_{0.4}O_3$ (LNF) cathode microstructures
- The increase of layer resistance and Cr content is dependent on the microstructure of the LNF layer
- The Cr-poisoning impact is more severe for microstructures with finer particles

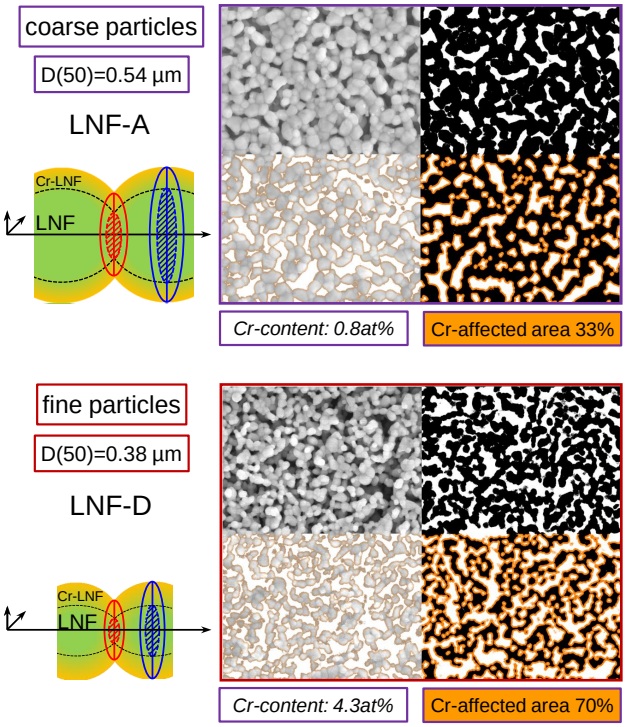

Cr-poisoning of a $LaNi_{0.6}Fe_{0.4}O_3$ cathode under current load (Chapter 5)

Published in: *Journal of Power Sources* **209C** 120-129 (2012)

Highlights:

- Volatile Cr-species cause degradation of $LaNi_{0.6}Fe_{0.4}O_3$ (LNF) cathodes under current load conditions
- Overpotential and impedance increase is due to reaction of $LaNi_{0.6}Fe_{0.4}O_3$ and $Gd_{0.4}Ce_{0.6}O_{1.8}$ (GDC) with Cr
- Cr-reactivity is chemically- and electrochemically-driven
- R_{ohmic} increases due to both the drop in LNF conductivity and the loss in GDC ionic transport
- R_{pol} increases due to the loss of LNF electrochemical activity at the triple phase boundary (TPB)

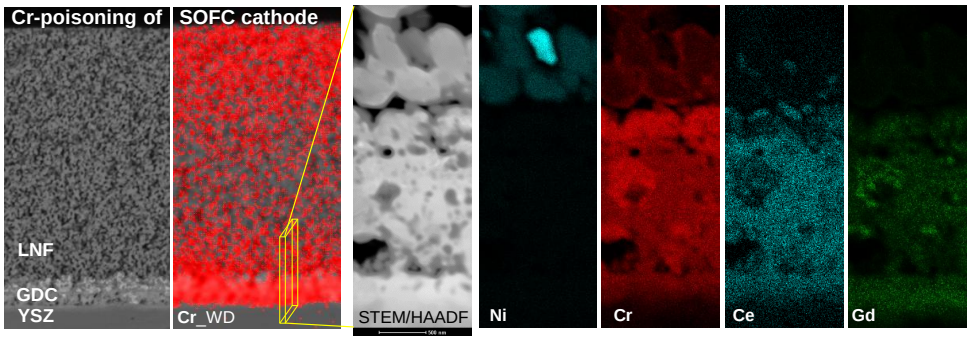

1 Introduction

I. Background

1.1 Preface

Over the last decades, the growth in world population (exceeding 7 billion of human beings! [1]) has led to an increasing interest in flexible electricity production together with the necessity for introduction of decentralized, more efficient and clean power systems [2, 3].

Fuel cells (FCs) have emerged as a possible next generation power system, having both high efficiency and environmental-friendly operation. The higher electrical efficiency of FCs compared to combustion engines [2–4], may help to reduce dependence on fossil fuels and considerably diminish emissions into the atmosphere. FCs can especially help to reduce emissions of greenhouse gases like CO_2, since FCs generate electricity through electrochemical reactions, without burning fossil fuel.

Among all types of FCs, solid oxide fuel cells (SOFCs) have a good potential for being used as the stationary stand-alone power generation systems. SOFCs are particularly suitable in the power range of 1-200 kW_e [5, 6], due to their high energy conversion efficiency which can reach up to 65% [7]. In addition, SOFCs have other advantages such as silent working, lack of moving parts, multi-fuel capability (apart from hydrogen, also including methane and biogas), very low level of NO_x and SO_x emissions, and a relative simplicity of system design. Furthermore, the exhaust is sufficiently high in temperature to be used as an effective heat source for various processes. The possibility of the co-generation of electricity and heat can lead to a further increase in the overall efficiency approaching 80% [8]. This has been demonstrated by Siemens-Westinghouse and Sulzer-HEXIS for decentralized Combined Heat and Power (CHP) units.

An essential step towards SOFCs commercialization is a reduction of the operating temperature from 1000°C to the intermediate regime of 600-800°C [2, 3]. This is also referred to as intermediate-temperature SOFC, IT-SOFC. Lower operating temperature can improve SOFC stability and reliability, and also reduce the production costs. This can be mainly achieved by using cost-effective chromia-forming ferritic stainless steels as interconnects and other constructing elements. However, Cr-poisoning, caused by evaporating Cr from such metallic interconnects, has been

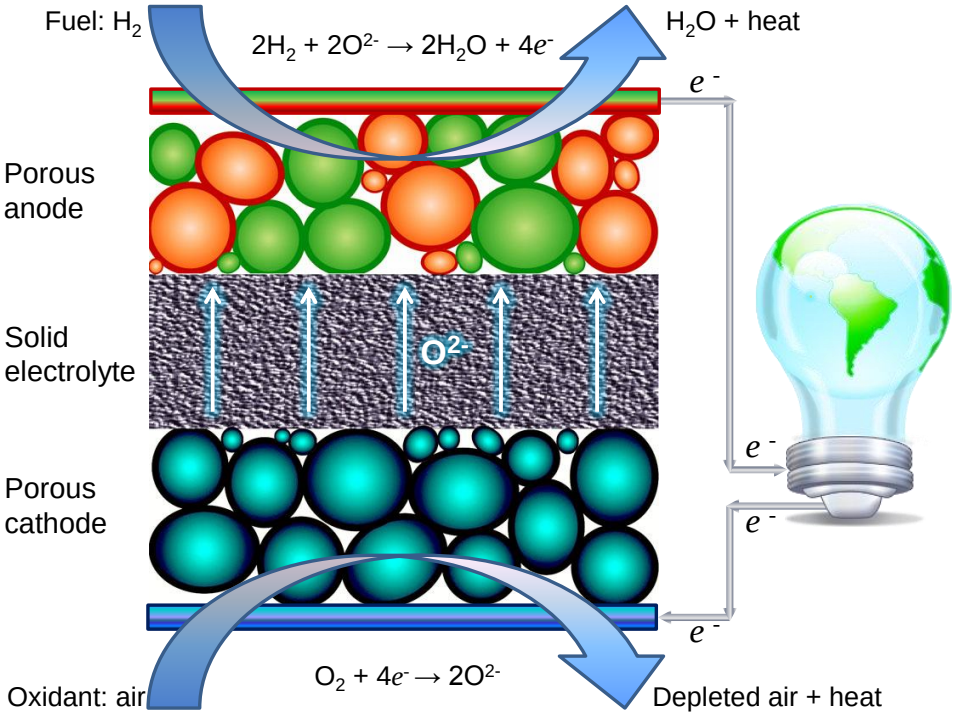

Figure 1.1: Solid Oxide Fuel Cell - principle of operation.

identified as very detrimental for the functioning of the state-of-the-art (SoA) SOFC cathodes. This resulted in performance degradation [9–13], impeding the required 40,000 hours operation of the IT-SOFC system.

Recently it has been proposed that Cr-poisoning can be suppressed by using Cr-resistant cathodes [11, 14–16]. However, the actual Cr-tolerance of the proposed cathode materials is debatable and controversial [17].

Investigation on the impact of Cr-poisoning on the claimed Cr-resistant cathode materials will be the main theme of this thesis.

1.2 Solid Oxide Fuel Cell - principle of operation

The basic structure of all fuel cells (including SOFC) is similar and relatively simple: a cell consists of two electrodes which are connected via external circuit and are separated by an ion-conducting material - the electrolyte. The electrodes have a porous structure and are gas permeable to allow diffusion of reactants at high rates without mass transfer limitations [2–4, 6].

The operating principle of an SOFC is shown schematically in Fig. 1.1. In SOFCs the solid electrolyte can conduct oxide ions. The fuel (e.g. hydrogen or simple hy-

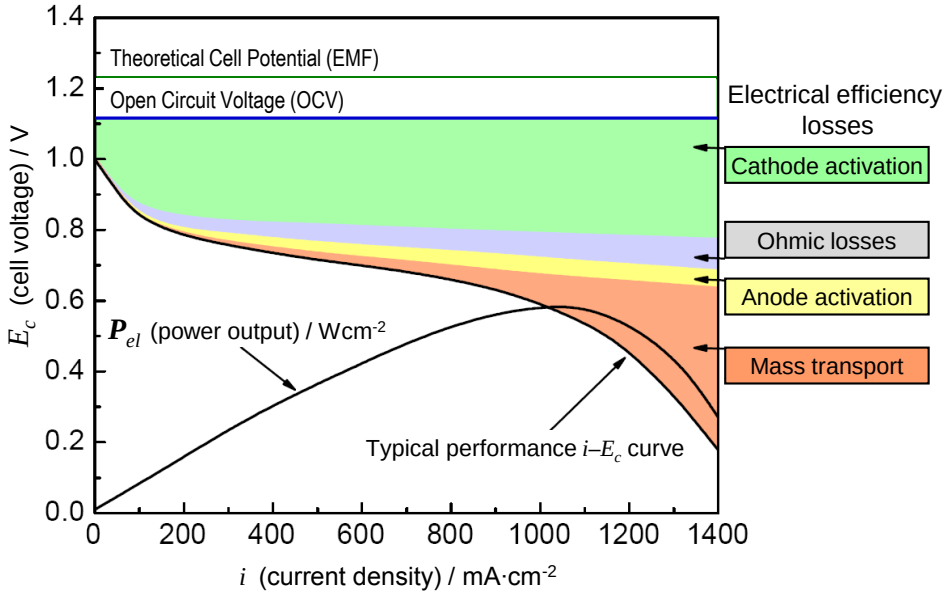

Figure 1.2: A current-voltage curve characterizing the performance of an SOFC.

drocarbons like methane) is oxidized at the fuel electrode - anode, according to:

$$2H_2 \leftrightarrow 4H^+ + 4e^-, \tag{1.1}$$

whereas the oxidant i.e. oxygen is reduced at the porous air electrode - cathode, according to:

$$O_2 + 4e^- \leftrightarrow 2O^{2-}. \tag{1.2}$$

The difference in the oxygen activity of two gases (oxidant and fuel) at both electrodes (cathode and anode) provides a driving force for motion of the oxide ions in the solid electrolyte. Oxide ions, formed by a dissociation of oxygen at the cathode under electron consumption (Eq. 1.2), migrate through the electrolyte to the anode in response to the activity gradient (chemical potential, or partial pressure) of oxygen. To complete the reaction, oxygen ions react with hydrogen to form water. The overall SOFC reaction can be thus presented as:

$$2H_2 + O_2 \rightarrow 2H_2O + P_{el} + Q_{heat}, \tag{1.3}$$

where P_{el} represents an electrical power output and Q_{heat} denotes a useful exhaust heat [3, 4, 6].

Further increase in the overall efficiency of the SOFC system can be obtained by combining the electrical power output P_{el}, defined as $P_{el} = E_c \cdot i$ where E_c is a cell voltage and i is a current density, with the useful exhaust heat Q_{heat}.

Cell voltage, E_c, characterizes the performance of the fuel cell under operation (i.e. the electrical power output P_{el} at a given current load). Under current load conditions, E_c is lower than the theoretical electromotive force (EMF) or reversible (thermodynamic) cell voltage E_r which is defined by Nernst Equation [3, 4, 6]:

$$E_r = \frac{RT}{4F} ln \left(\frac{P_{O_2(cathode)}}{P_{O_2(anode)}} \right) = E^0 + \frac{RT}{4F} ln \left(\frac{P_{O_2(cathode)} P^2_{H_2(anode)}}{P^2_{H_2O(anode)}} \right) \tag{1.4}$$

where R is the gas constant, T - temperature, F - the Faraday constant, P - partial pressure of O_2, H_2 or H_2O at the given electrode, and E^0 - EMF at the standard pressure and temperature.

The cell voltage E_c under loading conditions is then expressed as:

$$E_c = E_r - iR_{tot} - \eta \tag{1.5}$$

where R_{tot} is the total internal cell resistance and η is the polarization loss (overpotential) at the electrodes. The term iR_{tot} is associated with ohmic losses and can be attributed to activation polarization (of both anode and cathode) and to concentration polarization (due to mass transport) [3].

A schematic representation of a current-voltage curve with marked regions of the different contributions of polarization losses is presented in Fig. 1.2. It is evident that cathode activation is the main contributor to loss of electrical efficiency in SOFCs [3]. Therefore, any detrimental impact of Cr-poisoning on the performance of the cathode is of great significance for the long-term stability of SOFCs.

1.3 SOFC composition and configuration

During the last few decades of the research into SOFC systems, the composition and the configuration of the cell has evolved significantly [2–4, 6]. Fig. 1.3 shows schematically the evolution in SOFC research on the flat plate (planar) cell design [4, 6]. The first generation (*Gen* 1) of SOFC was based on an electrolyte-supported cell (thick yttria stabilized zirconia - YSZ) operated at high temperature, circa 1000°C (HT-SOFC). As electrodes a cermet anode Ni+YSZ and a composite cathode (La,Sr)MnO_3+YSZ (LSM+YSZ) were used [4, 6]. The second generation of SOFCs (*Gen* 2) was composed of an anode-supported cell (Ni+YSZ) with a thin YSZ electrolyte and a LSM+YSZ cathode [4, 6]. Further improvement of the anode-supported SOFC (*Gen* 2.5) included placement of a barrier layer (gadolinia doped ceria - GDC) between the YSZ electrolyte and the cathode material like (La,Sr)(Co,Fe)O_3 (LSCF) or (La,Sr)CoO_3 (LSC). The anode-supported SOFC configuration enables operation at intermediate temperatures of 600-800°C (IT-SOFC) [4, 6]. Currently, the state-of-the-art (SoA) SOFC is the anode-supported Ni+YSZ/YSZ/GDC/LSCForLSC cell.

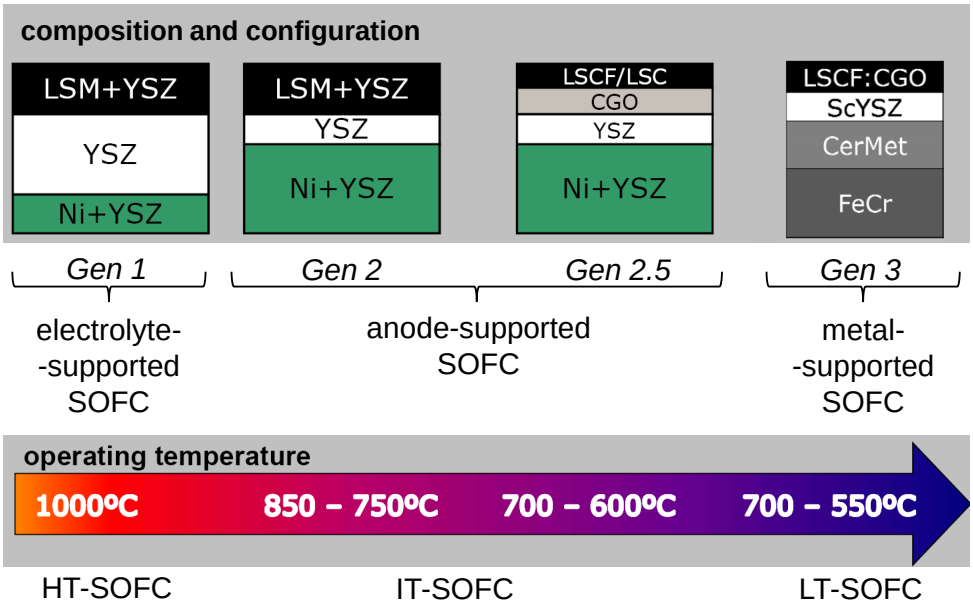

Figure 1.3: SOFC composition and configuration for high- (HT), intermediate- (IT) and low temperature (LT) applications.

The foreseen third generation of SOFC (*Gen* 3) would be composed of a metallic support, a cermet anode, a scandium doped YSZ electrolyte and a composite cathode LSCF:GDC (Fig. 1.3) operated at temperatures lower than 600°C [4, 6].

The SOFC system operated at HT and IT can be used as decentralized Combined Heat and Power (CHP) units for the stationary applications. The LT-SOFC can also enter new market segments, e.g. Auxiliary Power Units (APU) for a transportation market.

1.4 IT-SOFC stacks

To obtain high power output single cells are stacked on top of each other, separated by a metallic interconnect, forming an SOFC-stack. Out of many stack designs [ref], a concept for a cost-effective IT-SOFC planar stack design has been proposed by the Energy research Centre of the Netherlands (ECN) [18], as shown in Fig. 1.4. A relatively cost-efficient interconnect material such as chromia-forming ferritic stainless steel can be used to separate anode and cathode compartments. The requirements for being a suitable interconnect material include not only cost-effectiveness but also good workability, high corrosion resistance and a proper thermal expansion coefficient matching with all the other stack components [4, 6]. Corrugated Fe-Cr-alloyed metallic interconnect fulfills all these stringent requirements.

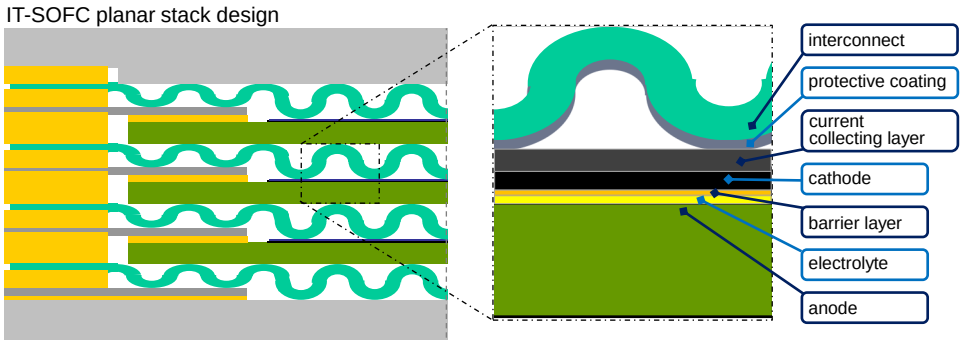

Figure 1.4: IT-SOFC stack assembly [18]

A drawback of the use of the ferritic stainless steels is the Cr evaporation from Fe-Cr interconnects resulting in Cr-poisoning of the SOFC cathodes, which leads to a serious performance deterioration (loss of the electrical power output P_{el}) [4, 6, 9–13].

1.5 Cr-poisoning of SOFC cathodes

To prevent the Cr-poisoning phenomenon one approach is to use protective coatings on the interconnects (Fig. 1.4) decreasing, and preferably preventing, Cr-vaporization [19–21]. However, taking into account required life-time of 40,000 hours and the possibility of spalling and formation of cracks within interconnect coating layers [19, 20] it seems that this approach should not be regarded as a sufficient solution to the Cr-poisoning issue.

The other approach is to improve the cathode material itself. The literature review presented below gives the status of Cr-poisoning affecting state-of-the-art SOFC cathodes and also gives proposals for new promising Cr-tolerant cathode compositions.

1.5.1 Cr-poisoning mechanism – general view

In the cathode compartment of the IT-SOFC-stack, the surface of the metallic interconnect oxidizes during operation. This results in formation of a Cr-oxide layer on top of the interconnect. Cr-species originating from this layer can migrate inside the cathode compartment along two paths: either through direct interconnect-cathode contact via solid-state diffusion (possibly surface diffusion) or through vapor phase transport of mainly $CrO_{3(g)}$ and/or $CrO_2(OH)_{2(g)}$ [10, 22].

Cr-species arriving through either mechanism at the cathode material have a detrimental effect on the functioning of the SOFC cathodes, particularly (La,Sr)MnO_3 (LSM) or (La,Sr)(Co,Fe)O_3 (LSCF). This leads to performance deterioration over time [9–13, 23–26]. However, so far no consensus has been reached in literature re-

garding the nature of Cr deposition and the interaction with the cathode materials. It has been proposed to be due to either (*i*) electrochemical deposition or (*ii*) chemical dissociation reaction.

The electrochemical Cr deposition i.e. electrochemical reduction of volatile Cr-species (*i*) has been reported to take place at triple phase boundary (TPB) or in the whole bulk of cathode material. The electrochemical deposition of volatile Cr-species at TPB competes with the O_2 reduction reaction (depending on the cathode overpotential and temperature [23]), thus is (partially) blocking the electrochemically active sites [27, 28]. The electrochemical deposition of Cr in whole bulk takes place via Cr substitution into the perovskite lattice [23]. Cr incorporation is slow at low temperatures [23, 29].

The Cr chemical dissociation reaction (*ii*), which is a non-electrochemical process, has been reported to be due to local low oxygen partial pressure near active sites (TPB) [10, 23, 24], which may be an indirect effect of the cathodic polarization [30]. Furthermore, Cr chemical deposition under no current load is random [27, 30] and is affected by thermodynamics and catalytic properties of the electrode material [30]. The observed distribution of Cr deposits at different locations (within cathode or/and far away) depends on the mobility of Cr-containing nuclei [30, 31]. Cr chemical deposition (*ii*) is controlled by the nucleation reaction between the nucleation agent and the gaseous Cr species [12, 13, 15]. The nature of the nucleation agent strongly depends on the electrode material and impurities [12, 13, 15].

1.5.2 New promising Cr-tolerant cathode

It has been suggested that the absence of the nucleation agents in the cathode composition could assure Cr tolerance [15]. The nucleation agents inducing Cr deposition discovered so far include: Mn^{2+} and SrO [12, 13, 15]. The search for Cr-tolerant materials was first reported on La(Ni,Fe)O_3 cathode material [11, 14, 15]. A particular composition of $LaNi_{0.6}Fe_{0.4}O_3$ (LNF), prepared intentionally without nucleating elements such as Mn, and/or Sr, showed no Cr deposition [14]. The authors concluded that LNF is stable against Cr vapors at 800°C [14]. No visible Cr deposition was found on the LNF electrode surface or at the LNF/YSZ interface [11]. Furthermore, very low reactivity of LNF with Cr_2O_3 powder has also been reported [11]. The reaction product $NiCr_2O_4$ was only observed if residual NiO reacts with Cr_2O_3 powder [11]. It has also been concluded that the deposition of Cr species on the LNF electrode is much smaller than that on the LSCF electrode [11]. However, thermodynamic calculations indicate that Cr vapors can react with LNF to be substituted into perovskites with NiO precipitation [29], though no experimental confirmation has been presented so far.

1.6 La(Ni,Fe)O_3: Cr-tolerant?

$LaNi_{0.6}Fe_{0.4}O_3$ material being reported as a Cr-tolerant cathode, together with its high electronic conductivity and a thermal expansion coefficient matching that of zirconia [32], is of great interest for a stable long-term cathode operation and thus could open the road towards rapid commercialization of the IT-SOFC-stacks. However, only short-term tests have been reported on the Cr-stability of LNF [11, 14–16]. Therefore, an endurance test of the LNF cathode was conducted at ECN [17] to evaluate the Cr-tolerance of the LNF cathode material.

Endurance testing, performed in a Cr-free all ceramic housing (Fig. 1.5), of an LNF cathode with an improved electrochemical performance [33] showed enhanced and stable long-term performance of the anode-supported SOFC (*Gen* 2.5) with such an optimized LNF cathode. However, endurance testing of the LNF cathode in combination with an uncoated metallic interconnect (Fig. 1.5) showed noticeable degradation in cell performance [17] raising questions of the actual Cr-tolerance of the LNF material.

A preliminary post-test analysis of the deteriorated cell revealed a considerable Cr accumulation in the LNF cathode, as shown in Fig. 1.6. A standard SEM-EDX elemental mapping of an embedded and polished cross-section of the anode-supported cell with the LNF cathode exposed to a metallic interconnect demonstrates that Cr was spread throughout the entire cathode thickness [17], indeed calling into question the actual Cr-tolerance of the LNF material.

Taking into account contradictory literature findings with ECN testing of the LNF cathode it seems that Cr-poisoning is a relatively complex phenomenon dependent on numerous variables and factors. Such a scientific enigma motivated and triggered further research on Cr-tolerance of the IT-SOFC La(Ni,Fe)O_3 material which became the main theme of the PhD research described in this thesis.

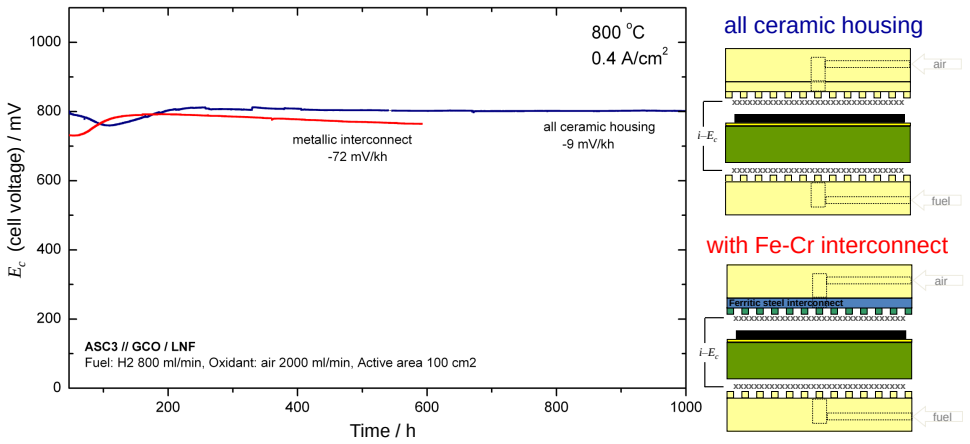

Figure 1.5: Endurance testing of the anode-supported SOFC with an LNF cathode performed in all ceramic housing and in the presence of a metallic interconnect.

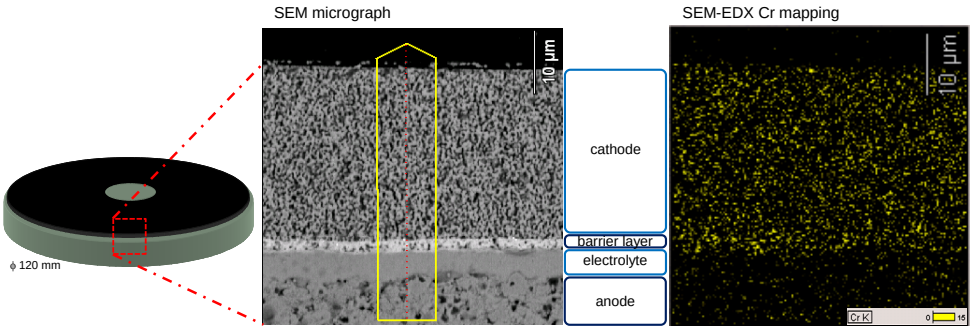

Figure 1.6: Preliminary post-test analysis of a Cr-poisoned LNF cathode.

1.7 Scope of the thesis

II. Aim

The research goal of this PhD is to understand the chemical stability of the LNF material in the presence of Cr species and ultimately provide a thorough understanding of the degradation mechanisms of the LNF cathode exposed to the Cr-poisoning conditions and recommend any feasible solution to the Cr-poisoning issue.

III. Approach and strategy

The perovskite $LaNi_{0.6}Fe_{0.4}O_3$ - LNF - can be considered for use as a current collecting layer, an interconnect protective coating and/or an electrochemically active SOFC cathode layer in an IT-SOFC-stack. Such a variety of LNF applications brings a challenge of a proper investigation of the possible interaction between LNF and Cr-species. Investigation complexity increases further taking into account that transport of Cr-species is known to take place along two paths: either through direct solid-state diffusion or through vapor phase transport.

Therefore, this investigation has been subdivided into two parts. Solid-state reactivity between LNF and chromia was investigated first (Chapter 2), followed by a study on the impact of volatile Cr-species on the LNF properties as a function of various environmental parameters (Chapter 3-5). To investigate whether Cr-deposition is electrochemical (*i*) or chemical (*ii*) in nature the impact of Cr-vapors was studied at OCV (Chapter 3-4) and at a current load (Chapter 5).

This approach is depicted in Fig. 1.7 on a schematic roadmap of the necessary research that was performed.

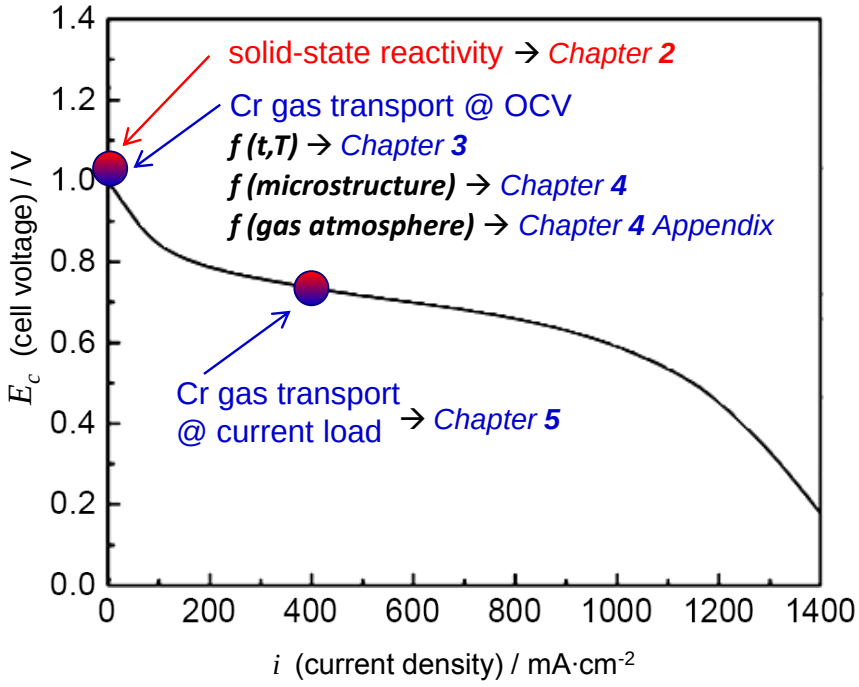

Figure 1.7: Roadmap of experiments and thesis scope.

2 La(Ni,Fe)O_3 stability in the presence of chromia – A solid-state reactivity study

The perovskite $LaNi_{0.6}Fe_{0.4}O_3$ (LNF) is a candidate material for an electrochemically active cathode layer, a cathode current collecting layer and/or an interconnect protective coating in intermediate temperature solid oxide fuel cells (IT-SOFC) operated at 600-800°C. Since these operating temperatures enable the use of relatively cheap interconnect materials such as chromia-forming ferritic stainless steel, investigation of the chemical stability of LNF in the presence of Cr-species is of importance. This study demonstrates that LNF is chemically unstable at 800°C when it is in direct contact with Cr_2O_3. It has been observed that Cr enters the perovskite phase, replacing first Ni and then Fe, already after 200 h. At 600°C, however, only minor reaction products were detected after 1000 h exposure to Cr_2O_3. Although this is a promising result, long-term testing under fuel cell operating conditions at 600°C is needed to prove that LNF is a viable IT−SOFC material.

Published in: *Journal of The Electrochemical Society* **158** (2) B112-B116 (2011)
ECS Transactions **25** (2) 2915-2922 (2009)

Presented at: 11^{th} International Symposium on SOFC, 216^{th} ECS Meeting; October 2009, Vienna, Austria (*talk*)
II Polish Forum - Fuel Cells and Hydrogen Technologies; September 2009, Kocierz, Poland (*talk*)

2.1 Introduction

For intermediate temperature solid oxide fuel cells (IT-SOFCs), chromia-forming ferritic stainless steels can be used as bipolar plates, enhancing ease of fabrication, workability and cost-effectiveness of the SOFC interconnects. However, the evaporation of Cr-oxide and oxy-hydroxide species from these metal separator plates in an oxygen-rich atmosphere is known to be highly detrimental to the functioning of common SOFC cathode materials such as $(La,Sr)MnO_3$ (LSM) or $(La,Sr)CoO_3$ (LSC) perovskite [9, 10]. This may be due to the poisoning of electrochemically active sites or the formation of secondary phases with low electrical conductivity.

It has recently been found that $La(Ni,Fe)O_3$-based cathodes have higher resistance to Cr-poisoning [11, 14]. Of particular interest is $La(Ni_{0.6}Fe_{0.4})O_3$ (LNF) which exhibits high electronic conductivity and a thermal expansion coefficient matching that of zirconia, a common SOFC electrolyte material [32]. Optimization of the microstructure of the LNF cathode, with respect to lateral conductivity and three phase boundaries at the electrode-electrolyte interface, has been shown to result in enhanced electrochemical performance [34]. However, recent endurance test data obtained at ECN on SOFCs with an LNF cathode at operating temperatures of 800-850°C, showed degradation in cell performance when tested in combination with a Cr containing metallic interconnect [17], despite the claimed Cr-resistance of LNF in the literature.

Besides its application as a cathode material, LNF can be used as a cathode current collecting layer and/or an interconnect coating. Therefore, a thorough understanding of the true extent of LNF chemical stability in the presence of Cr species is vital for its application in SOFC systems when ferritic steel interconnects are used. The transport of Cr-species is known to take place along two paths, through vapor phase transport or through solid-state diffusion [10, 22]. The present study deals with the solid-state reactivity between LNF and Cr_2O_3 in the IT-SOFC operating temperature range of 600-800°C. In addition, due to the gradient of the oxygen partial pressure throughout the cathode layer, caused by the applied overpotential under load, it is also important to investigate the reactivity at partial oxygen pressures lower than atmospheric. To this end, mixtures of LNF and Cr_2O_3 were heated at 600-800°C in a wide PO_2 range and possible changes in the phase composition of LNF were analyzed by means of X-ray diffraction (XRD).

2.2 Experimental

Powders of $La(Ni_{0.6}Fe_{0.4})O_3$ (Praxair, 99.9%) and Cr_2O_3 (Alfa Aesar, 99%) were used for the determination of the reactivity of Cr_2O_3 with $La(Ni_{0.6}Fe_{0.4})O_3$. The LNF raw material contained trace amounts of unreacted La_2O_3, which disappeared after heating at 800°C for 1 h in air. Therefore, this pretreated powder was used in all experiments reported below, and the abbreviation LNF, used below, refers to this pretreated powder.

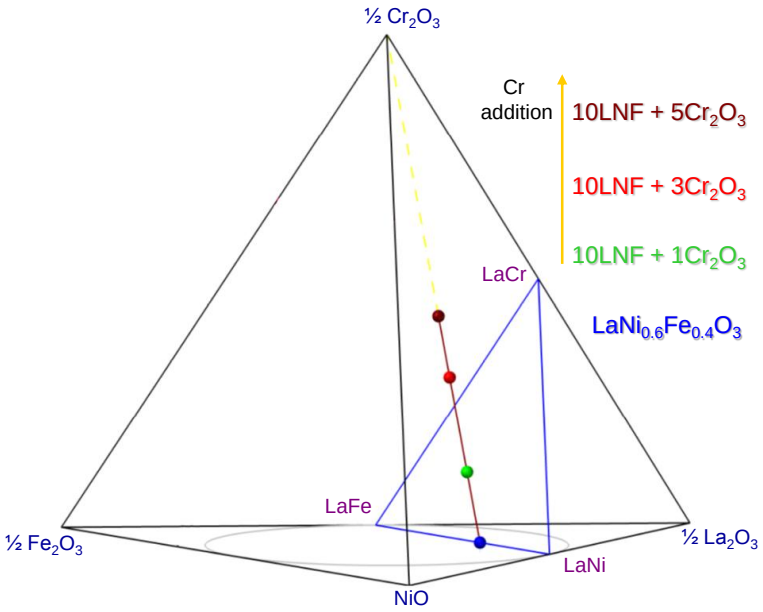

Figure 2.1: The mixtures of LNF and Cr_2O_3 presented on a schematic phase diagram. The compositions are expressed as the mole fractions of the metallic components (La,Ni,Fe,Cr) allowing to present the phase diagram in the form of a regular tetrahedron.

Both LNF and Cr_2O_3 powders were thoroughly mixed in weight ratios of 10:1, 10:3 and 10:5. The extent of the weight ratios of LNF and Cr_2O_3 mixtures was chosen to investigate possible various reaction products within the system of La-Ni-Fe-Cr-O. This approach is depicted in Fig. 2.1 by means of a schematic phase diagram. By expressing the compositions as the mole fractions of the metallic components (La, Ni, Fe, Cr) the phase diagram can be represented by the 4 equilateral triangles forming the faces of the regular tetrahedron. The various mixture compositions of LNF and Cr_2O_3 are depicted within the tetrahedron by bullets with corresponding color to the composition (Fig. 2.1).

The mixing procedure included overnight rolling of polyethylene bottles containing the powder mixture and zirconia milling balls. Subsequently, these powder mixtures were heated at 800°C for 200 h and at 600°C for 200 or 1000 h. The heating was conducted either in ambient air or in a flowing gas mixture of O_2, N_2 or Ar of a desired PO_2 level (2×10^{-2}, 4×10^{-3}, 6×10^{-5} atm) which was monitored using a zirconia oxygen analyzer (Systech, model ZR 893/4). The heating and cooling rate was 100°C/h. The resulting samples were examined at room temperature by powder X-ray diffraction (XRD) using a Philips X'Pert diffractometer, equipped with a X'Celerator, operating with Cu Kα radiation in steps of 0.02° (2θ) and 10 s counting time in a 2θ range between 10° and 140°. The lattice parameters were obtained by fitting the XRD spectra using the Le Bail method [35] implemented in

the LHPM-Rietica software [36].

As a reference, the thermal stability of pure LNF was investigated by means of prolonged heating at 600-800°C in a wide PO_2 range followed by XRD-analysis and by in-situ high temperature XRD (HT−XRD) using a Bruker D8 Advance diffractometer equipped with MRI chamber as heating device and operating in Bragg Brentano mode.

To check whether full thermodynamic equilibrium had been reached in some heated LNF−Cr_2O_3 powder mixtures, additional heat treatments were conducted on selected samples in air at 1400°C for 24 h. For the same reason, some perovskite compositions in the La(Ni,Fe,Cr)O_3 system were prepared via a standard solid-state reaction method and sintered in air at 1400°C for 24 h.

2.3 Results and Discussion

The following sections describe the results concerning the stability of LNF in direct solid-state contact with Cr_2O_3−powder at 800 and 600°C in a wide PO_2 range. The thermal stability of pure LNF is discussed first, followed by the XRD analysis of the reactivity between LNF and Cr_2O_3 at 800 and 600°C, respectively.

2.3.1 Thermal stability of pure LNF

Figure 2.2 and Table 2.1 shows the XRD patterns and cell parameters of the starting LNF material and LNF material after heating at 800°C in air for 200 h. Prolonged heating in air resulted in enhanced crystallinity as compared with the

Composition	Space group	a [Å]	b [Å]	c [Å]	V [Å]^3
LNF [37]	R$\bar{3}$c	5.5047(1)	-	13.2642(1)	348.06
LNF	R$\bar{3}$c	5.5032(9)	-	13.267(2)	347.98(9)
LNF 800°C/200 h	R$\bar{3}$c	5.5039(5)	-	13.267(1)	348.07(5)
10LNF+1Cr_2O_3 800°C/200 h	R$\bar{3}$c	5.5015(4)	-	13.274(9)	347.94(4)
	Pbnm	5.5273(4)	5.4773(4)	7.8145(5)	236.58(3)
10LNF+1Cr_2O_3 1400°C/24 h	*Pbnm*	5.5325(1)	5.5101(1)	7.7982(2)	237.72(1)
La($Ni_{0.28}Fe_{0.40}Cr_{0.32}$)$O_3$	*Pbnm*	5.5311(1)	5.5081(1)	7.7958(2)	237.51(1)
La($Ni_{0.1}Fe_{0.4}Cr_{0.5}$)O_3	*Pbnm*	5.5352(1)	5.5163(1)	7.8026(2)	238.24(1)
La($Ni_{0.5}Fe_{0.4}Cr_{0.1}$)O_3	*Pbnm*	5.5326(1)	5.4735(1)	7.7574(2)	234.44(1)
10LNF+3Cr_2O_3 800°C/200 h	*Pbnm*	5.5132(4)	5.4897(6)	7.8070(4)	236.29(3)
10LNF+5Cr_2O_3 800°C/200 h	*Pbnm*	5.5066(5)	5.4885(5)	7.8093(7)	236.02(4)

Table 2.1: Structural properties of investigated perovskites heated in air.

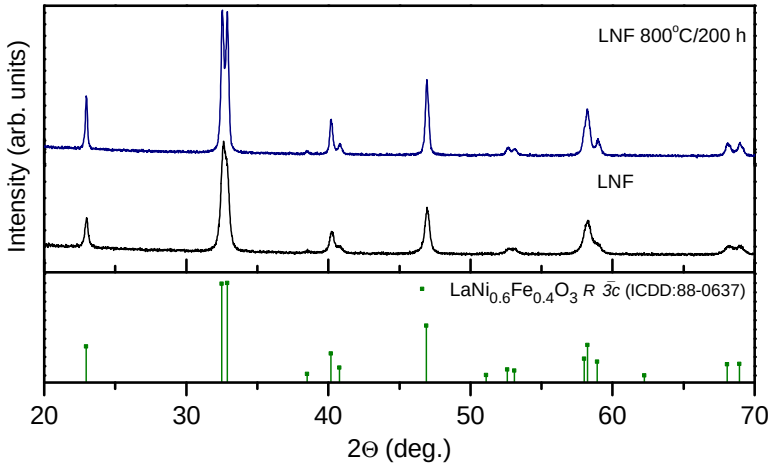

Figure 2.2: X-ray powder diffraction patterns of $La(Ni_{0.6}Fe_{0.4})O_3$ compound (initial LNF and LNF heated at 800 °C in air for 200 h).

starting LNF material (Fig. 2.2). Double splitting of the main reflection, characterizing the rhombohedral distortion of the ideal perovskite structure, was clearly visible at $32° < 2\theta < 33°$ for the LNF sample heated at 800°C in air for 200 h. The resulting fitted cell parameters of both LNF samples were identical within the given errors (Table 2.1) and comparable to previously reported values [37], demonstrating that LNF remains the same phase after prolonged heating in air. High temperature XRD analysis in the 800-1200°C range in air shows that $La(Ni_{0.6}Fe_{0.4})O_3$ also remained in the R$\bar{3}$c rhombohedral structure, indicating the stability of the LNF phase in the given temperature regime. In all cases, neither impurities (such as NiO) nor other phases were found, which further proves the intrinsic thermal stability of the

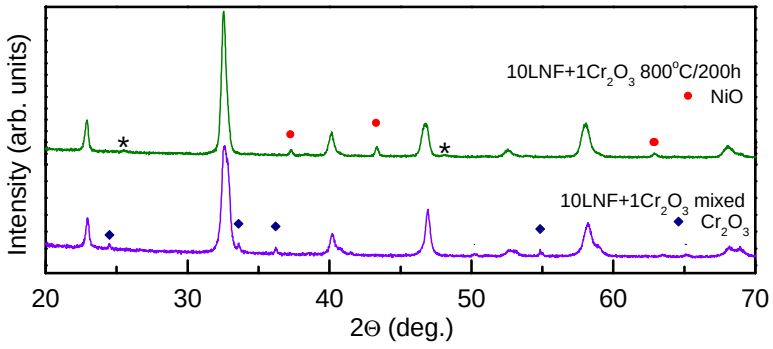

*Figure 2.3: X-ray powder diffraction patterns of the mixture $10LNF+1Cr_2O_3$ ('only mixed' and heated at 800°C in air for 200 h). The presence of the orthorhombic Pbnm phase is marked by * at the distinctive reflection angles where the specific Bragg reflections for the orthorhombic phase are visible.*

LNF compound.

Interestingly, 200 h heating of LNF in a PO_2 as low as 6×10^{-5} atm at 800°C did not result in perovskite phase decomposition. Moreover, the fitted lattice parameters of all rhombohedral LNF samples heat treated at 800°C in a wide PO_2 range exhibited comparable values within the range of one to three standard deviations.

2.3.2 LNF and Cr_2O_3 reactivity at 800°C

Mixture 10LNF+1Cr_2O_3

For the mixture of 10LNF+1Cr_2O_3 heated at 800°C in air for 200 h, the analysis of the XRD spectra revealed NiO and two perovskite phases: orthorhombic *Pbnm* and rhombohedral R$\bar{3}$c (Fig. 2.3). No presence of Cr_2O_3 was observed, suggesting that it had completely reacted with LNF. The fitted cell parameters of the two perovskite phases are summarized in Table 2.1. This table shows that the rhombohedral phase has comparable cell parameters as LNF, suggesting that LNF was still present in the mixture. The coexistence of the two perovskite phases is supported by the fact that the fit with only an orthorhombic or a rhombohedral phase resulted in the inferior reliability factors and worse accuracy of the fit. The presence of NiO, LNF as well as the absence of Cr_2O_3 implies that Ni was partially extracted from the LNF perovskite lattice, whereas Cr was incorporated, most likely to form orthorhombic La(Ni,Fe,Cr)O_3 phase.

The observed reactivity of LNF with Cr_2O_3 is in agreement with thermodynamic calculations [29], which predict the instability of LNF in combination with Cr_2O_3 and the precipitation of NiO. However, a similar study [38] has suggested that only the rhombohedral LNF and $NiCr_2O_4$ were formed. The difference in results with Ref. [38] is hard to explain, but might have resulted from NiO impurity that was reported in their initial LNF powder.

To investigate whether the 10LNF+1Cr_2O_3-mixture had reached thermodynamic equilibrium at 800°C, the same mixture was heated in air at 1400°C for 24 h in order to accelerate the reaction between the two components. Figure 2.4 shows X-ray diffraction peaks evolution in the 2θ range of 39-41° of LNF and the mixture of 10LNF+1Cr_2O_3 heated at different temperatures. The chosen 2θ range of 39-41° is characteristic for the detection of the presence of rhombohedral and orthorhombic perovskite phases [39]. For the pure LNF, heated at 800°C in air for 200 h, two single peaks appearing in the studied 2θ range can be indexed as $(202)_r$ and $(006)_r$ of the rhombohedral phase. In the sample 10LNF+1Cr_2O_3 heated at 800°C in air for 200 h, the small $(006)_r$ peak was very weak and the single peak $(202)_r$ began evolving into a doublet peak, indicating the presence of both rhombohedral and orthorhombic perovskite phases. This observation was supported by better reliability factors and higher accuracy of the fit obtained for a two perovskite system as compared to the fitting with only a single perovskite. For the same mixture of 10LNF+1Cr_2O_3 but heated at 1400°C for 24 h, the single peak changed completely into a doublet peak indexed as $(022)_o$ and $(202)_o$ of the orthorhombic phase. No peak identified as rhombohedral phase was detected. Therefore, due to the fact that after cooling down

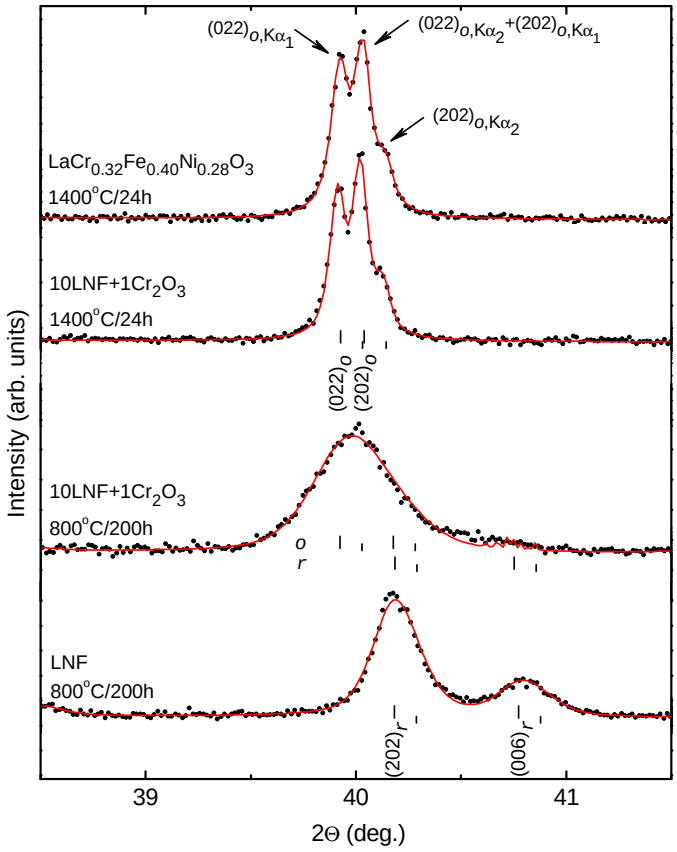

Figure 2.4: X-ray diffraction peaks variation in the 2θ range 39-41° of LNF and the mixture 10LNF+1Cr_2O_3 heated in air at different temperatures. The continuous line is the Le Bail fit using the space group $R\bar{3}c$ and/or Pbnm. For a doublet peak $(022)_o$ and $(202)_o$, additional splitting due to $K\alpha_1$ and $K\alpha_2$ radiations is visible (denoted by arrows). In all cases the longer and shorter bars correspond to $K\alpha_1$ and $K\alpha_2$ radiations, respectively.

from 1400°C to room temperature only a single orthorhombic phase was observed, it is very likely that the Cr containing orthorhombic perovskite is a thermodynamically stable phase over the whole temperature range of RT-1400°C. As a consequence, this indicates that the sample 10LNF+1Cr_2O_3 heated at 800°C for 200 h has not yet reached thermodynamic equilibrium, most likely due to the slower reaction kinetics as compared to 1400°C. For the sample sintered at 1400°C for 24 h, the composition of the orthorhombic perovskite phase can be calculated by completely replacing Ni in the LNF lattice by Cr, resulting in the composition $La(Ni_{0.28}Fe_{0.40}Cr_{0.32})O_3$ (under the assumption that the amount of Cr lost due to the possible vaporization process is negligible, as indicated by minor Cr weight change of less than 0.5 wt %). As a final check, this perovskite phase was prepared by means of a standard

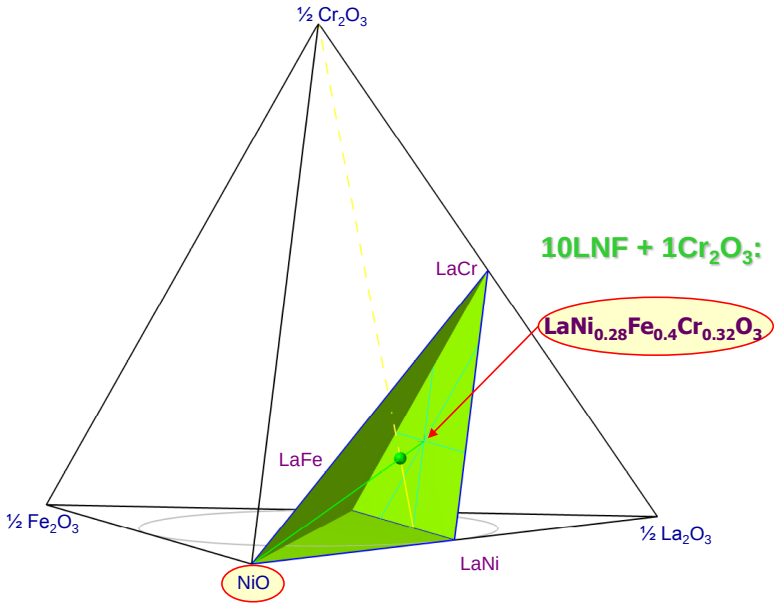

Figure 2.5: In the thermodynamic equilibrium situation the 10LNF+1Cr_2O_3-mixture is composed of NiO and orthorhombic La($Ni_{0.28}Fe_{0.40}Cr_{0.32}$)$O_3$ perovskite. The representation of the formed phases is given by means of a schematic phase diagram. The compositions are expressed as the mole fractions of the metallic components (La, Ni, Fe, Cr) allowing to present the phase diagram in the form of a regular tetrahedron. The green volume within the tetrahedron presents the predicted composition range of LNF+xCr_2O_3-mixture for which, in the thermodynamic equilibrium situation, only NiO and a perovskite is formed.

solid-state reaction (SSR) method with a final sintering step in air at 1400°C for 24 h. The resulting X-ray pattern (see Figure 2.4 and Table 2.1) indicates that the composition La($Ni_{0.28}Fe_{0.40}Cr_{0.32}$)$O_3$ exists as a single phase with an orthorhombic *Pbnm* structure.

Concluding, it seems that in the thermodynamic equilibrium situation the 10LNF+1Cr_2O_3-mixture is composed of NiO and the orthorhombic La($Ni_{0.28}Fe_{0.40}Cr_{0.32}$)$O_3$ perovskite. Fig. 2.5 shows the representation of the formed phases in such a case. A schematic phase diagram in a form of a regular tetrahedron presents in Fig. 2.5 the predicted composition range of LNF+$x$$Cr_2O_3$-mixture for which, in the thermodynamic equilibrium situation, only NiO and a perovskite is formed.

Until now, no crystallographic data concerning the perovskites belonging to the La(Ni,Fe,Cr)O_3 system have been available. Therefore, three different compositions of the $LaFe_{0.4}(Ni_{0.6-x}Cr_x)O_3$ series were prepared to further confirm the existence of a perovskite solid solution phase where Ni is replaced by Cr in LNF. The X-ray diffraction analysis shows that the $LaFe_{0.4}(Ni_{0.6-x}Cr_x)O_3$ series samples with $x = 0.1, 0.32, 0.5$ adopt an orthorhombic structure with the space group *Pbnm*. An

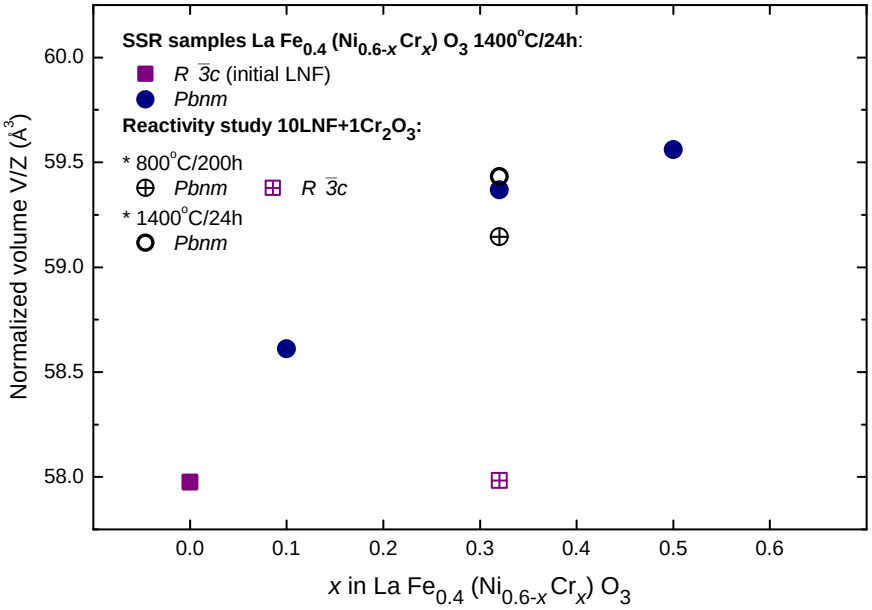

Figure 2.6: Variation of the normalized cell volume as a function of Cr amount in the $LaFe_{0.4}(Ni_{0.6-x}Cr_x)O_3$ series. Additionally, values for 10LNF+1Cr_2O_3 samples heated in air are included.

increase in cell parameters and cell volume following Vegard's law was observed on the successive replacement of the smaller nickel-ion by the larger chromium-ion. The standard six coordinate ionic radii of Ni^{3+} and Cr^{3+} is 0.60 Å and 0.615 Å, respectively [40].

Figure 2.6 shows the increase in the normalized volume V/Z, where V is the unit cell volume and Z is the number of formulas per unit cell, with increasing Cr-content. This figure also provides the normalized volume data of the orthorhombic and rhombohedral perovskite phase of the 10LNF+1Cr_2O_3 sample heated at 800°C in air for 200 h. It is observed that the normalized volume of the rhombohedral phase in the mixture is equal to the normalized volume of LNF. The orthorhombic phase in the mixture has slightly lower normalized volume than the expected orthorhombic perovskite $La(Ni_{0.28}Fe_{0.40}Cr_{0.32})O_3$, indicating a lower Cr content - which is in agreement with the fact that this mixture still contains the rhombohedral LNF and has not yet reached equilibrium.

Figure 2.6 also shows that the increase in the temperature to 1400°C/24 h for the 10LNF+1Cr_2O_3 mixture results in a perovskite cell volume corresponding with $La(Ni_{0.28}Fe_{0.40}Cr_{0.32})O_3$, which proves that all available Cr can be incorporated into the perovskite lattice. In sum, although the thermodynamic equilibrium has probably not yet been reached for the sample 10LNF+1Cr_2O_3 heated for 200 h at 800°C in air, the reactivity between LNF and Cr_2O_3 was clearly demonstrated.

In case of the heated mixtures of 10LNF+1Cr_2O_3 at PO_2 lower than atmospheric (2×10^{-2}, 4×10^{-3}, 6×10^{-5} atm) the XRD analysis revealed exactly the same phases as observed in air. The obtained lattice parameters of both orthorhombic and rhombohedral phases of the mixtures heated under low oxygen partial pressures were comparable with the cell parameters of the perovskite phases in the mixtures heated in air within the range of one to three standard deviations. Consequently, lowering the oxygen partial pressure results in a similar reactivity between LNF and Cr_2O_3 (for the sample of 10:1 ratio) as observed in air, which means that Ni in LNF is substituted by Cr and the mixture has not yet reached equilibrium.

Mixture 10LNF+3Cr_2O_3 and 10LNF+5Cr_2O_3

The X-ray diffraction analysis of the sample 10LNF+3Cr_2O_3 heated at 800°C for 200 h in the PO_2 range of $2 \times 10^{-1} - 6 \times 10^{-5}$ atm showed the presence of an orthorhombic perovskite phase, a spinel phase, and NiO (Fig. 2.7). The initial rhombohedral LNF-phase was no longer observed, indicating a complete reaction of LNF with Cr_2O_3. Interestingly, in the samples heated at PO_2 above 4×10^{-3} atm no Cr_2O_3 was found whereas trace amounts of Cr_2O_3 could be detected for the sample exposed to PO_2 as low as 6×10^{-5} atm. The presence of trace amounts of chromium oxide at a PO_2 of 6×10^{-5} atm suggests a lower reactivity of Cr_2O_3 under this condition, which might indicate that vapor phase transport of Cr-species plays a role in the reaction mechanism, given the fact that volatile Cr species are less present under low partial oxygen pressures [22].

In the sample 10LNF+5Cr_2O_3 heated at 800°C for 200 h in a wide PO_2 range, the main phase detected was an orthorhombic perovskite phase, resembling the Cr rich La(Fe,Cr)O_3 phase (Table 2.1). This result suggests that first Ni is being replaced by Cr, followed by the replacement of Fe by Cr. Next to this perovskite phase, for every partial oxygen pressure condition, a significant amount of a spinel phase was detected together with a trace amount of unreacted Cr_2O_3, while NiO was not detected (Fig. 2.7). The spinel phase identified in the case of 10LNF+3Cr_2O_3 and 10LNF+5Cr_2O_3 mixtures can generally be described as (Ni,Fe)(Fe,Cr)$_2O_4$. In these samples, no rhombohedral LNF-phase was present, again indicating a complete reaction of LNF with Cr_2O_3.

For the discussed samples of 10LNF+$x$$Cr_2O_3$ ($x = 1, 3, 5$) heated at 800°C, the lower PO_2 exposure conditions did not influence either the reactivity or the lattice parameters, which were comparable with the variations in the range from one to three standard deviations.

The current study on the reactivity between LNF and Cr_2O_3 at 800°C demonstrates that Cr enters the perovskite phase, replacing first Ni and then Fe in the investigated PO_2-range. The observed order of the precipitation (first Ni, then Fe) from the initial LNF perovskite phase correlates well with the relative thermodynamic stability of the perovskites: $LaCrO_3 > LaFeO_3 > LaNiO_3$ [41].

The substitution of Cr into the LNF lattice may result in a decrease of the electronic conductivity, similar to that reported for the La($Ni_{1-x}Cr_x$)O_3 system [42]. This might have significant implications for the ohmic losses across an LNF layer

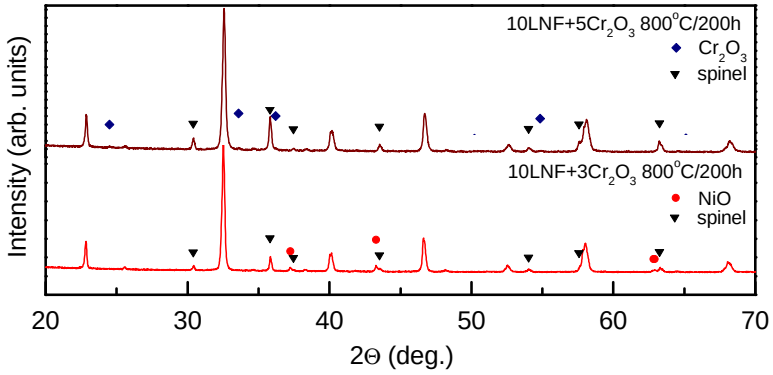

Figure 2.7: X-ray powder diffraction patterns of the mixtures 10LNF+3Cr_2O_3 and 10LNF+5Cr_2O_3 heated at 800° C for 200 h.

exposed to Cr-species during a fuel cell operation under the given conditions. Moreover, LNF crystal structure transformation from rhombohedral to orthorhombic, induced by Cr-incorporation might seriously affect the electrochemical activity of the LNF material. Comprehensive investigation of the lateral conductivity of the La(Ni,Fe)O_3 layer exposed to Cr-species will be reported in Chaper 3 and 4.

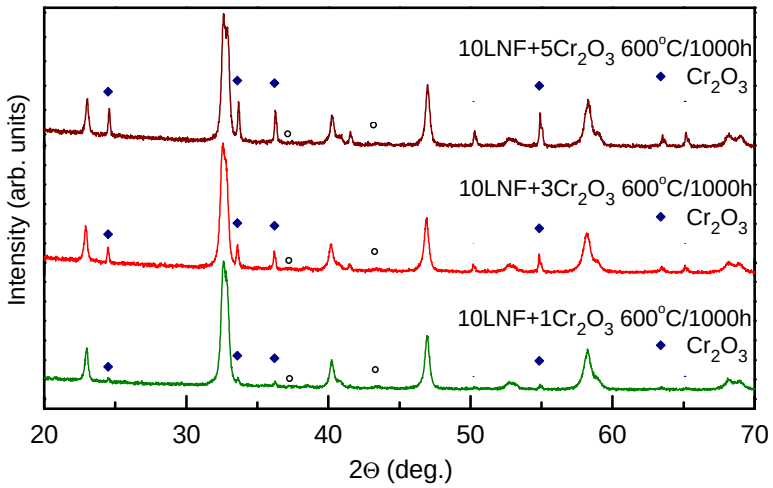

Figure 2.8: X-ray powder diffraction patterns of 10LNF+xCr_2O_3 mixtures ($x = 1, 3, 5$) heated in air at 600° C for 1000 h. The presence of the trace amounts of NiO is marked by ° at the most intensive Bragg reflections.

LNF and Cr_2O_3 reactivity at 600°C

The previous section showed that the thermodynamic equilibrium in a mixture of LNF and Cr_2O_3 depends on the temperature levels and the exposure time. Equilibrium was not reached after 200 h at 800°C, but increasing the temperature to 1400°C did result in an equilibrium composition. Consequently, lowering the temperature is expected to hinder the reactivity between LNF and Cr_2O_3. Therefore, a similar reactivity study was conducted at 600°C for 200 h and also for a prolonged period of 1000 h.

The XRD−analysis of the 10LNF+$x$$Cr_2O_3$ mixtures ($x = 1, 3, 5$) heated in air at 600°C for 200 h and ultimately for 1000 h revealed no reaction between the two compounds: in all cases only rhombohedral LNF and unreacted Cr_2O_3 were found, however trace amounts of NiO appeared (Fig. 2.8). Lowering the partial oxygen pressure gave the same results as obtained in the reactivity test in air. The fitted lattice parameters of all samples heat treated at 600°C under all PO_2 conditions exhibited comparable values within the range of one to three standard deviations. However, the influence of Cr cannot be neglected even at 600°C as the minor appearance of NiO might indicate some influence of Cr on the phase composition. Presumably, some reaction between Cr and the perovskite could possibly take place at the surface of the LNF-grains. NiO may nucleate and form a minor second phase. The Cr-substitution into the LNF-perovskite might take place in a thin subsurface layer in the pure LNF grains creating a core-shell like structure. The formed reaction layer might be too thin to observe a change in the perovskite lattice parameters using XRD. This phenomenon needs further investigation (Chapter 3 and 5).

The application of LNF at 600°C as a Cr-resistant cathode or contact coating would seem to be feasible, but this ought to be tested under long-term fuel cell operating conditions (Chapter 3 and 5). Such a low operating temperature of 600°C might require improvement of the LNF-cathode electrochemical activity possibly by means of composite structure or cathode infiltration.

2.4 Conclusions

This study demonstrates the intrinsic instability of the LNF cathode when it is in direct contact with Cr_2O_3 at 800°C. This situation may occur in the cathode compartment of a SOFC stack, where the Cr-containing metallic interconnect is in direct contact with this cathode or with LNF current collecting layer. The rate of the chromium reaction with LNF has been demonstrated to depend on the temperature and the exposure time. Lowering the operating temperature to 600°C resulted in a very low Cr reactivity with LNF: no reaction was observed with XRD. Thus, LNF at 600°C would seem to offer promising opportunities concerning its use as a Cr-resistant cathode, current collecting layer and/or interconnect protective coating. Nevertheless, further investigations remain necessary, especially under long-term fuel cell operation conditions.

The solid state reactivity between LNF and chromia is not significantly influenced by the level of the PO_2, at least not within the PO_2 range studied herein.

This result might indicate that Cr-poisoning of LNF, by solid state diffusion and subsequent solid state reactivity, would be the same along the depth of the operating LNF cathode when only taking partial oxygen pressure gradients into account. However, gas diffusion of volatile Cr-species may play an additional role in the actual distribution of Cr throughout the cathode layer.

Acknowledgments

This work was supported by the European Commission, as part of the European Project RealSOFC (SES6-CT-2003-502612) and SOFC600 (SES6-CT-2006-020089). Adrien Signolet is acknowledged for his involvement in the part of the study. Jan Pieter Ouweltjes is thanked for helpful discussions.

3 Impact of Cr-poisoning on the conductivity of $LaNi_{0.6}Fe_{0.4}O_3$

This study demonstrates the significant impact of Cr on the electronic conductivity of a $LaNi_{0.6}Fe_{0.4}O_3$ (LNF) porous cathode layer at 800°C. Vapor transport of Cr-species, originating from a porous metallic foam, and subsequent reaction with LNF, results in a decrease of the electronic conductivity of the LNF-layer. Cr has been detected throughout the entire cross-section of a 16 μm thick LNF layer, while Ni, besides its compositional distribution in the LNF layer, has also been found in enriched spots forming Ni-rich metal oxide crystals. Transmission electron microscopy revealed that Cr is gradually incorporated into the LNF-grains, while Ni is proportionally expelled. Electron diffraction performed in the center of a sliced grain showed the initial rhombohedral crystal structure of LNF, whereas diffraction performed close to the edge of the grain revealed the orthorhombic perovskite crystal structure, indicating a Cr enriched perovskite phase. Progressive Cr deposition and penetration into the LNF grains and necks explains the electronic conductivity deterioration. The impact of Cr-poisoning on the electronic conductivity of the LNF porous layer is considerably smaller at 600°C than at 800°C.

Published in: *Journal of Power Sources* **196** 9290-9298 (2011) – **Key Scientific Article** (*Renewable Energy Global Innovations*)
ECS Transactions **35** (1) 2035-2043 (2011)

Presented at: 12^{th} International Symposium on SOFC, 219^{th} ECS Meetings; May 2011, Montreal, Canada (*talk*, *student award*)
Advances in Dutch Hydrogen and Fuel Cell Research; March 2011, Eindhoven, The Netherlands (*talk*)

3.1 Introduction

The perovskite $LaNi_{0.6}Fe_{0.4}O_3$ (LNF) is considered a candidate cathode and interconnect coating material for various intermediate temperature SOFC (IT-SOFC) systems where relatively cheap interconnect materials such as chromia-forming ferritic stainless steels are used. High electronic conductivity and thermal expansion coefficient matching that of zirconia [32], together with claimed high Cr-resistance [11, 14, 16] are the properties of LNF that enable its use as cathode current collecting layers, interconnect protective coatings and/or electrochemically active cathode layers. Furthermore, the use of LNF material as a cathode is recommended for metal-supported SOFCs [43] (see Fig. 1.3), due to claimed high Cr-tolerance and good performance obtained for LNF sintered at low temperatures [44].

In order to ascertain reliable operation of LNF in a Cr-containing environment, such as in an IT-SOFC stack (see Fig. 1.4), a study regarding the actual tolerance of LNF towards Cr was undertaken, especially in the view of recent findings demonstrating the occurrence of solid-state reactivity of LNF with chromia at 800°C: It has been observed that LNF is chemically unstable at 800°C when it is in direct contact with Cr_2O_3 as Cr-cations enter the perovskite phase, replacing first Ni- and then Fe-cations [45, 46](Chapter 2 of this thesis). The present study investigates the extent to which the electronic conductivity of the LNF layer is affected by the exposure to Cr. Transport of Cr is known to take place by solid-state diffusion of Cr-cations and by vapor phase transport of mainly $CrO_{3(g)}$ and/or $CrO_2(OH)_{2(g)}$ [10, 22]. The aim of this study is to describe and clarify the mechanism of the attack of volatile Cr-species and its impact on the electronic conductivity of a porous LNF-layer. The electronic conductivity is monitored under dry synthetic air conditions. In order to accelerate the Cr-poisoning impact, active flushing of the gas atmosphere over the LNF-layer has been prevented, with the aim of building an equilibrium pressure of the volatile Cr-species above the LNF-layer. On basis of literature data it is expected that the main volatile Cr-species in dry synthetic air is $CrO_{3(g)}$ [10, 22]. The exposed porous LNF layer resembles porous SOFC cathode layers that have been investigated in other studies [17, 34]. Based on the present study a tentative mechanism for the Cr attack on the scale of one LNF particle will be presented.

3.2 Experimental

3.2.1 Sample preparation

LNF layers were prepared using $LaNi_{0.6}Fe_{0.4}O_3$ powder (Praxair, 99.9% purity). The mechanical support used during the conductivity measurements was composed of a tape cast 3 mol% yttria stabilized zirconia (3YSZ) layer, that was sintered at 1500°C for 1 h resulting in an electrolyte disc of 25 mm diameter and 90 μm thickness, which was subsequently covered with a 2 μm thick $Gd_{0.4}Ce_{0.6}O_{1.8}$(GDC) barrier layer by means of screen printing followed by sintering at 1300°C for 1 h. The LNF powder, after precalcination at 800°C for 1 h in air, was milled and dispersed into an alcohol-binder solution using a Dispermat (VMA-Getzmann GmbH) milling

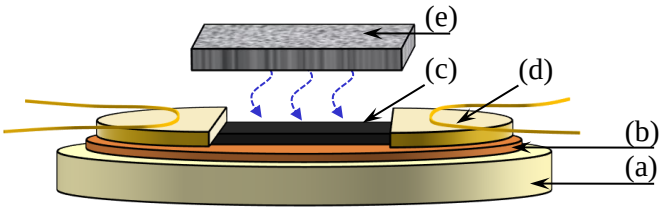

Figure 3.1: A schematic drawing of the sample used for the 'semi four probe' electronic conductivity measurements while exposed to a Cr-source. The 3YSZ disc (a) covered with a GDC barrier layer (b) served as a mechanical support for the LNF layer (c) and gold contacts (d). The porous ferritic ITM-14 foam (e) served as a source of volatile Cr-species (blue dashed arrows). Note that the drawing is not to scale. No active gas flushing took place over the porous LNF layer resulting in a semi-stagnant gas atmosphere above the LNF layer.

system. The LNF paste was screen printed on top of the GDC barrier layer and sintered at 1250°C for 1 h. Such obtained LNF layer microstructure is referred to as LNF-B in Chapters 4-6. The resulting LNF perovskite layer formed a 10 mm wide strip with a thickness of approximately 15-20 μm. Subsequently, gold thin foils, onto which gold wires were spot welded to serve as voltage and current probes, were attached at both ends of the LNF perovskite layer with the help of a gold paste (Metalor) and sintered in air at 850°C for 3 h to allow the measurement of the sheet conductivity [34, 47]. The resulting uncovered LNF layer had a surface area of 10 mm × 10 mm. The prepared sample is shown schematically in Fig. 3.1.

3.2.2 Conductivity measurements

In order to measure the electronic conductivity each freshly prepared sample was heated in a quartz tube, flushed with synthetic dry air, 20% O_2 (purity 99.6%, <7ppmv H_2O, where ppmv denotes parts per million in volume) and 80% N_2 (purity 99.999%, <4ppmv H_2O) at a total flow rate of 100 ml/min, to the operating temperature of 800 or 600°C with a rate of 100°C/h. The construction of the testing equipment was such that no active flushing over the LNF sample took place. After reaching the operating temperature, the impedance was measured using a Solartron 1255 frequency response analyzer in conjunction with a Solartron 1287A electrochemical interface in a 'semi four probe' configuration (i.e. the two electrodes had separate current and voltage probe wires). The applied frequencies ranged from 100 kHz to 0.1 Hz with a signal amplitude of 10 mV. The specific electronic conductivity in S/cm was calculated from the sheet resistance of the porous LNF layer and the LNF layer thickness, as determined by SEM, assuming a negligible ionic contribution [32, 48]. The high frequency intercept in the Nyquist plot (ZView2) was taken as the electronic resistance.

The conductivity measurements were performed as function of time and temperature in a Cr-free (reference) and in a Cr-containing environment. The temperature

dependence of conductivity was obtained directly after the exposure experiments. The cooling rate was 100°C/h with a short dwell time at each data point. For the Cr-poisoning experiments an ITM-14 ferritic FeCr-based alloy in the form of a porous foam (Plansee AG, Reutte, Austria [21, 49]) was used as a Cr source. The laser cut foam with dimensions of 14 mm × 10 mm was pre-oxidized for 100 h at 800°C prior to the experiment to insure the presence of a Cr-containing oxide scale on the metal surface. This 0.7 mm thick ITM-14 sheet was positioned 1 mm above the 10 mm × 10 mm area of the LNF layer without any direct contact, as depicted in Fig. 3.1. For each of the Cr-poisoning experiments a freshly cut and pre-oxidized ITM-14 foam was used.

3.2.3 Microstructural and compositional characterization

The porosity of the as-prepared LNF-layers was obtained from the density of the LNF layer calculated from geometrical dimensions, measured weight and theoretical density of $LaNi_{0.6}Fe_{0.4}O_3$.

After carrying out the conductivity measurements the surface, the fractured cross-section and the embedded and polished cross-section of the samples were analyzed by field emission scanning electron microscopy, using a JEOL JSM 6330F FEG-SEM equipped with an EDX detector (ThermoNoran's Pioneer NORVAR). The SEM micrographs of the LNF layers surface were digitally processed with ImageJ [50]. The micrographs were binarized by automatic thresholding and further analyzed to obtain the microstructural features such as particle and neck size distribution statistics.

The elemental composition of the LNF-layers exposed to Cr was obtained by scraping off the LNF-layer and analyzing the elemental composition of the resulting powder by means of inductively-coupled plasma-optical emission spectroscopy (ICP-OES), using a Varian Vista AX PRO CCD.

The Cr-exposed sample chosen for the transmission electron microscopy (TEM) analyses was prepared by the method of Dimple Grinding/Polishing in water-free conditions and argon ion beam etching. TEM analyses were performed using Philips CM300ST-FEG TEM equipped with a Gatan Tridiem energy filter and a Thermo Fisher NORAN System Six EDX analyzer with a Nanotrace EDX detector. All TEM experiments were performed at an acceleration voltage of 300 kV, using several modes of operation: General Bright Field TEM imaging (BF-TEM) with Objective Aperture (OA), Selected Area Electron Diffraction (SAED), and Energy Dispersive X-ray analysis (EDX) in a static small-spot size mode.

3.3 Results and discussion

3.3.1 Microstructure of the LNF layer

Fig. 3.2 shows the SEM micrograph of the fractured cross-section of the LNF sample. The LNF layer possessed a homogenous and continuous microstructure with an open granular structure and well-connected grains. The LNF layer exhibited a

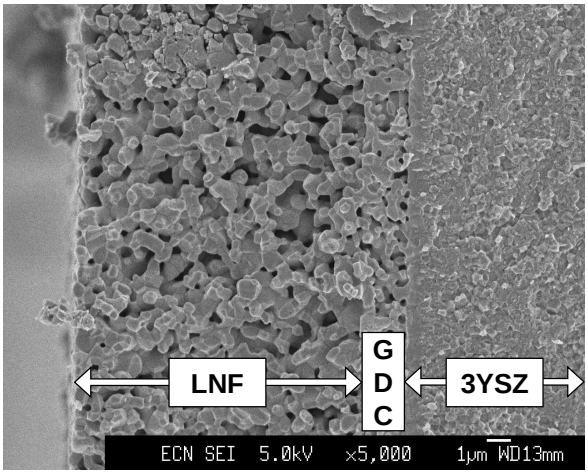

Figure 3.2: SEM micrograph of the fractured cross-section of the LNF-GDC-3YSZ assembly.

total porosity of 32% with an average layer thickness of 16 μm. The open porosity enabled vapor phase transport of volatile Cr-species into the LNF layer.

In Fig. 3.3a, the digitally processed SEM micrograph of the representative area of the LNF layer surface shows the inter-granular porosity (white areas) and remaining interconnected particles. The sizes of the necks and particles were calculated to create the size distribution statistics as shown in Fig. 3.3b. The median neck diameter d(50) was 0.33 μm and the median grain diameter D(50) was 0.54 μm.

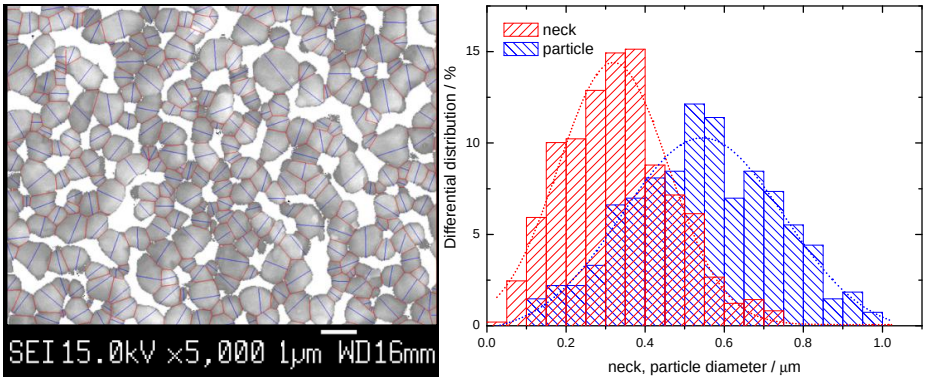

(a) (b)

Figure 3.3: (a) Digitally processed SEM micrograph of the LNF layer surface showing the inter-granular porosity (white areas) and remaining interconnected particles. Necks' diameters are sketched with red lines and average grains' diameters with blue lines. The collection of necks and grains sizes is presented in form of the neck and particle size distributions (b). Dotted lines of a Gaussian fit are only a guide to the eye.

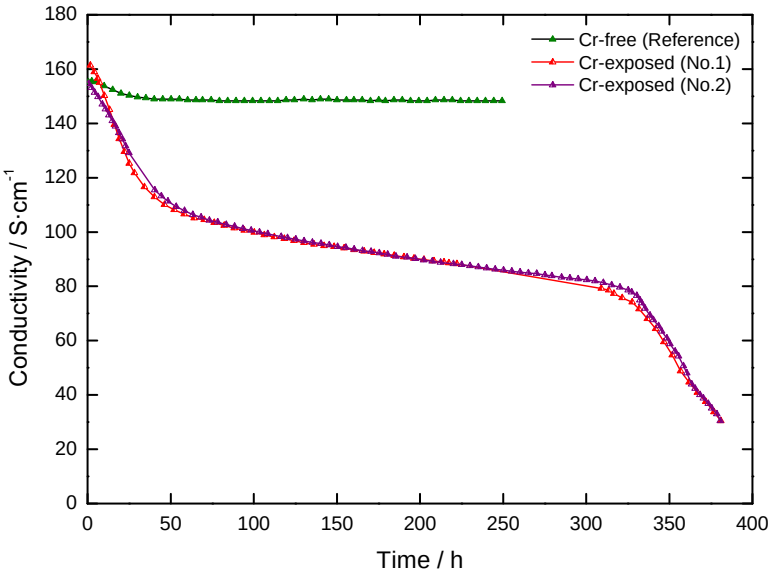

Figure 3.4: Electronic conductivity evolution at 800° C for the Cr-free and Cr-exposed LNF layers.

3.3.2 Conductivity evolution of LNF at 800°C

Conductivity evolution of LNF as function of time

Fig. 3.4 presents the electronic conductivity evolution with time of the LNF layers at 800°C in Cr-free and in Cr-containing atmospheres. The reference sample showed a relatively stable electronic conductivity for a testing period of 250 h. The LNF sample exposed to volatile Cr species (sample No.1 in Fig. 3.4) exhibited a significant loss in the electronic conductivity within the first 50 h, then a semi-linear conductivity decline could be observed in the time period of approximately 100−300 h. Subsequently, a second steep conductivity drop appeared after 320 h of exposure to volatile Cr-species. In the repeated Cr-poisoning test (sample No.2 in Fig. 3.4), the shape of the electronic conductivity drop was reproducible with a maximum deviation in time of 3 h, indicating consistent and reproducible results (Fig. 3.4).

Conductivity as function of temperature

For both the Cr-free and the Cr-exposed samples, the electronic conductivity σ as a function of temperature was measured directly after the exposure at 800°C in order to determine the impact of volatile Cr-species on the electronic conductivity behavior of the LNF layer. Fig. 3.5 shows the relation between $\log(\sigma T)$ versus the inverse absolute temperature. This relationship was chosen because literature indicates that the electronic conductivity of $LaNi_xFe_{1-x}O_3$ series ($x \leqslant 0.6$) can be described by the

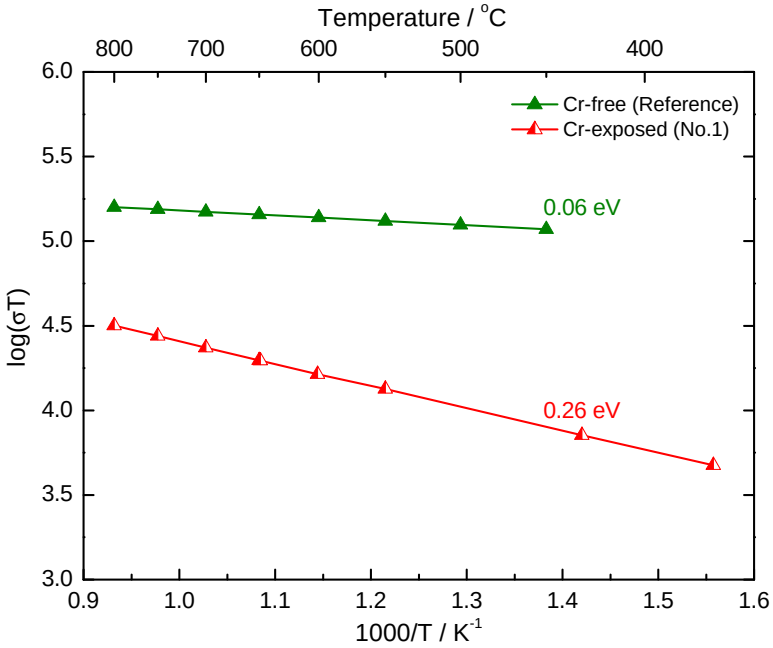

Figure 3.5: Temperature dependences of the electronic conductivity for the Cr-free (250 h at 800° C) and Cr-exposed (380 h at 800° C) LNF layer.

thermally activated small polaron mechanism [32, 51] which is generally expressed as:

$$\sigma = \frac{1}{T} A e^{-\frac{E_a}{kT}} \tag{3.1}$$

in which E_a is the activation energy for small polaron hopping conduction, k is the Boltzmann constant, T is the absolute temperature and A is a pre-exponential factor.

Both the Cr-free and the Cr-exposed samples (No.1) exhibit linear behavior in the $\log(\sigma \mathrm{T})$ vs. $1000/T$ coordinates (Fig. 3.5), which is in agreement with the assumed small polaron conduction mechanism. There is a significant difference in the slope of the linear trend between the reference sample and the Cr-exposed sample, hence the effective activation energy increased significantly for the Cr-exposed layer from 0.06 eV to 0.26 eV. The activation energy measured for the Cr-free reference porous LNF layer is similar to literature data of LNF (0.05−0.08 eV) [51, 52], whereas the E_a value of the Cr-exposed layer is comparable to $\mathrm{La(Fe,Cr)O_3}$ compounds (0.20−0.30 eV) [42, 53–55].

LNF sample type	Time (h) at 800°C	Atomic percentage (at %)				Fraction percentage (%)			
		La	Ni	Fe	Cr	$[La]_{cal} = \frac{[La]_{abs}}{\sum La,Ni,Fe}$	$[Ni]_{cal} = \frac{[Ni]_{abs}}{\sum La,Ni,Fe}$	$[Fe]_{cal} = \frac{[Fe]_{abs}}{\sum La,Ni,Fe}$	$[Cr]_{cal} = \frac{[Cr]_{abs}}{\sum La,Ni,Fe}$
Powder $LaNi_{0.6}Fe_{0.4}O_3$	-	50.5(6)	29.9(5)	19.6(2)	0.0	50.5(6)	29.9(5)	19.6(2)	0.0
Cr-free LNF layer	250	50.0(6)	30.2(5)	19.8(2)	0.0	50.0(6)	30.2(5)	19.8(2)	0.0
Cr-exposed LNF layer	25	51.0(6)	29.2(5)	19.7(2)	0.11(6)	51.0(6)	29.3(5)	19.7(2)	0.11(6)
	50	51.3(6)	29.0(5)	19.6(2)	0.15(6)	51.3(6)	29.0(5)	19.7(2)	0.15(6)
	100	51.3(6)	29.0(5)	19.5(2)	0.32(6)	51.4(6)	29.1(5)	19.5(2)	0.32(6)
	200	50.4(6)	29.4(5)	19.7(2)	0.43(6)	50.6(6)	29.6(5)	19.8(2)	0.43(6)
	325	49.9(6)	29.6(5)	19.7(2)	0.80(6)	50.3(6)	29.9(5)	19.8(2)	0.81(6)
	350	49.9(6)	29.3(5)	19.6(2)	1.20(6)	50.5(6)	29.7(5)	19.8(2)	1.22(6)
	380	48.7(6)	29.2(5)	19.3(2)	2.88(6)	50.2(6)	30.0(5)	19.8(2)	2.97(6)

Table 3.1: ICP-OES investigation of the LNF powder, Cr-free and Cr-exposed LNF-layers as function of the exposure time.

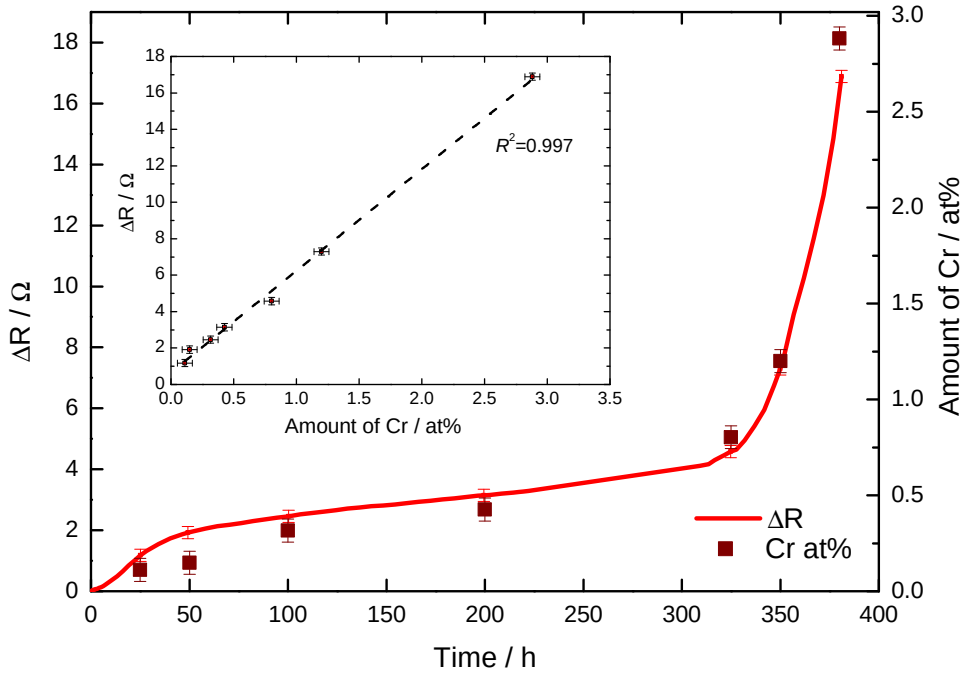

Figure 3.6: The increase in the sheet resistance ΔR (ΔR=$R(t)$-$R_{initial}(t = 0)$) of the Cr-exposed LNF layer (No.2) in time plotted together with the amount of deposited Cr. The inset presents directly the correlation of ΔR versus amount of Cr deposited in the corresponding time periods in the bulk of the Cr-exposed LNF layers.

3.3.3 Cr distribution in the Cr-exposed LNF layer

This section deals with the analysis of the nominal LNF layer composition as a function of the exposure time to volatile Cr-species and the resulting distribution of Cr throughout the layer.

Table 3.1 presents the results of the ICP-OES investigation of the LNF powder, Cr-free LNF-layer, and also the Cr-exposed LNF-layers as a function of the exposure time. It is important to note that the ratio between La-, Ni-, and Fe-concentration (50:30:20) did not change in any of the Cr exposure experiments. Hence there was no cation loss from the porous LNF layer during the exposure to Cr-species. As shown in Table 3.1, the Cr-content increased with the exposure time suggesting that the decrease in the electronic conductivity was related to the amount of Cr deposited in the layer. Fig. 3.6 presents the correlation of the increase in the sheet resistance ΔR of the Cr-exposed LNF layer (No.2) in time with the amount of Cr detected in the bulk of the layer in the corresponding time periods. The nearly linear relationship (R^2=0.997) of this correlation (inset in Fig. 3.6) indicates indeed that the decrease in the electronic conductivity (Fig. 3.4) was related to the amount of Cr deposited in the Cr-exposed LNF-layer.

The non-linear time dependent behavior of the electronic conductivity together with the corresponding amount of deposited Cr indicates that the Cr-incorporation in the LNF-layer is not linear in time. One of the possible explanations of the non-linear Cr-incorporation behavior might be a change in the evaporation behavior of the porous ITM-14 foam-like structure with time, in contrast to a steady Cr evaporation rate reported for the ITM-14 sheet [19, 21, 49]. To explain this possible change in the Cr evaporation behavior, post-test analysis was performed on the exposed ITM-14 porous foams [56]. SEM-EDX analysis revealed that the outer oxide scale formed during the exposure in dry air at 800°C changed with time. In case of the ITM-14 foams exposed no longer than 300 h (in addition to the initial pre-oxidation step of 100 h) the outer oxide scale was mainly composed of $(Mn,Cr)_2O_4$. In case of foams exposed longer, the outer scale was formed mainly by Cr_2O_3. The Cr vaporization from $(Mn,Cr)_2O_4$ layers is reduced due to a lower partial pressure of CrO_x species over $(Mn,Cr)_2O_4$ compared to Cr_2O_3 (for which $pCrO_x$ is $\sim 1 \times 10^{-4}$ Pa at 800°C) [19, 20, 22]. Such a change in the composition of the outer oxide scale of the porous ITM-14 foam will in consequence account for a different Cr release rate with time [20, 56] causing the observed sudden decrease in the electronic conductivity after 300 h (Fig. 3.4) together with the corresponding increased amount of deposited Cr (Table 3.1 and Fig. 3.6).

The distribution of Cr in the LNF layer exposed to volatile Cr-species for 380 h at 800°C was provided by Energy Dispersive X−ray spectroscopy (EDX). Fig. 3.7 shows the SEM-EDX elemental mapping on an embedded and polished cross-section of the Cr-exposed LNF layer. The EDX-map demonstrates that Cr was evenly spread throughout the entire cross-section of the layer without observable significant areas of agglomeration, at least not visible with the available resolution of the used SEM-EDX technique (about 1 μm^3). Therefore, a technique offering higher spatial resolution, below the 1 μm scale, is required to investigate the exact Cr location. For this purpose TEM-EDX (transmission electron microscopy-EDX) was used, as discussed in Section 3.3.4 The uniform elemental distribution of Cr throughout the Cr-exposed LNF-layer, as observed by SEM-EDX, indicates that Cr-species entered the porous LNF-layer via vapor phase transport. The driving force for the Cr-deposition in the LNF-layer can be understood by comparing the enthalpies of formation and the relative thermodynamic stability of the perovskites: $LaCrO_3 > LaFeO_3 > LaNiO_3$ [41], showing that the Cr-containing perovskite is thermodynamically preferred over the LNF-phase.

Fig. 3.7 additionally shows the Ni elemental map which indicates that Ni was also detected everywhere in the layer, as expected on basis of the LNF-composition. However, there was a number of clearly visible spots with high Ni concentration. The locations of these submicron Ni rich spots coincided with particles which had a sharp, cuboid-like appearance as observed in the SEM micrographs (Fig. 3.8). The standard Point-and-Shoot SEM-EDX analysis (with a ~ 1 μm^3 excitation volume) performed on these particles showed a dominance of Ni and O signal in the EDX spectra, indicating the presence of Ni-rich metal oxide, which could be a perovskite, spinel, or pure Ni oxide. In comparison, the reference sample (shown in Fig. 3.2) contained only LNF particles with uniformly distributed elements and no Ni enriched spots

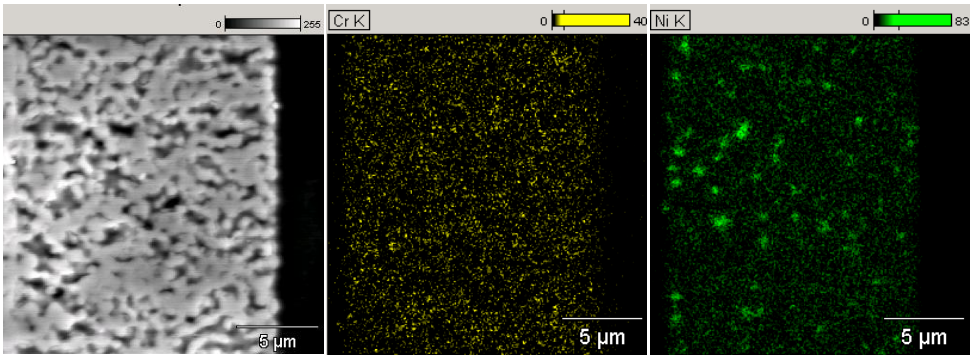

Figure 3.7: SEM-EDX elemental mapping of Cr and Ni throughout the embedded and polished cross-section of the Cr-exposed LNF layer.

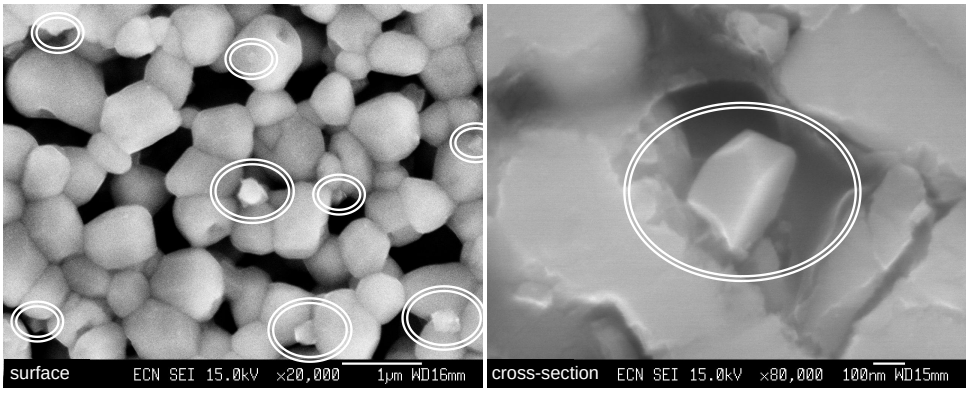

Figure 3.8: SEM micrographs of the surface and the embedded and polished cross-section of Cr-exposed LNF layer. Ni-rich oxide crystals are circumscribed.

could be found. This observation clearly indicates that the incorporation of Cr was accompanied with a segregation of Ni from LNF, resulting in the formation of a Ni-rich secondary oxide phase. The relatively large size of the Ni-rich crystals, found in the pores both on the surface and inside the Cr-exposed porous LNF-layer (see Fig. 3.7 and Fig. 3.8), suggests that Ni could not exclusively originate from the adjacent grains and fast transport of Ni-species seemed to take place either by surface [57] or vapor diffusion mechanism [58–60].

3.3.4 Cr distribution in a Cr-exposed LNF grain

From the sample examined with SEM-EDX (Fig. 3.7 and Fig. 3.8) a section was taken to prepare a TEM-specimen for analysis of the Cr distribution within a single grain. A preliminary TEM screening of different locations was performed in order to select a representative grain for in-depth analyses by bright field TEM imaging (BF-TEM), selected area electron diffraction-TEM (SAED-TEM) and TEM-EDX.

BF-TEM and TEM-EDX

TEM-energy dispersive X-ray spectroscopy (TEM-EDX) in a Point-and-Shoot way (i.e. by focusing the electron beam with a spot diameter of 3.5 nm) was performed on an electron transparent grain, at a distance of 10, 40 and 300 nm from the grain's edge as shown in the bright field TEM image (BF-TEM) in the right part of Fig. 3.9. The measurement was repeated 3 times in close vicinity of each spot to obtain a representative average of the elemental composition. Fig. 3.9 shows the Ni, Fe and Cr concentrations detected in the corresponding distances from the grain's edge. The concentrations in atomic percentages of the A- and B-site constituents of the perovskite ABO_3 (i.e. La, Ni, Fe and Cr) were combined together to 100%. On the basis of these TEM-EDX results it is possible to estimate a composition of the perovskite phase throughout the investigated grain. In the center of the grain (300 nm spot) the approximate perovskite composition was $LaNi_{0.59}Cr_{0.00}Fe_{0.40}O_3$ which is close to the nominal LNF ($LaNi_{0.60}Fe_{0.40}O_3$). This finding proves that the center of the grain was unaffected by Cr. At a distance of 40 nm from the grain's edge the evaluated perovskite composition was $LaNi_{0.39}Cr_{0.24}Fe_{0.36}O_3$. Here, the Fe-content was almost unchanged but Ni was considerably depleted and substituted by Cr. Close to the grain's edge (10 nm spot) the composition was estimated to be $LaNi_{0.17}Cr_{0.54}Fe_{0.28}O_3$, suggesting a slight Fe and a massive replacement of Ni by Cr which then occupied more than 50% of the B-site of the perovskite.

The observed gradients of Ni-, Fe- and Cr-, but constant La-content over the particle cross section, suggest that Cr diffused into the particle, while Ni diffused out of the particle. This result implies that Cr was incorporated into the LNF perovskite lattice as a solid solution.

Electron diffraction (SAED-TEM)

Selected area electron diffraction (SAED) was performed in order to investigate the influence of the incorporated Cr and removed Ni (and Fe) on the crystal structure of the Cr affected grain. Two circles sketched on a BF-TEM image shown in Fig. 3.10A depict locations of the smallest available selected area aperture (210 nm in diameter) for SAED.

Electron diffraction performed in the middle of the sliced grain proved to be the well known rhombohedral crystal structure of LNF (Fig. 3.10B), whereas SAED performed close to the edge of the grain revealed the presence of an orthorhombic perovskite crystal structure (Fig. 3.10C). The spots (marked by red arrows), indicating an orthorhombic symmetry, appeared only when the aperture area of the

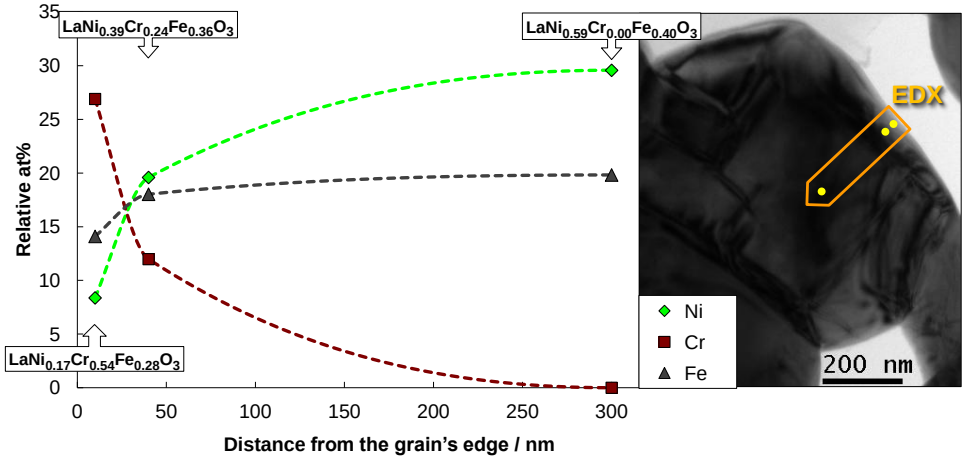

Figure 3.9: Ni, Fe and Cr concentration variations across the sliced Cr-exposed LNF-grain (TEM-EDX). The left figure shows the elemental distribution over the grain distance indicated by the arrow and TEM-EDX spots in the bright field TEM image in the right figure. The shape-preserving spline was used to interpolate the dashed lines connecting elemental concentration values.

SAED was positioned close the grain's edge, which corresponded to the Cr induced structural phase transition from a rhombohedral to an orthorhombic perovskite distortion. A similar Cr impact on the LNF crystal structure was reported in case of solid-state reactivity of chromia with LNF [45, 46] (Chapter 2 of this thesis). All the reflection spots in Fig. 3.10B could be indexed by assuming the rhombohedral cell with the hexagonal lattice parameters a_h=5.5 Å and c_h=13.3 Å, where the suffix h

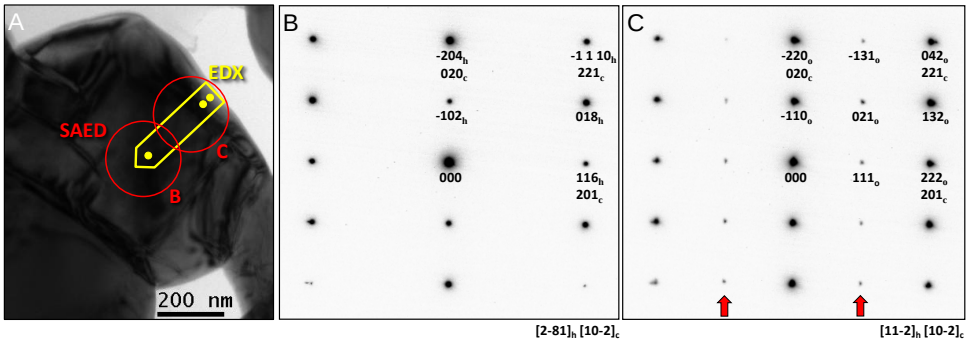

Figure 3.10: SAED patterns of the Cr-poisoned LNF grain collected at room temperature. Incidence of electron is [2 $\bar{8}$ 1]$_h$ of hexagonal lattice and [1 1 $\bar{2}$]$_o$ of orthorhombic lattice both corresponding to [1 0 $\bar{2}$]$_c$ of cubic lattice. The reflection spots indicated by arrows are derived from the orthorhombic lattice.

indicates a hexagonal system. In Fig. 3.10C all the reflections could be indexed as belonging to the orthorhombic cell (suffix *o*) with the parameters: a_o=5.5 Å, b_o=5.5 Å, c_o=7.8 Å. The reflection spots indicated by arrows are typical for the orthorhombic lattice. In Fig. 3.10B and 3.10C the proper orthorhombic and hexagonal indices are also expressed in the cubic settings (suffix *c*). The fact that both SAED patterns can be indexed with the equivalent cubic cell suggests that the perovskite crystal orientation throughout the grain was preserved with only a crystal distortion induced by the Cr- and Ni-cation exchange. The presence of an orthorhombic phase at the edge of the grain and the presence of a rhombohedral phase in the bulk of the grain, detected with SAED at room temperature, corresponds to the observed gradient of Cr and Ni throughout the grain as described in the previous section.

3.3.5 Conductivity evolution and Cr distribution at 600°C

To investigate the impact of the Cr-exposure at lower temperatures, where reaction rates have decreased [45, 46], a similar conductivity experiment was repeated at 600°C. Fig. 3.11 shows the evolution of the electronic conductivity as a function of time for the LNF layer exposed to volatile Cr-species at 600°C. For comparison, Fig. 3.11 contains also the results of the conductivity study at 800°C. Compared to the samples exposed at 800°C, the sample exposed at 600°C exhibited a considerably smaller electronic conductivity drop, namely the electronic conductivity declined slowly in the first 2000 h to reach semi plateau between 2000 and 3000 h of the exposure. Only 30% electronic conductivity was lost after 3000 h of the operation at 600°C, in contrast with the 80% electronic conductivity loss after 380 h at 800°C. An increased effective activation energy, of the small polaron hopping conduction, up to 0.15 eV was also observed after the exposure of 3000 h at 600°C.

Furthermore, SEM-EDX analysis on the Cr-exposed layer at 600°C also demonstrated the presence of small Ni-rich metal oxide crystals, similarly to those which had been observed in the 800°C case. However, the amount of Cr deposited in the layer during 3000 h exposure to volatile Cr-species at 600°C was considerably smaller than during 380 h exposure at 800°C. ICP-OES results showed a huge difference between exposure at 600 and 800°C, with Cr content values of 0.30 at% (after 3000 h at 600°C) and 2.88 at% (after 380 h at 800°C).

The observed deterioration of the electronic conductivity occurring both at 800°C and 600°C suggests that a comparable conductivity degradation mechanism took place at both considered operating temperatures. However, the significant differences in the electronic conductivity loss indicate that the poisoning process was happening at different rates. This could be due to the thermally induced differences: (*i*) in the amount of Cr species released by the Cr-source and/or (*ii*) in the rate of Cr diffusion into the LNF grain. The Cr evaporation rate (*i*) is influenced by the exposure conditions: the partial pressures of different Cr-species, over $Cr_2O_{3(s)}$ in dry air, decrease with temperature [22]. Therefore, vapor supply of Cr into the porous body of the LNF layer is smaller at 600°C than at 800°C. Furthermore, the cation diffusivity in the perovskite lattice (*ii*) is known to decrease substantially with temperature [61]. This accounts for a lower diffusion rate of Cr- and Ni-ions in the

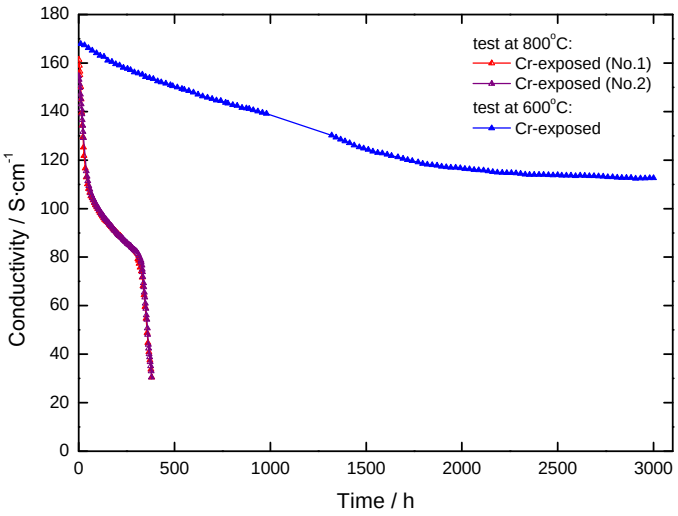

Figure 3.11: The electronic conductivity evolution with time of LNF layers exposed to Cr at 600° C and 800° C.

LNF grains. Consequently, at 600°C the reaction rates and the background pressure of the volatile Cr-species are significantly reduced as all rate limiting processes are thermally activated.

Even at 600°C the electronic conductivity loss is evident (Fig. 3.11) but at a much slower rate. Taking into account that in the present study the Cr-poisoning conditions were deliberately severe, under actual SOFC operation conditions the Cr deposition might be significantly lower due to the continuous airstream. This would lead to a much lower loss rate for the electronic conductivity. Nevertheless, the impact of Cr on the catalytic activity and the surface exchange rate needs further investigation to prove LNF feasibility at 600°C.

3.3.6 Phenomenological description of the conductivity loss

The observed loss in the in-plane electronic conductivity (Fig. 3.4 and Fig. 3.11) of the LNF porous layer, under a constant exposure to a CrO_x rich atmosphere, was clearly due to an exchange between Cr and Ni in the LNF-particles in the porous LNF-layer (Sections 3.3.2 - 3.3.5). The in-plane conductivity of the porous LNF-layer can be described by a percolating network of conducting LNF particles, which are connected to each other by necks, formed during the sintering step in the manufacturing procedure. The smallest repeating unit in such a percolating network is the particle-neck-particle sequence as shown in Fig. 3.12. The Cr-substituted LNF phase, formed in the outer shell of the LNF particles and necks during Cr-exposure (as schematically shown in Fig. 3.12), has a significantly lower electronic conductivity [42, 53] compared to a Ni-rich LNF phase [32, 51].

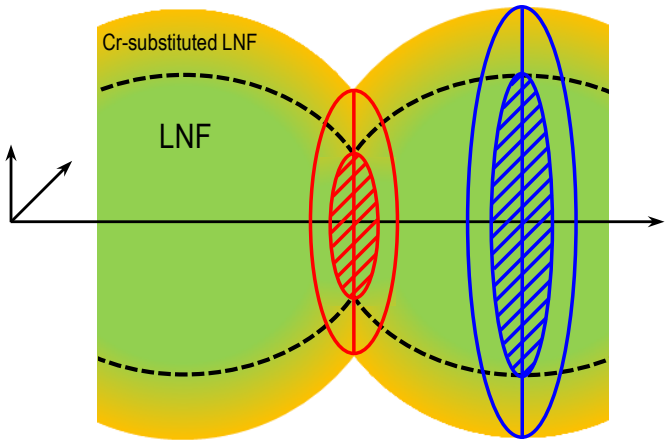

Figure 3.12: A schematic drawing of the Cr-affected LNF particle-neck-particle sequence representing the smallest repeating unit in a percolating network of the porous LNF-layer.

As a consequence the Cr-intrusion results in a lower volume of a well conducting LNF-phase causing a decrease in the overall in-plane conductivity of the porous LNF-layer. When assuming a Cr-intrusion depth of circa 100 nm (Fig. 3.9) it can be calculated (based on Fig. 3.3b) that ∼54% area of the grains' cross-section has been affected by the Cr-intrusion. In addition also the necks between the grains are affected by the Cr-intrusion, where the effect on the neck is expected to be large due to the smaller diameter (Fig. 3.3) and thus a relatively large part of the neck cross-section contains the Cr-containing phase. Indeed, assuming the Cr-intrusion of 100 nm, a simple calculation indicates that ∼73% of the necks' cross-section area is affected by Cr compared to mentioned ∼54% of the grains' cross-section area.

On the base of this phenomenological description of the conductivity loss one can expect that the particle size distribution will have a considerable influence on the rate and the magnitude of the electronic conductivity loss, caused by the volatile Cr-species attack. The microstructure related aspect of Cr-poisoning will be discussed in a follow-up paper [62] (Chapter 4 of this thesis).

3.4 Conclusions

Based on the presented observations the following mechanism has been derived for the impact of Cr-poisoning on the electronic conductivity of the LNF layer:

(1) Cr vapor species directly reacts with LNF at IT-SOFC operating temperatures. The Cr-attack at the LNF grain surface comprises a replacement of Ni by Cr in the perovskite lattice.

(2) The Cr-rich phase transforms from a rhombohedral to an orthorhombic crystal structure, confirming the exchange of Ni by Cr.

(3) The drop in the in-plane conductivity of the porous LNF-layer is caused by a significantly lower electronic conductivity of the Cr-rich phase, made worse at the constricted necks of the grains, where higher concentrations of Cr are likely to exist due to their higher surface to volume ratios.

(4) The segregated Ni, replaced by Cr in the LNF bulk, forms Ni-rich metal oxide precipitates in the pores.

(5) Cr-poisoning impact on the LNF conductivity is smaller at 600°C than at 800°C.

During full SOFC-stack operation, the actual LNF ageing rate, due to Cr-poisoning seems to be significantly lower [17] as the relative area of the Cr-source is much smaller. The continuous air flow will also affect the Cr-background pressure.

Acknowledgements

This work was partly supported by the European Commission, as part of the European Project SOFC600 (SES6-CT-2006-020089), and partly supported by funding from ECN. Adrien Signolet is acknowledged for his involvement in this study during his traineeship at ECN. Jan Pieter Ouweltjes and Wim Haije are thanked for helpful discussions and comments. ECN Engineering & Services (Materials Testing & Consultancy group) is thanked for the SEM-EDX and ICP-OES analysis. Enrico G. Keim (MESA+Institute NanoLab, University of Twente) is gratefully acknowledged for assistance with the TEM analyses.

4 Impact of Cr-poisoning on the conductivity of different $LaNi_{0.6}Fe_{0.4}O_3$ cathode microstructures

The microstructure of porous $LaNi_{0.6}Fe_{0.4}O_3$ (LNF) layers has a significant influence on the degree of the Cr-poisoning impact. The increase off the in-plane resistance and Cr accumulation in poisoned LNF-layers has been correlated with microstructural features. The Cr-poisoning impact is more severe in the case of a microstructure characterized by finer particles, higher porosity and larger particle surface area.

Published in: *Solid State Ionics* (accepted for publication, DOI: 10.1016/j.ssi.2012.04.004)

Presented at: 18^{th} International Conference on Solid State Ionics; July 2011, Warsaw, Poland (*talk*; *student award*)
PhD Workshop on Materials for Sustainable Energy; June 2011, Ameland, The Netherlands (*poster*)

4.1 Introduction

The perovskite $LaNi_{0.6}Fe_{0.4}O_3$ (LNF) is being considered as a possible cathode and interconnect coating material for intermediate temperature SOFC (IT-SOFC) systems where relatively cheap interconnect materials, such as chromia-forming ferritic stainless steels, are used. High electronic conductivity, thermal expansion coefficient matching that of zirconia [32] and claimed high Cr-resistance [11, 14, 16] are the properties of LNF that enable its use as cathode current collecting layers, interconnect protective coatings and/or electrochemically active cathode layers. Furthermore, using the LNF material as a cathode is recommended for metal-supported SOFCs [43], due to the claimed high Cr-tolerance and good electrochemical performance obtained for LNF sintered at low temperatures [44].

However, an actual Cr-tolerance of the LNF material is debatable and controversial in the view of recent findings. Previous studies [45, 46] have demonstrated the occurrence of solid-state reactivity of LNF with chromia at 800°C. It has been found that LNF is chemically unstable at 800°C when it is in direct contact with Cr_2O_3 as Cr-cations enter the perovskite phase replacing Ni- and Fe-cations. Other studies [63, 64] (Chapter 3 of this thesis) showed a significant impact of Cr on the electronic conductivity of an LNF porous cathode layer at 800°C. Vapor transport of Cr-species, originating from a porous metallic foam, and subsequent reaction with LNF resulted in a decrease of the electronic conductivity of the LNF layer. Cr-attack at the LNF grain surface resulted in a replacement of Ni by Cr in the perovskite lattice. Formation of a Cr-substituted LNF phase, with a significantly lower electronic conductivity, has led to a serious deterioration of the in-plane conductivity of the porous LNF layer.

In the later study it has also been anticipated that the particle size distribution would have a considerable influence on the rate and magnitude of the electronic conductivity loss [64]. Therefore, the role of the microstructure on the conductivity deterioration is a subject of the present work. To create a wide range of samples with different micro-structural parameters (porosity, internal surface area, etc.) two sets of the LNF powder with different morphology were sintered at different temperatures.

To analyze and compare different LNF microstructures a proper quantitative micro-structural analysis method has to be chosen. In the present study a 2D SEM approach has been used. The investigated samples were represented by a simple binary system: LNF particles (black) and pores (white). The 2D SEM micrographs provided sufficient quantitative microstructural information allowing the relative comparison of different LNF layers. The degree of Cr-poisoning and the in-plane resistance increase of the LNF layer has been directly correlated with the quantitative microstructural features.

4.2 Experimental

4.2.1 Sample preparation

LNF layers were prepared using $LaNi_{0.6}Fe_{0.4}O_3$ powder (Praxair, 99.9% purity). The mechanical support used during the conductivity measurements was composed of a tape cast 3 mol% yttria stabilized zirconia (3YSZ) layer. The 3YSZ layer was sintered at 1500°C for 1 h resulting in an electrolyte disc of 25 mm diameter and 90 μm thickness. The sintered 3YSZ layer was subsequently covered with a 2 μm $Gd_{0.4}Ce_{0.6}O_{1.8}$ (GDC) barrier layer by means of screen printing followed by sintering at 1300°C for 1 h. To obtain LNF layers with different microstructures the following variations were introduced: (*i*) the as received LNF powder was pretreated by a calcination step at 800°C for 1 h in air, (*ii*) the particle size and the degree of LNF powder dispersion in the screen print paste (powder dispersed in an alcohol-binder solution) was varied by introducing a milling step using a Dispermat (VMA-Getzmann GmbH) milling system, (*iii*) the obtained LNF pastes (LNF-paste-I and LNF-paste-II) were screen printed on top of the GDC barrier layer and sintered in air either at 1150 or 1250°C for 1 h. Based on these variations $(i) - (iii)$ four microstructures were selected and referred to as: LNF-A (calcined, milled, 1250°C), LNF-B (calcined, milled, 1150°C), LNF-C (as received, unmilled, 1250°C), LNF-D (as received, unmilled, 1150°C). Resulting LNF perovskite layers formed a 10 mm wide strip with a thickness in a range of $15-25$ μm. To allow measurements of the LNF layer resistance gold contacts were attached as described elsewhere [34, 63].

4.2.2 Resistance measurements

The resistance measurements procedure has been presented in the previous publication [64] (Chapter 3 of this thesis). For Cr-poisoning experiments (exposure in dry air at 800°C for 300 h) an ITM-14 ferritic FeCr-based alloy in the form of a porous foam (Plansee AG, Reutte, Austria [49]) was used as a Cr source. For each of the Cr-poisoning experiments a freshly cut and pre-oxidized ITM-14 foam was used. Details of the ITM-14 samples treatment were described in Chapter 3 of this thesis.

4.2.3 Microstructural and compositional characterization

To characterize the porosity of LNF-layers two different approaches were used. The macroscopic geometrical porosity was obtained from the density of the LNF layer which was calculated from geometrical dimensions, measured weight and the theoretical density of $LaNi_{0.6}Fe_{0.4}O_3$. On a microscopic level the microstructural porosity was determined by the 2D image analysis (ImageJ software [50]) of SEM micrographs (JEOL JSM 6330F FEG-SEM) of the LNF layers' surface.

The elemental composition of the LNF-layers exposed to Cr volatile species was obtained by scraping off the LNF-layer and analyzing the elemental composition of the resulting powder by means of inductively coupled plasma-optical emission spectroscopy (ICP-OES), using a Varian Vista AX PRO CCD.

4.3 Results and Discussion

4.3.1 Microstructure characterization

Table 4.1 presents values of the geometrical porosity and the microstructural porosity for different LNF layers. LNF layers manufactured with a calcined and milled LNF powder (LNF-paste-I) were less porous compared to LNF layers prepared out of as received and unmilled LNF powder (LNF-paste-II) for each of the sintering temperature (1150 and 1250°C). The calcination improved milling efficiency of the LNF powder which led to an increase in the sintering activity, manifested by obtaining lower porosities and thinner layers.

As shown in Fig. 4.1, the higher sintering temperature of 1250°C for both LNF-pastes (samples LNF-A and LNF-C) resulted in a more intensive grain growth. Thus broader necks and larger grains were formed. In case of layers sintered at the lower temperature of 1150°C necks and grains were small and abundant (samples LNF-B and LNF-D). Furthermore, samples LNF-A and LNF-B prepared using LNF-paste-I possessed a homogenous and continuous microstructure. However, in the case of samples LNF-C and LNF-D, manufactured using LNF-paste-II, for which the as received powder was agglomerated, the sintering between LNF crystallites within the agglomerates occurred at lower temperatures than the sintering between the agglomerates. The sintering of the crystallites inside the agglomerates formed large and separate particles, which led to an inhomogenous microstructure with large cavities, as observed in Fig. 4.1 for samples LNF-C and LNF-D.

Layer preparation				
Powder treatment	calcined		as received	
Paste	milled and mixed		unmilled, only mixed	
	LNF-paste-I		LNF-paste-II	
Sintering temperature (°C)	1250	1150	1250	1150
LNF-i layer type	LNF-A	LNF-B	LNF-C	LNF-D
Microstructural features				
Geometrical porosity (%)	31	39	45	53
Layer thickness T (μm)	16	21	18	22
Microstructural porosity (%)	22	25	29	34
Cr-content $^{(300\text{ h exposure at }800°C)}$ (at%)	0.8	3.8	3.1	4.3
$f\%^{300h}_{bulk_i Cr-aff}{}^{(125\text{ nm Cr-intrusion})}$(%)	33	58	42	70

Table 4.1: Summary of the characteristics of different LNF-i microstructures (i=A−D)

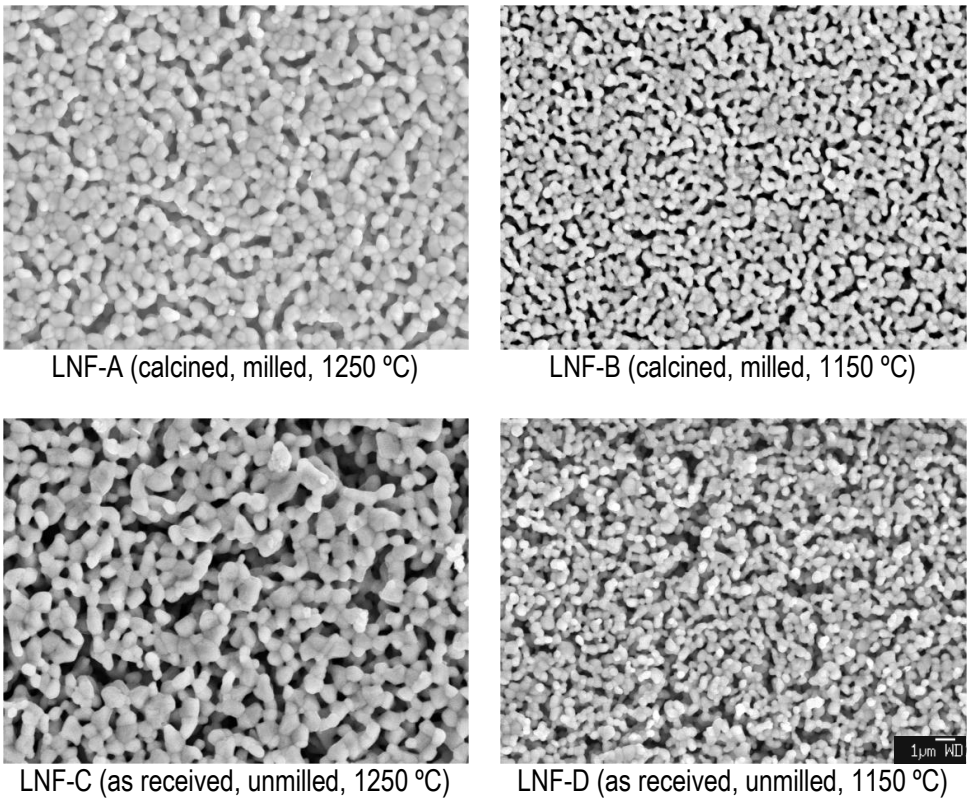

Figure 4.1: SEM micrographs of the four different microstructures of LNF layers.

4.3.2 Correlation of Cr-content with microstructure of the LNF-layer

The Cr-content, after 300 h exposure to volatile Cr-species, was obtained for four different LNF-layers by means of an ICP-OES method (Table 4.1). In order to correlate the observed Cr-content with the different micro-structural features of the LNF-layers a simple approach was taken. In this approach the main important assumption is that the surface of the LNF-bulk of four different LNF-layers was identical in its chemical behavior towards Cr-incorporation. Therefore, the Cr-intrusion into the LNF-particles, after a certain exposure period, was assumed to be the same for all microstructures. An exposure time of 300 h results in a Cr-affected volume of the LNF-particles corresponding to an intrusion depth of circa 125 nm [64]. Consequently, the available Cr-exposed LNF surface area in the four different LNF-microstructures determines the overall extent of the Cr-affected volume of the LNF bulk. In order to determine the impact of the microstructure on the amount of incorporated Cr, it is important to obtain a quantitative description of the Cr-affected volume of the LNF-bulk. The quantification of the Cr-affected volume was

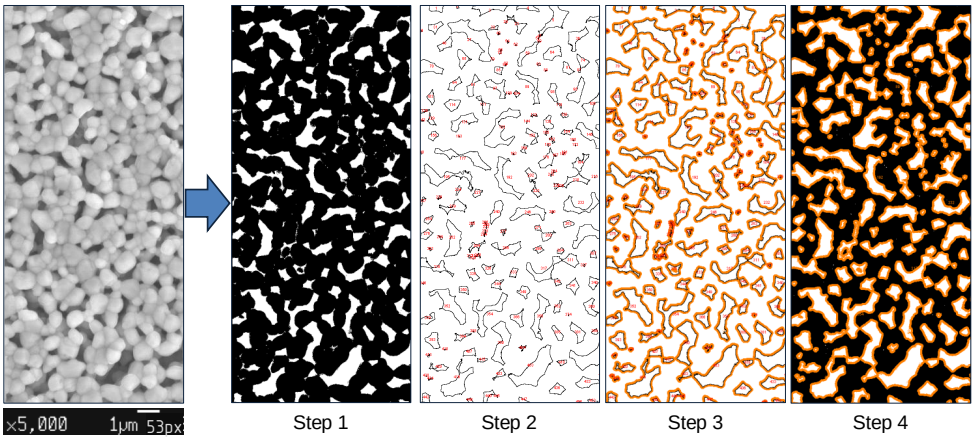

Figure 4.2: Steps involved in the image processing of the SEM micrograph.

obtained using SEM micrographs (Fig. 4.1), which were digitally processed with the ImageJ software. The steps in the image processing sequence (Fig. 4.2) and the quantification of the Cr-affected volume of the LNF-bulk were:

- Step 1) SEM micrographs were binarized by automatic thresholding (isodata algorithm [50]) assigning a black area to the LNF bulk and a white area to the pore. Then the microstructural porosity was determined as a $(pore\ area)/(total\ area)$ ratio.
- Step 2) The threshold data were analyzed with the 'Analyze Particles' command. In the 2D-image pores were regarded as "particles" because they were occupying less than 50% of the analyzed frame area and were separated by the interconnected LNF bulk area. For each of the pores larger than 4 pixels an individual object number and an outline was automatically assigned. Each pore's outline represents the LNF-surface, which can react with volatile Cr-species during the Cr-exposure.
- Step 3) Each pore's outline, as obtained in step 2, was enlarged (orange area) by the given value of the Cr-intrusion depth, giving a representation in the 2D plot of the Cr-affected volume of the LNF-bulk.
- Step 4) The obtained orange area was overlaid on the black area of the bulk (determined in step 1) representing ipso facto the Cr-affected volume of the LNF-bulk. The fraction of the LNF-bulk affected by Cr ($f\%_{bulk\ Cr-aff}$), being the ratio between the Cr-affected LNF bulk ($A_{bulk\ Cr-aff}$) and the initial unaffected LNF bulk (A_{bulk}), should correlate with the amount of incorporated Cr according to the following relation:

$$f\%_{bulk_i\ Cr-aff} = \frac{A_{bulk\ Cr-aff}}{A_{bulk}} = \frac{\text{orange area}}{\text{black area}} \propto Cr\ content. \qquad (4.1)$$

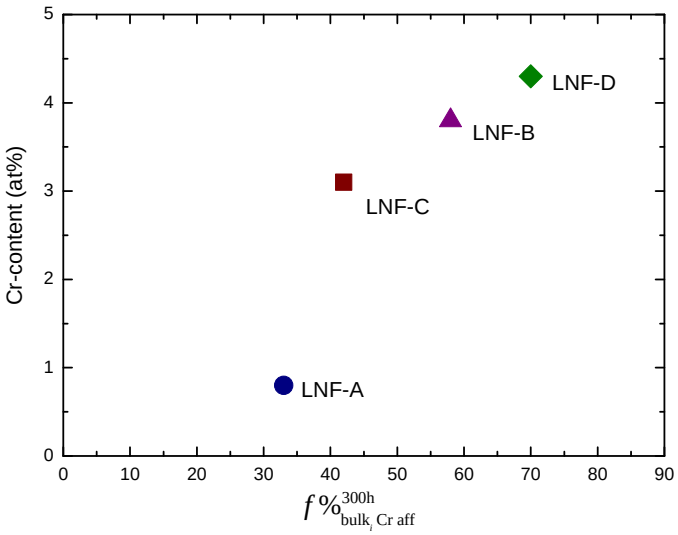

Figure 4.3: Correlation of the amount of incorporated Cr into the bulk of LNF after 300 h with the calculated fraction of the Cr-affected area of the LNF bulk.

As observed in Fig. 4.3, the amount (in at%) of the incorporated Cr into the bulk of LNF after 300 h exposure (Table 4.1) correlates well with the calculated fraction of the Cr-affected LNF bulk area ($f\%^{300h}_{bulk_i\ Cr-aff}$) (Table 4.1), validating the proposed approach and the relationship (4.1).

4.3.3 Correlation of in-plane resistance with microstructure of the LNF-layer

In order to correlate the layer resistance, in the Cr-free case (time 0 h) and in the Cr-intrusion case (time 300 h), with the layer microstructure the following considerations have to be taken into account:

Firstly, the resistance of a dense LNF-layer (R_d) is expressed as:

$$R_d = \varrho \frac{L}{A} = \varrho \frac{L}{(T \cdot W)}, \tag{4.2}$$

where ϱ denotes resistivity of the LNF-bulk, L is the length between contacts, and A represents the cross-sectional area of the dense bulk (A equals to the width W times the thickness T).

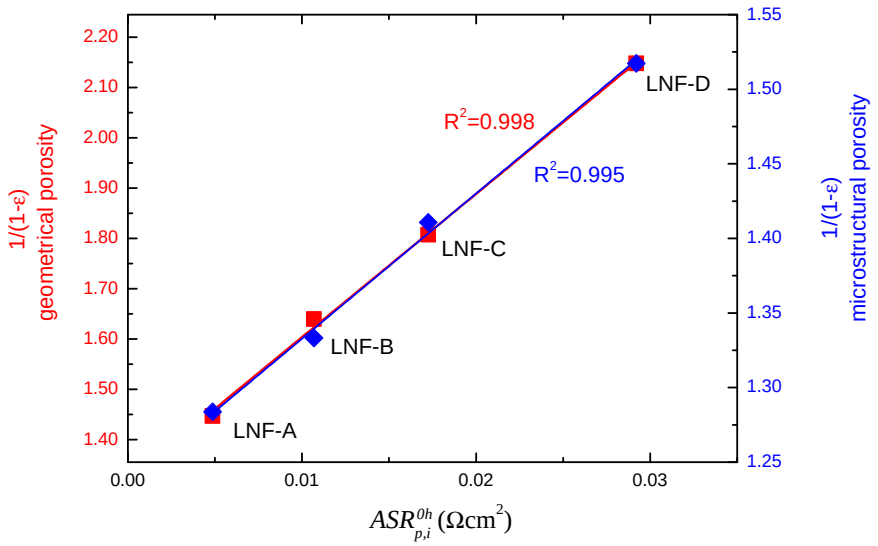

Figure 4.4: Correlation of the resistance of different porous LNF-i layers obtained at time 0 h (Cr-free case) as a function of variable microstructure parameters.

Secondly, the resistance of the porous LNF-layer with a fractional porosity ε, which has not been affected by Cr, is expressed as:

$$R_p^{0h} = \varrho \frac{L}{A_{bulk}^{0h}} = \varrho \frac{L}{(W \cdot T) \cdot (1 - \varepsilon)}, \tag{4.3}$$

where A_{bulk}^{0h} is defined as the cross-sectional area corrected for the porosity. This is a first order approximation of the influence of the porosity on the in-plane electrical resistance, though some more complex formulations have been also reported in the literature [65, 66].

For the four different LNF-i layers (i $\in$ {A,B,C,D}) ϱ, L, W are constant, but T and ε varies due to differences in the microstructure. Therefore, by introducing the cross-sectional area specific resistance $ASR_{p,i}^{0h}$, which equals $R_{p,i}^{0h} \cdot W \cdot T_i$, Equation (3) can be conveniently expressed as:

$$ASR_{p,i}^{0h} = \varrho L \cdot \frac{1}{1 - \varepsilon_i}. \tag{4.4}$$

Thirdly, the resistance of a porous LNF-layer after 300 h of Cr-exposure can be expressed using modified Equation (4.3) as:

$$R_p^{300h} = \varrho \frac{L}{A_{bulk}^{0h} - A_{bulk\ Cr-aff}^{300h}}. \tag{4.5}$$

The Cr-affected area ($A^{300h}_{bulk\ Cr-aff}$) is assumed here as non-conductive, because $\varrho_{LNF-Cr} \gg \varrho_{LNF}$ (0.02 Ωcm ≫ 0.0017 Ωcm) [64], resulting effectively in a decrease of the cross-sectional area of the highly conductive LNF phase.

Assigning again $f\%^{300h}_{bulk\ Cr-aff} = A^{300h}_{bulk\ Cr-aff}/A^{0h}_{bulk}$ (similarly as in Equation (4.1)), one can rewrite Equation (4.5) as:

$$R^{300h}_{p} = \varrho \frac{L}{A^{0h}_{bulk} \cdot (1 - f\%^{300h}_{bulk\ Cr-aff})}, \tag{4.6}$$

which can be further simplified, by replacing ϱ with Equation (4.3), which results for the different LNF-i layers in the final expression:

$$R^{300h}_{p,i} = \frac{R^{0h}_{p,i}}{(1 - f\%^{300h}_{bulk_i\ Cr-aff})}. \tag{4.7}$$

Equation (4.7) allows the estimation of the resistance at time 300 h based on the input data of the measured resistance at time 0 h and the fraction of the Cr-affected bulk at time 300 h as obtained from the image analysis in Table 4.1. This allows comparison between the measured and the calculated resistance at time 300 h.

Resistance as a function of microstructure at time 0 h (Cr-free case)

Fig. 4.4 presents the correlation of the resistance for different porous LNF-i layers obtained at time 0 h as a function of variable microstructure parameters according to Equation (4.4). This correlation holds very well for both geometrical porosity values as well as the microstructural porosity values (Table 4.1). Such a good agreement validates the use of the 2D image analysis approach.

Resistance evolution in Cr-containing atmosphere for different microstructures

Fig. 4.5 shows the resistance evolution in time for different porous LNF-i layers exposed at 800°C in dry air to an ITM-14 Cr-source. All LNF-i layers exhibited a significant increase of the in-plane resistance within the first 50 h. Subsequently, a semi-linear resistance increase occurred in the time period of 100-300 h. The LNF-i layers were exposed only for 300 h as the previous study [64] reported a change in the evaporation behavior of the porous ITM-14 foam above 320 h.

The simulated values of the resistance at time 300 h ($R^{300h}_{p,i}$), calculated according to Equation (4.7), showed a relatively good agreement with the measured resistance values at time 300 h (Fig. 4.5). The proposed approach (Section 4.3.3) helps to understand the observed differences in the resistance increase for different LNF-i layers. The extent of the resistance increase depended on the fraction of the Cr-affected LNF bulk area, which related with the microstructure. Therefore, the parameter $f\%^{300h}_{bulk_i\ Cr-aff}$ reflected a susceptibility of the given microstructure to the Cr incorporation.

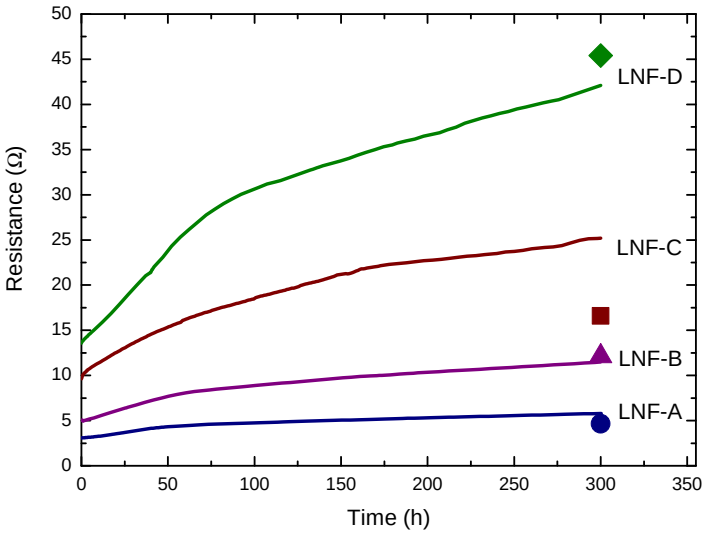

Figure 4.5: Measured resistance evolution in time (solid line) of different LNF-i layers exposed to volatile Cr species in dry air at 800° C. The colored symbols depict simulated values of resistance at time 300 h according to Equation (4.7).

However, in the case of sample LNF-C the simulated resistance increase is underestimated. This might be due to the fact that in the current approach the tortuosity and the grains' connectivity was not taken into account. Compared to other samples, the microstructure of the LNF-C sample (Fig. 4.1), is inhomogeneous with large cavities, poor grain connectivity and fewer percolation pathways, which probably contributes much more to the total resistance increase.

4.4 Conclusions

The proposed 2D image analysis approach, to correlate the impact of Cr-poisoning on different LNF microstructures, turned out to be successful. Especially, the calculated fraction of the Cr-affected area correlates well with the measured Cr-content and also gives satisfactorily explanation for the observed differences in the resistance increase for different LNF-*i* layers. The fraction of the Cr-affected LNF bulk area characterizes well different microstructures from the view point of the Cr-poisoning susceptibility. This parameter $f\%_{bulk\ Cr-aff}$ reflects the microstructural porosity, particle size and the length of the outline of the LNF bulk, which corresponds with the exposed particle surface area. Therefore, this approach proved, explained and justified that the Cr-poisoning impact, in terms of the resistance increase and the Cr-accumulation, is more severe in case of microstructure characterized by finer particles, higher porosity and larger particle surface area. This conclusion is presented schematically in Fig. 4.6, where two microstructural extremes (LNF-A and LNF-D) are shown.

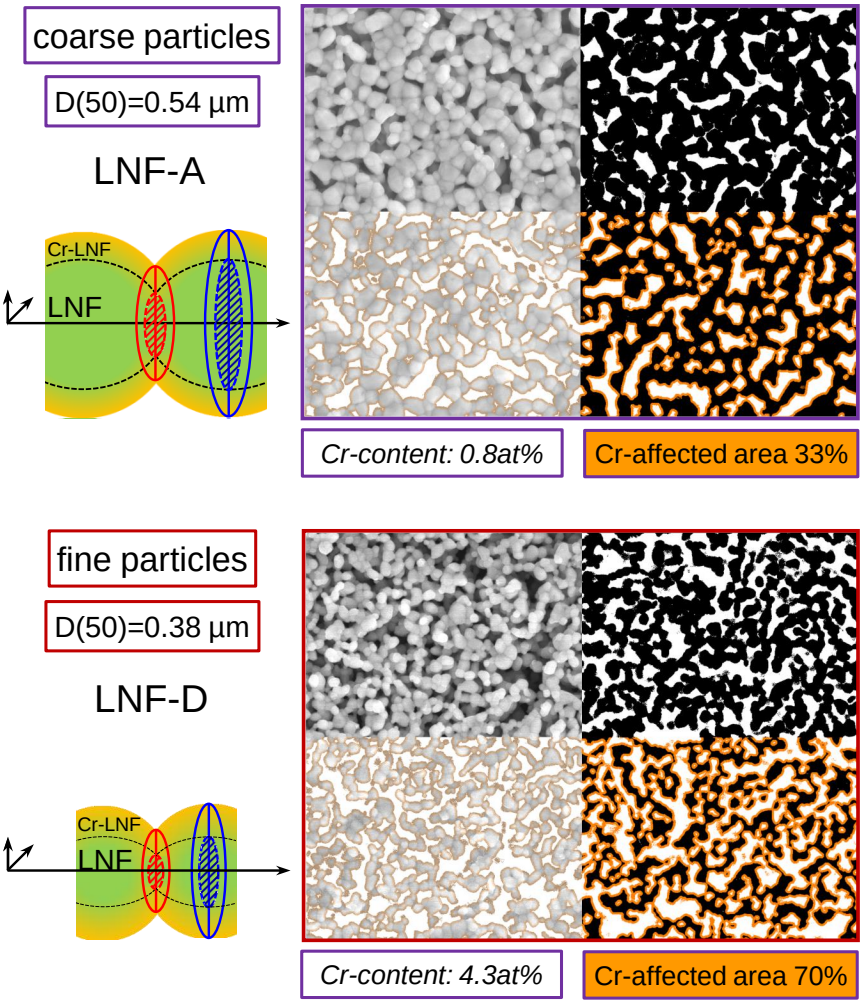

Figure 4.6: Schematic representation of the Cr-poisoning impact on the two microstructural extremes (LNF-A and LNF-D).

The observed different Cr impact on different LNF microstructures could suggest that a microstructure with coarse particles and low surface area would be most Cr-tolerant. However, this study only considers the Cr impact on the in-plane resistance increase and the Cr-accumulation. In the electrochemically operated LNF cathode, the actual Cr-poisoning impact in terms of the overall cell performance degradation could be different (as shown in Chapter 5).

4.5 Appendix: Conductivity evolution in different Cr-containing atmospheres

Motivation

The use of untreated air as the cathode gas has been reported to be the most simple option for operating an SOFC system. It has been shown, however, that moisture in any supplied air significantly accelerates the degradation due to Cr-poisoning [4, 6, 22]. In this section, the influence of moisture and oxygen content on the rate of Cr-poisoning of LNF cathode layers is presented. In literature it has been shown that the gas phase concentration of Cr-species is strongly dependent on the composition of the atmosphere; increasing oxygen and/or water content increases the concentration of volatile Cr-species [10, 22]:

- in dry air:

$$Cr_2O_{3(s)} + 3/2\ O_2 \rightarrow 2CrO_{3(g)} \tag{4.8}$$

- in humidified air:

$$Cr_2O_{3(s)} + 3/2\ O_2 + 2H_2O \rightarrow 2CrO_2(OH)_{2(g)} \tag{4.9}$$

Consequently, lowering the oxygen partial pressure and/or water content is expected to reduce the supply of Cr-species and hence the rate of Cr-poisoning.

Gas atmospheres

As described in Chapter 3 and 4, the rate of Cr-poisoning was monitored through measurement over time of the in-plane electronic conductivity of a porous LNF cathode layer. Each freshly prepared LNF sample, with the same microstructure (LNF-B), was heated in a quartz tube to the operating temperature of 800°C. Also a freshly cut and pre-oxidized ITM-14 foam was used and positioned as shown in Fig. 3.1.

Under standard conditions, the quartz tube was flushed with dry synthetic air (20% O_2 (purity 99.6%, <7ppmv H_2O) and 80% N_2 (purity 99.999%, <4ppmv H_2O)) at a total flow rate of 100 ml/min.

To evaluate the influence of moisture, the quartz tube was flushed with humidified air. The humidification was performed by passing dry synthetic air through a water bubbler kept at 29°C. This resulted in a water content of circa 4% in volume.

To investigate the influence of the reduced oxygen content, the quartz tube was flushed with dry nitrogen mixed with 0.4% O_2 at a total flow rate of 500 ml/min. This high flow was required to maintain basically the same low amount of oxygen over time.

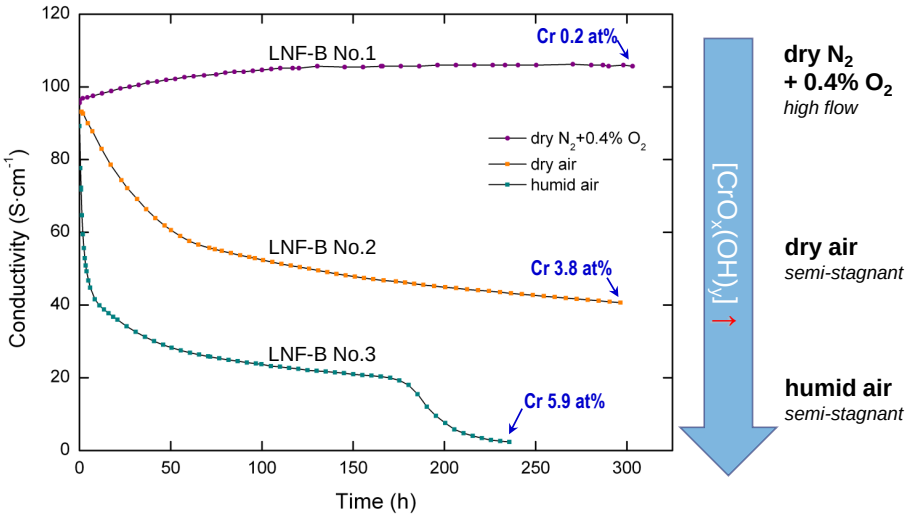

Figure 4.7: The electronic conductivity evolution at 800° C for the LNF-B layers exposed to a Cr-source in different atmospheres. The amount of Cr deposited in these layers was obtained by the ICP-OES method and is given as La+Ni+Fe+Cr=100 at%.

Conductivity evolution in different Cr-containing atmospheres

Fig. 4.7 shows the electronic conductivity evolution with time at 800°C of the LNF-B layers in various atmospheres. It can be seen that the Cr impact on the electronic conductivity of the LNF-layers is strongly influenced by the atmosphere. This is clearly related to the gas phase concentration of Cr species which depends on both the PO_2 level and humidity (Equations (4.8) and (4.9)).

In the presence of the Cr-source (pre-oxidized ITM-14 metallic foam), the electronic conductivity of the LNF-layer (sample LNF-B No.1 in Fig. 4.7) remained nearly unaffected when exposed to the atmosphere of dry nitrogen mixed with 0.4% oxygen (PO_2=4×10^{-3}atm) for a testing period of 300 h.

In the case of the LNF layer (LNF-B No.2) exposed to the Cr-source in dry air, a significant loss in the electronic conductivity was observed within the first 50 h, and then the rate of the conductivity decline slowed down in the time period of approximately 100-300 h (as also shown in Chapter 4 in terms of resistance increase (Fig. 4.5)).

The LNF sample (LNF-B No.3) exposed to the Cr-source in humidified air showed an immediate and substantial loss in the electronic conductivity just within the first 10 h, followed by a semi-linear conductivity decline in the time period of circa 50-170 h. Subsequently, a second steep conductivity drop appeared after 180 hours of the exposure. Probably this second drop in the conductivity reflected the moisture accelerated change of the surface of the ITM-14 foam from $(Mn,Cr)_2O_4$ to pure Cr_2O_3 scale, which results in higher concentration of volatile Cr-species [19, 20, 22, 56], similarly to the recorded observations after 300 h exposure in air [64] (Chapter 3 of

this thesis). This result indicates that the concentration of volatile Cr-species was significant larger than in dry air, leading to an intensification of the transport of Cr into the bulk of the LNF layer. This is also supported by the observed substantial conductivity loss. The presence of water vapor had, therefore, dramatic influence on the Cr-poisoning mechanism. This includes the impact on the Cr-source, concentration of volatile Cr-species and the attack at the LNF surface.

The variations in the gas atmospheres, in the case of testing in a Cr-free environment, had no impact on the stability of the electronic conductivity of all samples tested for about 150 h.

Cr accumulation in different Cr-containing atmospheres

The Cr-content of the exposed LNF-layers was obtained by ICP-OES analysis of the powders that were scraped-off the samples. The values obtained for the different testing atmospheres are presented in Fig. 4.7 as cation %.

A Cr-content of merely 0.2 at% detected in the sample LNF-B No.1 indicated that in dry nitrogen with 0.4% oxygen, equivalent to PO_2=4×10^{-3}atm, the concentration of volatile Cr-species was low, resulting, in turn, in very low Cr-deposition and unnoticeable electronic conductivity loss during the testing period of 300 h.

In dry air, however, volatile Cr-species originated from the Cr-source and diffused to the body of the porous LNF layer (LNF-B No.2). This resulted in the accumulation of Cr, reaching 3.8 at% after 300 h, and a related significant loss in the electronic conductivity.

In the sample exposed to the Cr-source in humidified air (LNF-B No.3) the Cr-content reached 5.9 at% already after 235 h. This result indicates that the concentration of volatile Cr-species was significantly higher, leading to a greater rate of reaction of Cr with the bulk of the LNF layer. This is also supported by the observed substantial loss in conductivity. The presence of both water vapor and atmospheric concentrations of oxygen has, therefore, a dramatic influence on the Cr-poisoning mechanism.

The reaction at the surface of the Cr-source is controlled by the content of the atmosphere (PO_2 and humidity) which in consequence determines the concentration and type of Cr-species.

Outlook

The Cr-poisoning impact on the LNF conductivity is very pronounced when humidified air is used, indicating that the concentration of volatile Cr-species is significantly increased. On the other hand, using dry nitrogen with 0.4% oxygen resulted in a negligible transport and Cr deposition, therefore the LNF conductivity remained unaffected.

The results presented in this Appendix, show the extreme impact of the humid conditions on the deterioration of LNF conductivity due to enhanced Cr-poisoning. This emphasizes the need for moisture removal from the cathode gas stream.

Acknowledgements

This work was partly supported by the European Commission, as part of the European Project SOFC600 (SES6-CT-2006-020089), and partly supported by funding from ECN. Adrien Signolet is acknowledged for his involvement in this study during his traineeship at ECN. Wim Haije is thanked for helpful discussions. ECN Engineering & Services (Materials Testing & Consultancy group) is thanked for the SEM and ICP-OES analysis.

5 Cr-poisoning of a $LaNi_{0.6}Fe_{0.4}O_3$ cathode under current load

This study demonstrates the significant impact of Cr-poisoning on the performance of the $LaNi_{0.6}Fe_{0.4}O_3$ (LNF) SOFC cathode under current load. Volatile Cr-species, originating from a porous metallic foam, enter the working electrode and modify both the LNF cathode layer and the $Gd_{0.4}Ce_{0.6}O_{1.8}$ (GDC) barrier layer, causing increasing overpotential and cell impedance. The increase of the ohmic resistance is caused by a decrease of the in-plane electronic conductivity of the LNF layer (due to Cr incorporation and Ni removal from the LNF perovskite lattice) combined with a deterioration of the ionic conductivity of the GDC barrier layer due to reactivity with Cr resulting in formation of a $GdCrO_3$-phase. The increase of the polarisation resistance is caused by a decrease of the electrochemical activity of the LNF surface towards oxygen reduction reaction at the triple phase boundary (TPB) due to Cr-incorporation in the outer shell of the LNF grains. Chemical reaction and electrochemically-driven reaction of volatile Cr-species with LNF and GDC contributes to the extrinsic degradation of the LNF cathodes under current load.

Published in: *Journal of Power Sources* **209C** 120-129 (2012)

Presented at: 2^{nd} International Workshop on Degradation Issues of Fuel Cells, September 2011, Thessaloniki, Greece (*invited talk*)

5.1 Introduction

The perovskite $LaNi_{0.6}Fe_{0.4}O_3$ (LNF) has been considered as a candidate cathode and interconnect coating material for various intermediate temperature SOFC (IT-SOFC) systems where relatively cheap interconnect materials such as chromia-forming ferritic stainless steels are used. High electronic conductivity and a thermal expansion coefficient matching that of zirconia [32], together with claimed high Cr-resistance [11, 14, 16] are the properties of LNF that enable its use as current collecting layer, interconnect protective coating and/or electrochemically active cathode layer. In the context of Cr-tolerance, LNF has a claimed advantage of not being composed of the so-called Cr-nucleating-agents [15], like Mn^{2+} or SrO, which are inducing Cr-deposition (as reported for LSM or LSCF cathodes [12, 13, 15]).

However, previous studies regarding the actual Cr tolerance of LNF have demonstrated the occurrence of solid state reactivity of LNF with chromia at 800°C [45, 46] (Chapter 2). It has also been found that volatile Cr species directly react with a porous LNF layer at IT-SOFC operating temperatures [63, 64]: This reaction results in a replacement of Ni by Cr in the LNF perovskite lattice. One of the observed consequences of this replacement of Ni by Cr is a decrease of the in-plane electronic conductivity of the LNF porous layer [64] (Chapter 3).

In the present study the impact of volatile Cr species on the electrochemical properties of a $LaNi_{0.6}Fe_{0.4}O_3$ cathode has been investigated under current load, aiming for an evaluation of the reliability of a LNF cathode operating in a Cr-containing environment, such as in an IT-SOFC stack (Fig. 1.4). To accelerate the Cr-poisoning impact, a Cr-containing porous interconnect foam has been used, which is distinctively different from a dense interconnect alloy employed in a real stack situation.

In order to unambiguously observe the degradation of the Cr-exposed LNF cathode under electrochemical operation, a special set-up was required. Reliable three-electrode measurements, facilitating a square planar geometry with coplanar reference electrodes, allowed insight into the cathode degradation under stationary conditions (400 mA/cm^2 at 800°C). Changes in the overpotential and the evolution of the electrochemical impedance spectra of the working LNF electrode were monitored over a time period of 1000 h. The accuracy of the three-electrode measurements has been assured by virtually perfect electrodes alignment, obtained with precise laser-ablation trimming of the edges of the electrodes.

Based on the analysis of the electrochemical impedance and electronic conductivity measurements, together with detailed post-mortem analyses on the Cr-exposed sample, a mechanism is proposed for the Cr-poisoning of $LaNi_{0.6}Fe_{0.4}O_3$ (LNF) cathodes under current load.

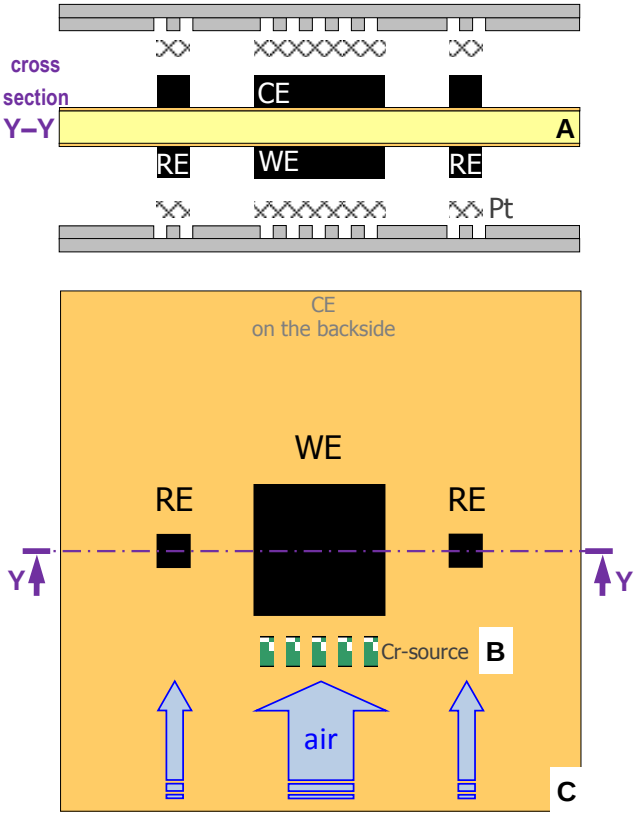

Figure 5.1: Endurance testing of the LNF cathode as the working electrode (WE) was performed in a 'three-electrode set-up' (A) for a Cr-free case and with a Cr-source added (B).

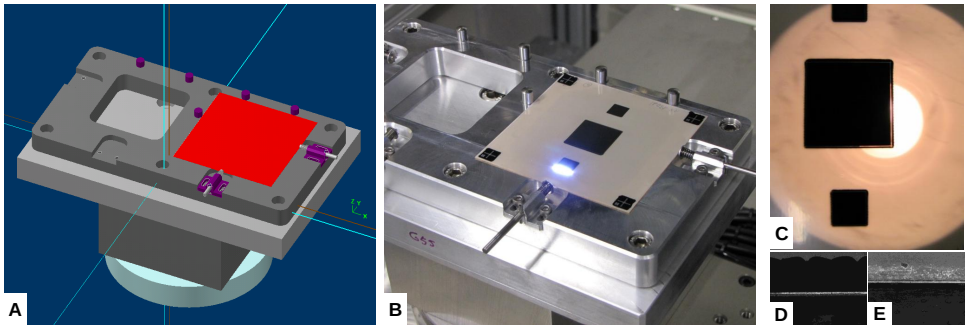

Figure 5.2: Laser aided electrode alignment.

5.2 Experimental

5.2.1 Sample preparation

LNF cathode layers were prepared using a commercial $LaNi_{0.6}Fe_{0.4}O_3$ powder (Praxair, 99.9% purity). A 3 mol% yttria stabilized zirconia (YSZ) electrolyte, providing the mechanical support, was prepared by tape casting and sintering at 1500°C for 1 h. The electrolyte squares, with dimensions 80 mm × 80 mm and 150 μm thickness, where subsequently covered on both sides with 2 μm thick $Gd_{0.4}Ce_{0.6}O_{1.8}$ (GDC) barrier layers by means of screen printing, followed by sintering at 1300°C for 1 h. The LNF powder, after precalcination at 800°C for 1 h in air, was milled and dispersed into an alcohol-binder solution using a Dispermat (VMA-Getzmann GmbH) milling system. The LNF paste was screen printed on top of the GDC barrier layer on both sides of the electrolyte in a pattern shown in Fig. 5.1.

A perfectly aligned working electrode (WE) and counter electrode (CE), vital for a coplanar reference electrode geometry [67–71], was successfully obtained by laser aided trimming of the electrode edges. A special chuck (sample holder/clamp) was designed (Fig. 5.2A) to precisely reverse the electrolyte providing a high spatial accuracy of the laser trimming on both sides of the sample (as shown in Fig. 5.2). Dried, but not sintered, LNF layers were trimmed with the third harmonic of Nd:YAG laser (355 nm) (Rofin-Baasel). A groove of 60 μm width and circa 40 μm depth was obtained by laser ablation (Fig. 5.2B shows laser in operation). The surplus of LNF material outside the groove (Fig. 5.2C and D) was removed from the electrolyte surface by scraping it off with a zirconia blade (Fig. 5.2E).

Finally, the aligned symmetrical cell was sintered at 1150°C for 1 h. The resulting LNF perovskite layers, with a thickness of approximately 35 μm, formed 3.8 cm^2 WE and CE electrodes, and 0.6 cm^2 reference electrodes (RE) as shown schematically in Fig. 5.1. A total misalignment between both corresponding edges of the WE and CE was measured using an Apex Vision Measuring Machine (Mitutoyo QuickVisionPRO). The misalignment was smaller than 10 μm, which is below 7% of the electrolyte thickness. Hence, such a misalignment is lower than the allowed maximum of 10% of the electrolyte thickness for accurate electrochemical characterization [72].

5.2.2 Electrochemical measurements

In order to investigate the electrochemical behavior of the Cr-free and the Cr-exposed LNF working electrodes in the three-electrode set-up (Fig. 5.3), samples were heated to the operating temperature of 800°C. The heating was performed at a rate of 30°C/h under a flow of dry synthetic air, composed of 20% O_2 (purity 99.6%, <7 ppmv H_2O, where ppmv denotes parts per million in volume) and 80% N_2 (purity 99.999%, <4 ppmv H_2O), at a total flow rate of 500 ml/min for both the WE and the CE sides. After reaching the operating temperature the WE was cathodically polarized under a constant current load of 400 mA/cm^2. Applying such a current load is in line with the standard testing procedure at ECN for a durability test at 800°C. The current was applied using a Pt mesh (Fig. 5.3E).

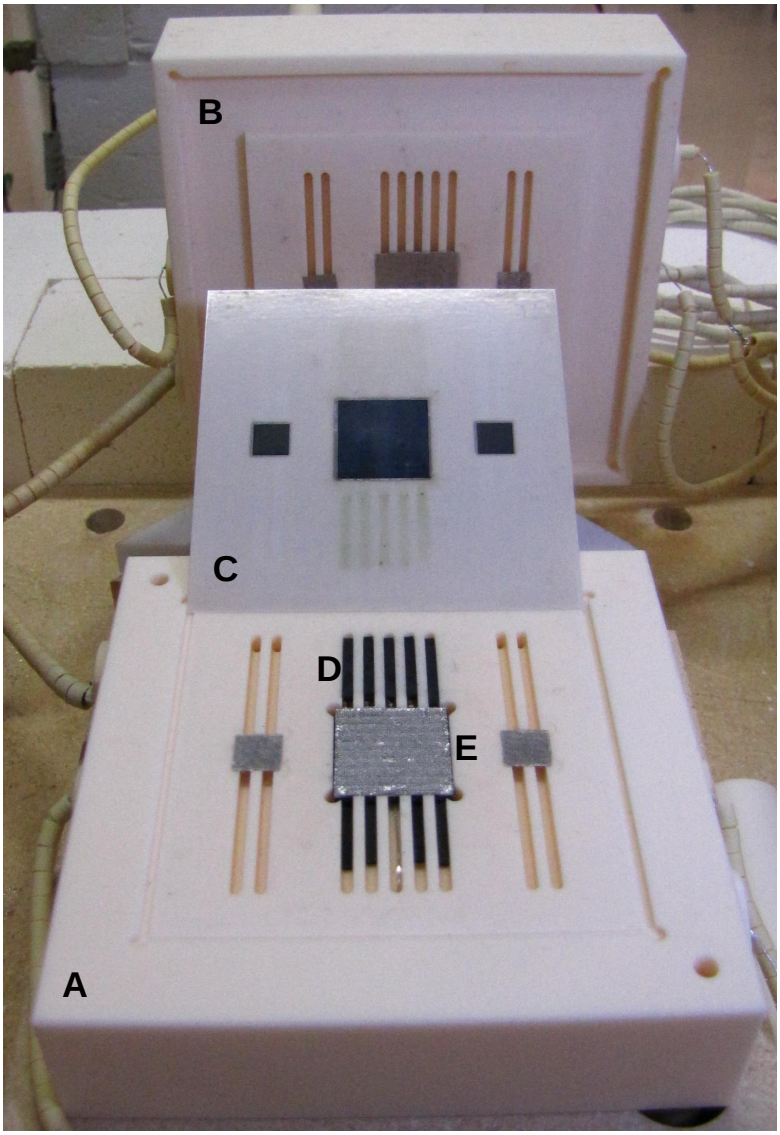

Figure 5.3: Electrochemical measurements were performed in a 'three-electrode set-up': (A) presents the WE ceramic block, (B) shows the CE ceramic block, (C) points to the WE side of the Cr-exposed cell for which the Cr-source (ITM-14) was placed in the gas channels (D). The current was applied using a Pt mesh (E).

A Pt mesh was chosen instead of an Au mesh, which would have been the preferred choice for electrochemical inertness, because of reported reactivity of Au with metallic interconnects. Metallic interconnects were used as the Cr-source during the electrochemical characterization, as described hereafter. The load was interrupted

approximately every 200 h for I-V measurements and impedance analysis at open circuit voltage (OCV), though the discussion of these results is beyond the scope of this paper. Voltage signal between the WE and both reference electrodes RE on both sides of the working electrode was continuously recorded and electrochemical impedance spectroscopy (EIS) was performed under load after periods of circa 200 h uninterrupted operation. EIS measurements were performed with a Solartron 1255 frequency response analyzer in conjunction with a Solartron 1287A electrochemical interface. The applied frequencies ranged from 100 kHz to 0.1 Hz with a signal amplitude of 10 mV.

The voltage signals between the WE and both reference electrodes (RE) were compared and averaged for each measurement point. For the Cr-free reference cell a nearly perfect match between both signals (WE-RE1 and WE-RE2) was observed over the entire operating time, demonstrating the effect of the aimed precision alignment of the WE and CE electrodes. For the Cr-poisoned cell initially an identically perfect match was observed, but an increasing imbalance between both WE-RE signals was observed over time. This is probably due to increasingly inhomogeneous poisoning over the working electrode as described in Section 5.4.1. In order to compensate for the imbalance, both WE-RE signals were averaged to obtain the overall electrochemical performance of the Cr-poisoned cell in terms of overpotential and cell impedance. The averaged voltage signal (WE-RE), representing electrode potential E, was corrected for the ohmic drop between WE and RE in order to present the true cathode overpotential value η. The correction was applied according to the relation: $\eta = E - iR_{ohmic}$, where i represents a current density and R_{ohmic} is the electrolyte contribution obtained from the EIS data under current load (as explained below).

Impedance data was fitted using the Eqcwin software [73–76] with an equivalent circuit of $R(RQ)(RQ)(RQ)$, where Q is a constant phase element and R represents various contributing resistances. Fitting of the EIS data provided values of the contributing resistances to the total resistance, i.e. ohmic (R_{ohmic}) and polarization resistance (R_{pol}).

The Cr-free sample was electrochemically operated in an all-ceramic housing. For the Cr-exposed sample an ITM-14 ferritic FeCr-based alloy in the form of a porous foam (Plansee AG, Reutte, Austria [21, 49]) was used as the Cr source. The laser-cut foam was pre-oxidized for 100 h at 800°C prior to the experiment to insure the presence of a Cr-containing oxide scale on the metal surface. The ITM-14 Cr-source was placed in the gas channels in front of the WE but without any direct contact neither with electrolyte nor with WE (Fig. 5.3D). This allowed the air-flow to pick up volatile Cr species and transport them to the electrochemically operating WE, simulating the Cr evaporation from the stainless steel manifolds, metallic interconnects (MIC) and system components (BoP) of the IT-SOFC stack.

After completing the current load experiments the electrical in-plane conductivity was measured for both the Cr-free and the Cr-exposed working electrodes. For this a standard van der Pauw method was used at the operating temperature of 800°C in air.

5.2.3 Post-mortem analyses

The elemental composition of the Cr-exposed LNF cathode layer was obtained at four different distances from the Cr-source. Therefore, four pieces were laser-cut along the direction of the gas flow (as shown later in 5.7). Subsequently, the CE electrode side was removed for each piece by polishing until YSZ electrolyte was reached and the remaining WE electrode was acid-dissolved and the elemental composition was measured by means of inductively coupled plasma-optical emission spectroscopy (ICP-OES), using a Varian Vista AX PRO CCD.

The surface of the Cr-exposed WE sample was analyzed by field emission scanning electron microscopy, using a JEOL JSM 6330F FEG-SEM equipped with an EDX detector (ThermoNoran's Pioneer NORVAR).

The embedded and polished cross-section of the Cr-exposed WE was analyzed by field emission scanning electron microscopy, using a Philips XL40-W SEM equipped with an Oxford Microspec 600 WDX (wavelength dispersive X-ray) detector and also using SEM-EDX detector.

For the cross-sectional transmission electron microscopy (TEM) study of the LNF/GDC/YSZ assembly of the Cr-exposed WE, a specimen was acquired using focused ion beam (FIB) lift-out sample preparation using a Nova 200 Nanolab SDB (small dual beam). TEM analyses were performed using an FEI Tecnai F30ST equipped with an EDAX energy dispersive X-ray (EDX) detector. All TEM experiments were performed at an acceleration voltage of 300 kV, using several modes of operation: Z-contrast imaging generated by high angle annular dark field (HAADF), general bright field TEM imaging (BF-TEM), energy dispersive X-ray analysis (EDX) in scanning TEM mode (STEM), and high resolution transmission electron microscopy (HRTEM) together with fast Fourier transform (FFT) analysis of the HRTEM images.

5.3 Degradation during operation conditions - Results and Discussion

5.3.1 Overpotential evolution in time

Fig. 5.4 shows the evolution of the WE cathode overpotential η measured versus the RE, and corrected for the ohmic drop between WE and RE, in Cr-free and in Cr-containing atmospheres at 800°C under a load of 400 mA/cm^2. The reference Cr-free LNF cathode showed a stable overpotential over a testing period of 500 h. The LNF cathode exposed to volatile Cr species exhibited a relatively stable overpotential up to 200 h. After that a considerable increase in the overpotential losses was observed over a time period of approximately 200-1000 h.

During the initial 100 h the changes in the overpotential could be attributed to the so-called 'burn-in' process, characteristic for LNF cathodes [77].

For the reference LNF cathode tested in the all-ceramic housing no apparent degradation was observed over the full 500 h of operation. The Cr-containing atmo-

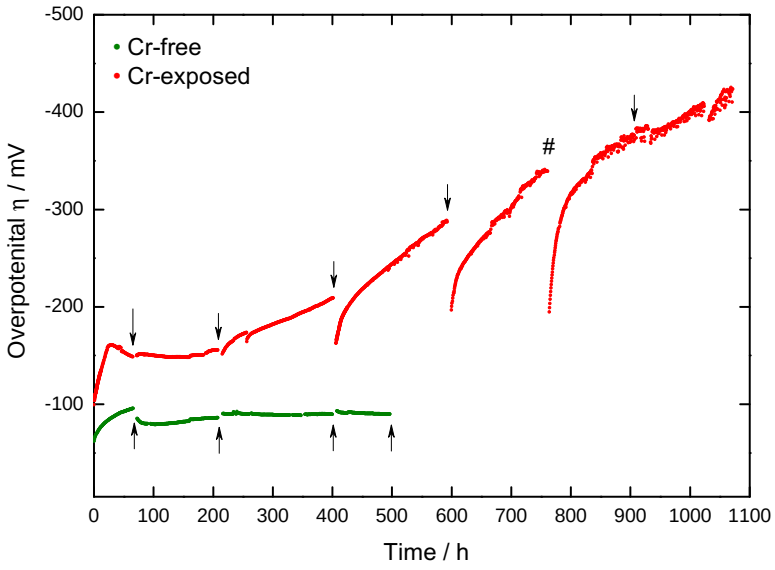

Figure 5.4: Evolution of the cathode overpotential η with time for the LNF WE in Cr-free and in Cr-containing atmospheres. Arrows indicate the EIS measurements under load. A hash sign (#) depicts an accidental current interruption with no EIS measurements performed beforehand.

sphere clearly caused a continuous and progressing degradation of the electrochemical performance of the LNF cathode tested over the period of 1000 h.

While the period of the current interruption had virtually no effect on the overpotential for the Cr-free cathode, a significant effect can be seen for the Cr-exposed cathode, especially after 400 h of operation (Fig. 5.4). After current switch off the WE relaxed to a state with an initially significantly lower overpotential upon switching on the current. Similar transient recovery of the WE performance after a current interruption has been also observed for LSM cathode in the presence of Cr-based interconnect [24, 25].

5.3.2 Evolution of the EIS

As indicated by the arrows in Fig. 5.4 the EIS was performed at the end of each uninterrupted operation period (about every 200 h) in order to follow the change in the electrochemical response of the LNF cathode under current load. Fig. 5.5 presents the EIS evolution with time of the WE, averaged over both RE, measured under a load of 400 mA/cm^2. The reference Cr-free LNF cathode showed a stable and nearly constant impedance (Fig. 5.5A). The LNF cathode exposed to volatile Cr-species exhibited relatively comparable EIS spectra up to 200 h, then a significant increase in size and shift to higher resistance values was observed for the impedance during the time period after 200 h (Fig. 5.5B).

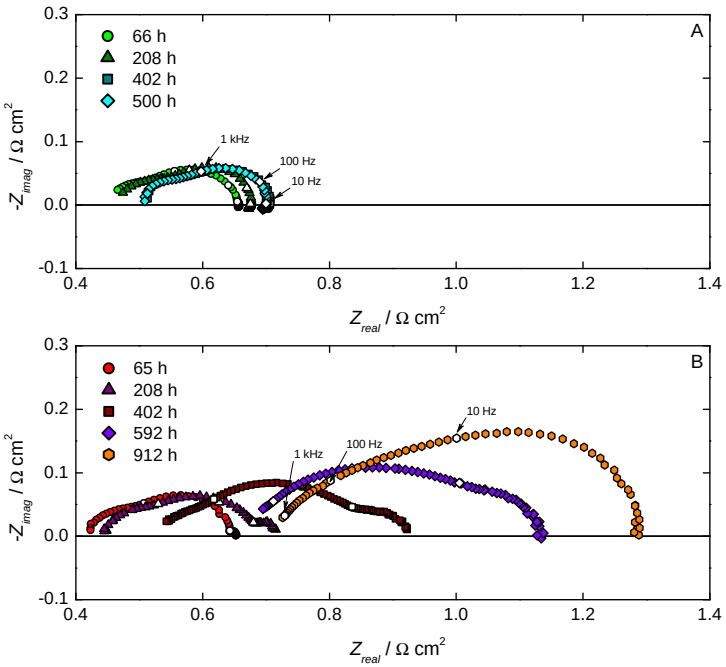

Figure 5.5: Evolution of the WE impedance (EIS) with time, measured under a load of 400 mA/cm^2 in Cr-free (A) and in Cr-containing atmospheres (B).

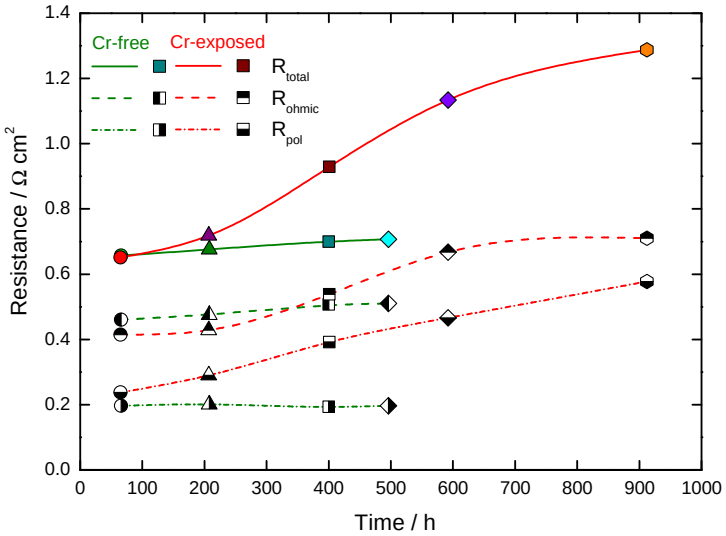

Figure 5.6: Evolution of R_{total}, R_{ohmic} and R_{pol} in time at 400 mA/cm^2 for Cr-free and Cr-exposed sample. Markers shape corresponds to markers in Fig. 5.5.

Evolution of the contributing resistances obtained with EIS

Fig. 5.6 presents the evolution with time of the total (R_{total}), ohmic (R_{ohmic}) and polarization (R_{pol}) resistances of the tested LNF cathodes. The reference Cr-free cathode showed relatively stable values of both R_{ohmic} and R_{pol} resulting in a constant R_{total} during the testing period of 500 h. The LNF cathode exposed to volatile Cr-species exhibited a continuous increase in R_{pol} throughout the experiment. R_{ohmic} was relatively stable up to 200 h, followed by a rather steep increase over the time period of circa 200-600 h, reaching a mild incline between 600 and 1000 h.

The LNF cathode tested in a Cr-free atmosphere showed stable values of both R_{ohmic} and R_{pol}, confirming the intrinsic stability of the LNF cathode under electrochemical operation. However, the LNF cathode tested in combination with a Cr-source showed clear deterioration of both R_{ohmic} and R_{pol} indicating extrinsic degradation due to Cr presence.

5.3.3 In-plane electronic conductivity of Cr-free and Cr-exposed samples

For both Cr-free and Cr-exposed samples, the in-plane electronic conductivity σ was measured at the operating temperature of 800°C in order to determine the impact of volatile Cr-species on the electronic conductivity of the WE. The Cr-free LNF cathode layer showed an in-plane electronic conductivity of 204 S/cm. The Cr-exposed LNF cathode layer exhibited a lower electronic conductivity of 127 S/cm.

The in-plane electronic conductivity of the Cr-exposed LNF layer was lower than the electronic conductivity of the Cr-free layer which is in line with a previous study [63, 64]. An increase in the in-plane resistance of the electrode can cause an apparent increase in R_{ohmic}. However, a drop in the conductivity of 77 S/cm (37%) does not explain the relatively large increase in R_{ohmic}. Other causes for the increase in R_{ohmic} were examined with the post-mortem analyses.

5.4 Post-mortem analyses - Results and Discussion

5.4.1 Overall Cr concentration in the Cr-exposed cathode as a function of the distance from the Cr source

SEM-EDX analyses over the WE surface area (Fig. 5.7) indicates a significant inhomogeneous Cr distribution along the gas flow direction ranging from 3.5 at% to 1.5 at% of Cr.

Fig. 5.8 presents the overall Cr concentration as detected with the ICP-OES method for the Cr-exposed WE operated 1000 h at 800°C under 400 mA/cm^2 load. A preferential higher Cr accumulation was observed at the air inlet close to the Cr source. The Cr concentration decreased nearly linearly as a function of the distance from the Cr source.

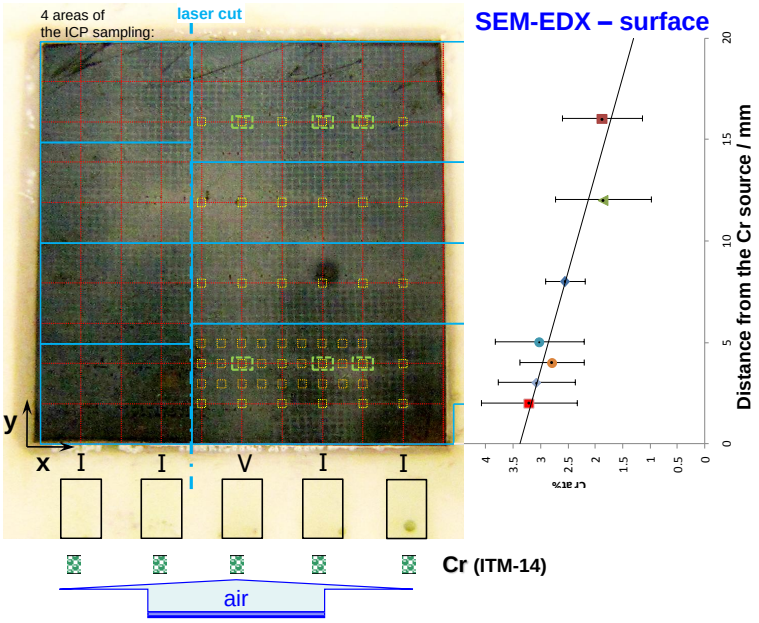

Figure 5.7: The amount of Cr detected with SEM-EDX on the surface of the Cr-exposed WE as a function of the distance from the Cr source. At several distances Y from the Cr-source EDX analyses (orange squares) were performed and averaged to provide the concentration of Cr, which is given as La+Ni+Fe+Cr=100 at%.

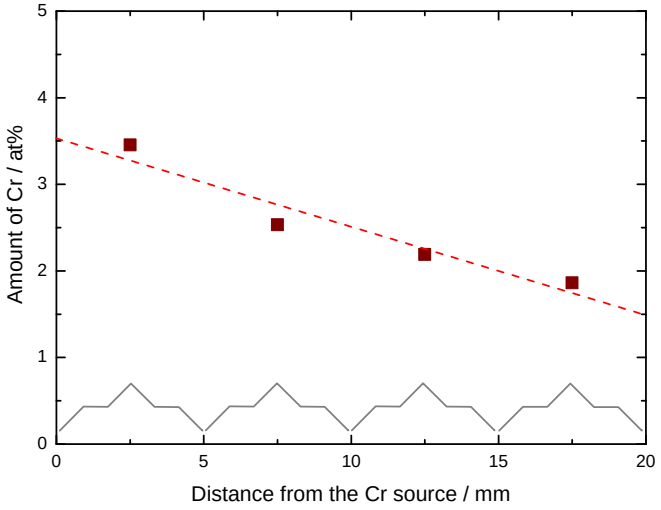

Figure 5.8: The amount of Cr deposited in the Cr-exposed WE as a function of the distance from the Cr source. The concentration is given as La+Ni+Fe+Cr=100 at%. The brackets indicate schematically the regions of the ICP sampling (as shown in Fig. 5.7).

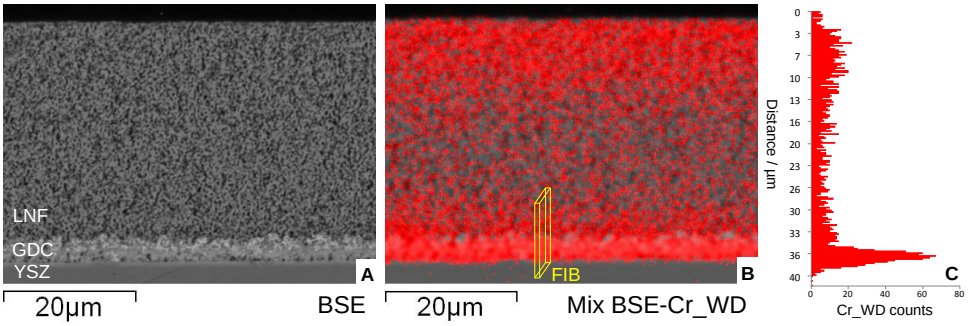

Figure 5.9: Backscattered electron (BSE) SEM image of the embedded and polished WE cross-section taken 2 mm from the Cr source (A). In red (B) an overlay of the Cr elemental mapping on the BSE image. (C) presents a vertical line scan of the Cr counts. A yellow cuboid in (B) indicates schematically a location of the TEM specimen acquired using FIB.

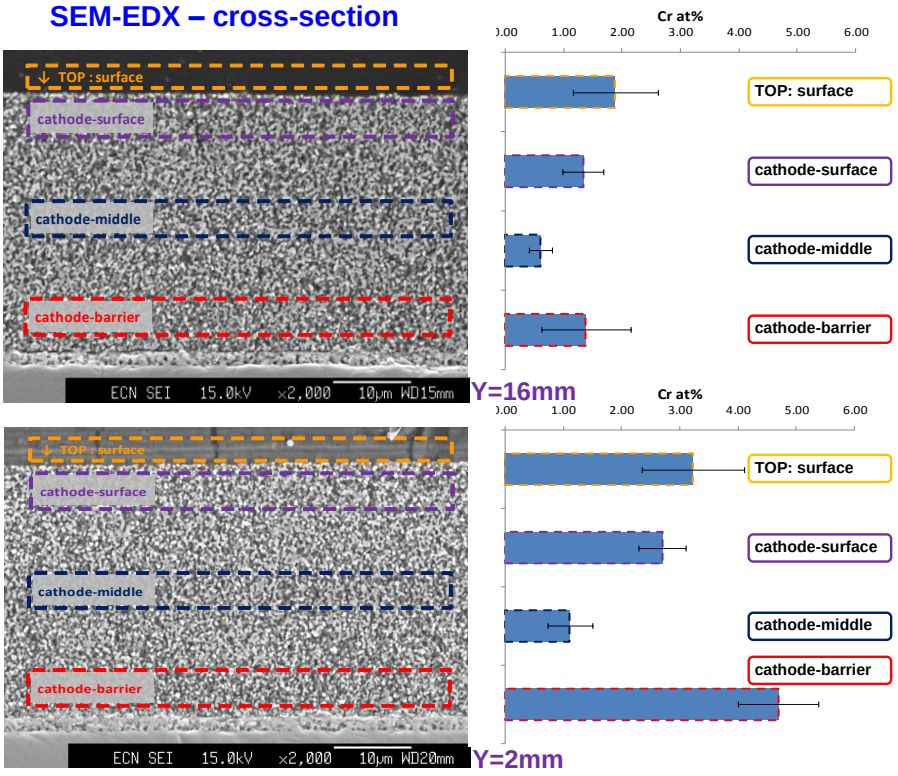

Figure 5.10: The amount of Cr detected with SEM-EDX in the cross-section of the Cr-exposed WE obtained at two distances from the Cr source (2 mm and 16 mm). The concentration is given as La+Ni+Fe+Cr=100 at%.

This observed inhomogeneity would cause an imbalance between the respective WE-RE signals, as clearly has been observed for the Cr-poisoned electrode. For a better description of the overall performance of the electrode the WE-RE1 and WE-RE2 signals (impedance and overpotential) have been averaged.

5.4.2 Cr distribution in the Cr-exposed cathode throughout the layer thickness examined with SEM-WDX/EDX

The overview of the Cr distribution over the depth of the Cr-exposed WE was obtained with wavelength dispersive X-ray spectroscopy (WDX). Fig. 5.9A shows a backscattered electron (BSE) SEM image of the embedded and polished WE cross-section which was cut at 2 mm from the Cr source. An overlay of the Cr elemental mapping on the BSE image (Fig. 5.9B) demonstrates that Cr was not evenly spread throughout the cross-section of the WE. A considerable amount of Cr was accumulated in the region close to the LNF surface, whereas in the middle of the LNF cathode the concentration of Cr was lower. Close to the interface of LNF/GDC the amount of detected Cr was substantial. Cr accumulation within the 2 μm thick GDC layer was exceptionally high. The line profile of the relative Cr concentration throughout the LNF/GDC/YSZ assembly is presented in Fig. 5.9C.

The Cr distribution over the depth of the Cr-exposed LNF cathode was additionaly obtained with SEM-EDX at two distances from the Cr source (2 mm and 16 mm) as shown in Fig. 5.10. The concentration of Cr across the depth of the Cr-exposed LNF cathode decreased as a function of the distance from the Cr source.

The Ni SEM-WDX elemental map (not shown) indicates that Ni was detected everywhere in the LNF layer, as expected on basis of the LNF-composition. However, there were also a number of clearly visible spots with high Ni concentration indicating presence of Ni-rich metal oxide (also shown in Fig. 5.12).

Cr presence in the LNF layer together with Ni-rich precipitates confirms the Cr incorporation into the LNF perovskite as reported in [64] which explains the observed in-plane electronic conductivity decrease. Furthermore, Cr presence at the LNF/GDC interface could be the cause for the increase in R_{pol} as well as in R_{ohmic}. However, there might also be a severe effect of Cr-incorporation in the GDC-layer on R_{pol} and R_{ohmic}. The Cr-incorporation in the GDC-layer is caused by a reaction of Cr-species with the GDC layer, as further explained in Section 5.4.3.

5.4.3 Cr distribution in the Cr-exposed cathode at the interface of LNF/GDC/YSZ examined with STEM-EDX

The origin of the TEM specimen is schematically shown by the yellow cuboid in Fig. 5.9B. The specimen was cut out by means of FIB lift-out sample preparation and is presented in Fig. 5.11A. The STEM/HAADF image of Fig. 5.11B shows the investigated areas of the LNF/GDC/YSZ assembly after the final thinning step down to electron transparency. In Fig. 5.11B area 0 indicates the region of the STEM-EDX elemental mapping. Within the indicated rectangular areas 1, 3 and 4 in Fig. 5.11B

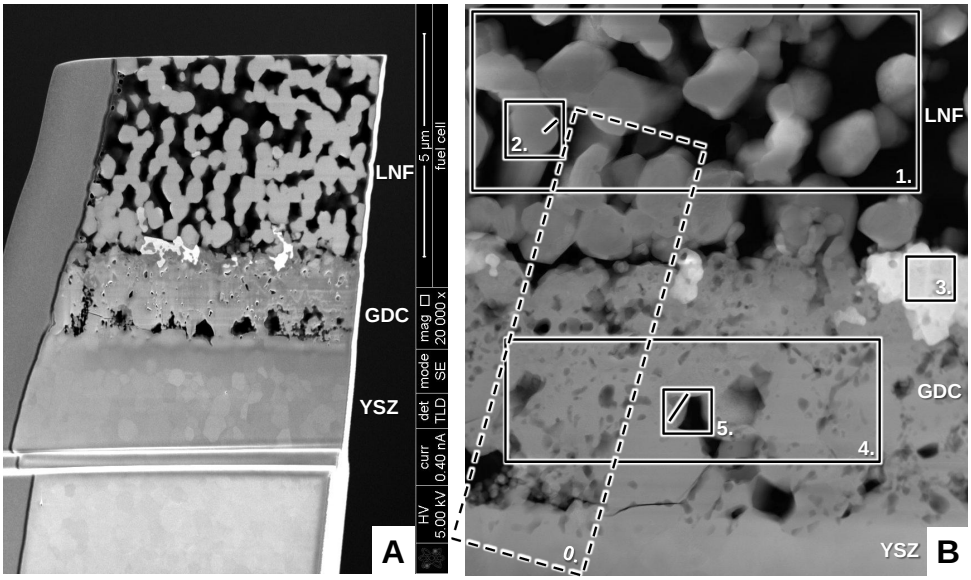

Figure 5.11: FIB prepared TEM-specimen before the final thinning step (A) and STEM/HAADF image (B) indicating the investigated areas of interest across the LNF/GDC/YSZ assembly. Area 0 indicates the region of STEM-EDX mapping. Within areas 1, 3 and 4 STEM-EDX elemental analyses were conducted. In areas 2 and 5 STEM-EDX line scans were performed.

the STEM-EDX elemental analyses were conducted. In areas 2 and 5 the STEM-EDX line scan was performed.

Fig. 5.12 presents the STEM-EDX mapping of the LNF/GDC/YSZ interface recorded over area 0 as indicated in Fig. 5.11B. The La, Ni and Fe maps show the region of the LNF grains. The Ni map shows additionally a Ni-rich precipitate (most likely NiO) located between LNF grains. The Cr map revealed that Cr was incorporated into the periphery of the LNF particles. Cr-enrichment is clearly indicated by high Cr counts and coincides with Ni-poor concentrations at the edges of the LNF grains. Furthermore, the Cr map demonstrates overall high Cr concentration within the GDC layer with locally even higher Cr intensities. Regions of a very high Cr concentration within the GDC layer overlap with Ce-poor and Gd-rich areas.

In Fig. 5.12 only raw count maps are presented, as the number of counts per pixel was too low to allow accurate quantification. Hence, further analysis by STEM-EDX was performed as indicated in Fig. 5.11B.

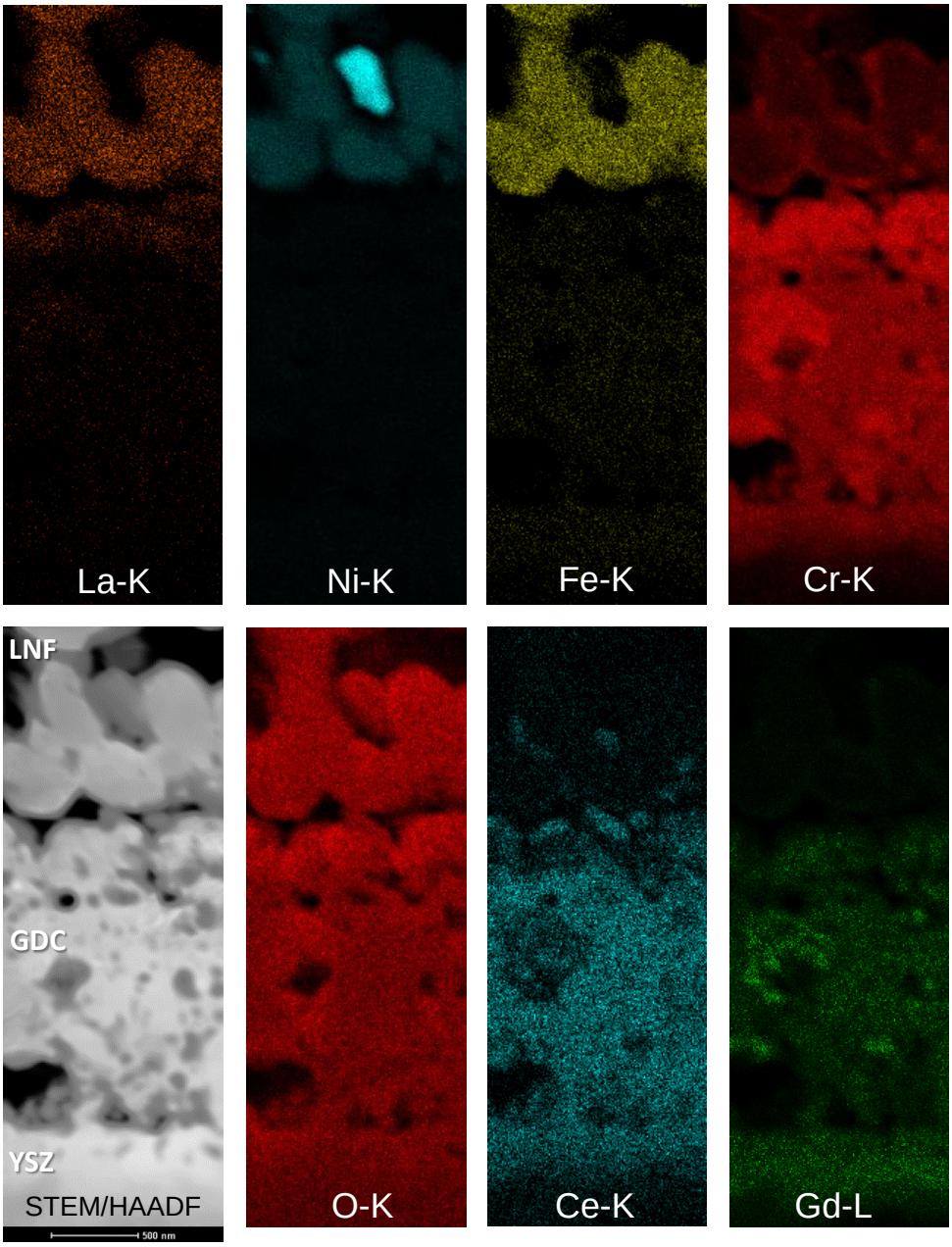

Figure 5.12: STEM-EDX mapping of the LNF/GDC/YSZ interface presented on HAADF image. Raw count maps of La, Ni, Fe, Cr, O, Ce and Gd are shown over the 1.27 µm × 3.48 µm region (area 0 indicated in Fig. 5.11).

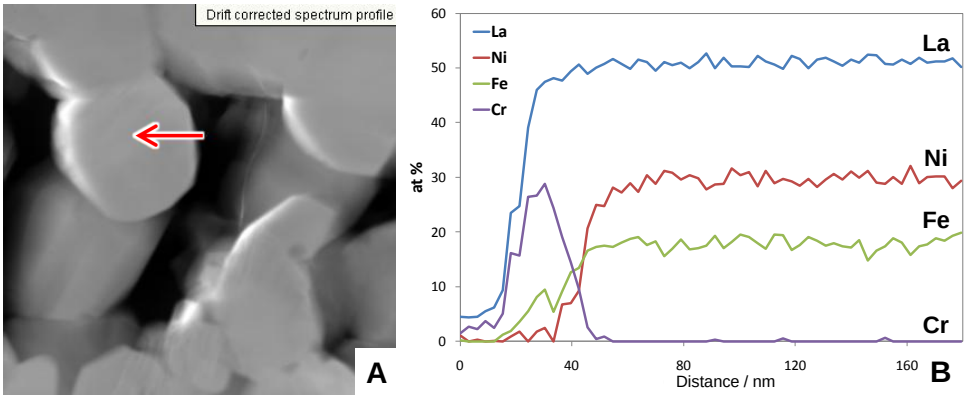

Figure 5.13: HAADF image of the investigated LNF grain (A). The red arrow indicates position and direction of the STEM-EDX line scan which was performed at 60 equidistant points along the 180 nm long line. (B) shows the compositional profile (in atomic%) across the LNF grain. Close to the edge of the grain also the signal of carbon (originating from the epoxy) was taken into at% calculations.

Cr distribution within the LNF layer

The STEM-EDX area scans within the LNF layer, indicated as area 1 in Fig. 5.11B, provided the following average elemental composition: 50.5 at% of La, 29.2 at% of Ni, 17.3 at% of Fe and 3.0 at% of Cr. This result confirms Cr accumulation of 3 at% in the LNF layer close to the interface with GDC layer.

Fig. 5.13 presents the location of the STEM-EDX line scan across the LNF grain (performed in the area 2 in Fig. 5.11B). The compositional profile (in atomic %) across the LNF grain indicated significant Cr enrichment in the outer shell of the LNF grain accompanied with a very low concentration of Ni together with lowered concentration of Fe. The Cr affected depth of the LNF grain was estimated to be up to 30-40 nm. Such Cr penetration depth is in agreement with a TEM-EDX study, as described in an earlier paper by the authors [64]. In the middle of the grain the nominal LNF perovskite composition was preserved: La 50 at%, Ni 30 at%, Fe 20 at%, as expected for $LaNi_{0.6}Fe_{0.4}O_3$.

Cr incorporation and Ni removal from the LNF perovskite justifies the decrease of the in-plane electronic conductivity as Cr-rich perovskite has lower electronic conductivity than Ni-rich [42]. The change in surface composition of the LNF-particles, especially close to the interface with the GDC-layer might be responsible for the increase in R_{pol}, as the cathode surface is known to play a significant role in the electrochemical process of oxygen reduction reaction (ORR) [78–80].

Cr distribution within the GDC layer

The STEM-EDX area scans within the GDC layer, indicated as area 4 in Fig. 5.11B, provided the following average composition: 47.1 at% of Ce, 31.5 at% of Gd and 21.4 at% of Cr. The atomic ratio of Ce and Gd was 3:2 as in the nominal

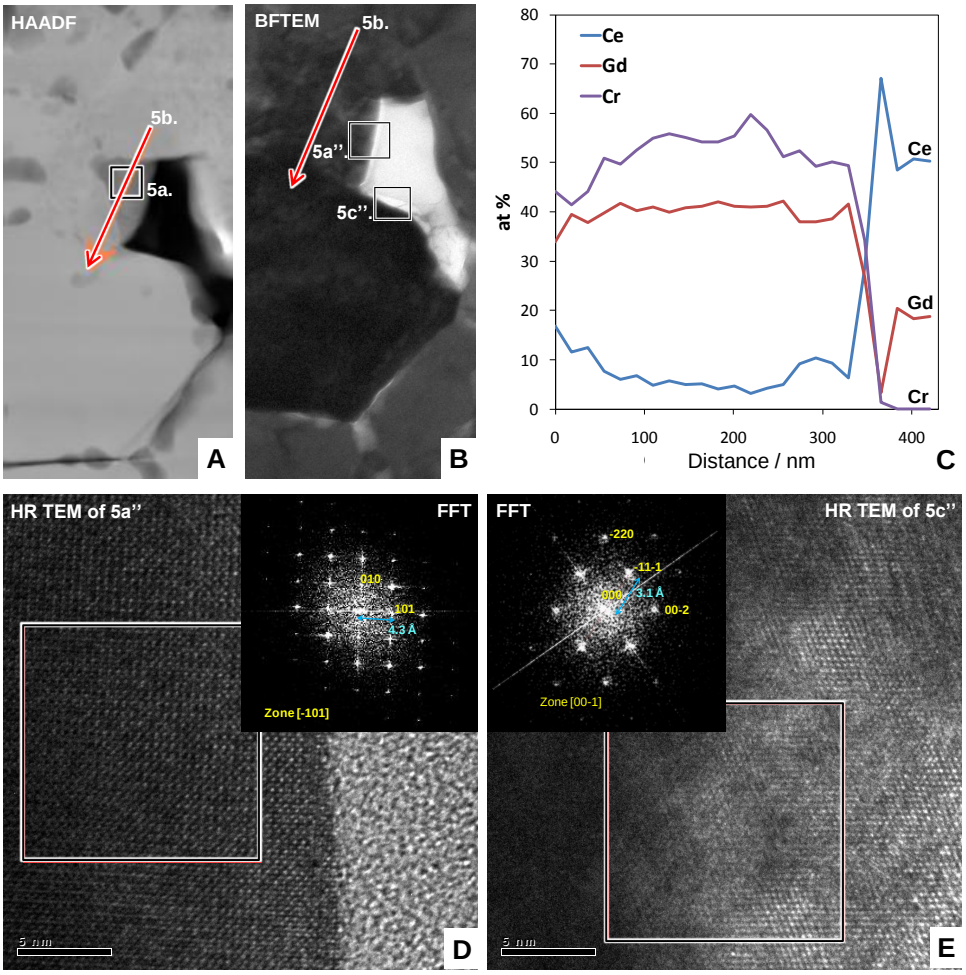

Figure 5.14: HAADF (A) and BF-TEM image (B) of the Cr-GDC grains. A red arrow indicates the position and direction of the STEM-EDX line scan of 420 nm with EDX taken every 17.5 nm. (C) shows resulting at % compositional profile. (D) and (E) presents HRTEM images of the positions in (B) with a corresponding FFT (as the insets).

$Ce_{0.6}Gd_{0.4}O_{1.8}$. This finding revealed remarkably high Cr accumulation of more than 20 at% in the GDC layer. An important fact is that such Cr-enrichment of GDC layer was not at all observed in the previous Cr-poisoning experiment [64], which was operated under conditions without current load, i.e. are comparable to OCV (Chapter 3 of this thesis).

The STEM-EDX line scan was carried out as indicated in Fig. 5.14A and 5.14B by line 5b. The compositional profile (in atomic %) across the investigated grains (Fig. 5.14C) shows Cr-Gd-rich grain across 300 nm distance and shift to a Ce-Gd-rich

grain at the end of the scan.

Fig. 5.14A shows the location of the STEM-EDX area scans (area 5a in the middle of line 5b) performed on a distinctively different grain compared to a majority of GDC grains. The average composition obtained in the area 5a was: 4.9 at% of Ce, 43.5 at% of Gd and 51.6 at% of Cr. Such composition suggested the presence of $GdCrO_3$ perovskite.

In order to investigate the crystal structure of a Cr-Gd-rich grain, in comparison with GDC grain, a HRTEM study was conducted in two regions as indicated in Fig. 5.14B.

The HRTEM image recorded on the edge of Cr-Gd-rich grain in the area 5a" is shown in Fig. 5.14D. The fast Fourier transform (FFT) of the crystalline region (inset in Fig. 5.14D) revealed an electron diffraction pattern that could be indexed as belonging to an orthorhombic perovskite cell with the parameters: a_o = 5.3 Å, b_o = 5.5 Å, c_o = 7.6 Å, very close to the cell parameters of $GdCrO_3$ perovskite (ICDD 71-1275). The atomic composition obtained with STEM-EDX in area 5a may, therefore, be presented as $(Gd_{0.9}Ce_{0.1})CrO_3$.

The HRTEM image recorded on the edge of Ce and Gd rich grain in the area 5c" is shown in Fig. 5.14E. The FFT of the crystalline region (inset in Fig. 5.14E) showed an electron diffraction pattern that could be indexed as belonging to a cubic fluorite cell with an ao parameter of 5.4 Å, similarly to the cell parameters of $Gd_{0.30}Ce_{0.70}O_{1.85}$ fluorite (ICDD 75-0163). The atomic composition obtained with STEM-EDX in the end region of the line scan (Fig. 5.14C) may be thus presented as $Ce_{0.7}Gd_{0.3}O_x$.

STEM-EDX and HRTEM study of the Cr-exposed GDC layer revealed the presence of perovskite type Gd-Cr-rich grains located next to Ce-enriched fluorite GDC grains. Such impact of Cr on the GDC-layer phase composition has serious implications for the ionic conductivity of GDC layer and can therefore justify the observed increase in R_{ohmic} of the WE.

Pt deposits

The STEM-EDX area scans at the interface of LNF/GDC layer, indicated as area 3 in Fig. 5.11B, revealed the presence of a nearly pure Pt deposit. This finding suggests possible Pt evaporation from the Pt mesh after prolonged operation. In the reference sample (Cr-free 500 h at 800°C under 400 mA/cm^2) the presence of Pt deposits was also detected (not shown here).

5.5 Mechanism of Cr-poisoning - Discussion

The LNF cathode tested in a Cr-free atmosphere showed no apparent degradation with stable values of both R_{ohmic} and R_{pol}, confirming the intrinsic electrochemical stability of the LNF cathode under operating conditions.

However, the LNF cathode tested in combination with the Cr-source showed clear deterioration of both R_{ohmic} and R_{pol}, indicating extrinsic degradation due to volatile Cr-species, which penetrated the working electrode (WE) and affected both the LNF cathode layer and the GDC barrier layer.

The top of the LNF cathode is assumed to be electrochemically inactive, serving just as a current collector. The presence of Cr in the top layer indicates that a chemical reaction of volatile Cr-species took place in this part of the LNF perovskite layer, which is in accordance with the Cr exposure study at open circuit voltage (OCV) [64] (Chapter 3 of this thesis). The observed loss of the in-plane electronic conductivity of the LNF layer, which was due to Cr-incorporation, contributed only partly to the increase in R_{ohmic}. The middle part of the LNF layer was less affected by Cr, showing a relatively 'low-Cr-accumulation zone'. This is not in accordance with the findings under OCV conditions [64], where the Cr-distribution was uniform over the whole LNF-layer thickness. The lower Cr-content in the middle part of the LNF layer is most likely a consequence of the electrochemical driving force for Cr accumulation towards the LNF/GDC interface. This is clearly demonstrated by high Cr concentration detected within a few microns of the LNF/GDC interface. In this region the electrochemically-driven reaction is assumed to play an even greater role than the chemical reaction. The more reducing conditions at the LNF/GDC interface [15, 80] is very likely to reduce gaseous Cr^{VI}-species [10, 22] to Cr^{III} which directly exchange with Ni in the LNF lattice. Such a change in the surface composition of the LNF-particles, into La-Cr-rich perovskite, might be responsible for the deterioration of the electrochemical activity for the oxygen reduction reaction (ORR) and thus contributing to the increase of R_{pol}. Cr incorporation into the LNF grains, up to tens of nm, was accompanied by a segregation of NiO-precipitates throughout the LNF layer thickness in accordance with a previous study at OCV [64] (Chapter 3).

A massive Cr deposition of more than 20 at% was observed within the 2 μm thick GDC layer. Cr reacted with Gd to form a $GdCrO_3$ perovskite. The $GdCrO_3$ layer might impede transport of oxygen ions from triple phase boundaries (TPB) to YSZ electrolyte, as this perovskite has significantly lower ionic conductivity compared to fluorite GDC [81, 82]. In the periphery of the GDC grains, the detected composition of $Ce_{0.7}Gd_{0.3}O_x$ might exhibit locally higher ionic conductivity compared to nominal $Ce_{0.6}Gd_{0.4}O_{1.8}$ [81]. Such a local improvement of ionic conductivity would be negligible considering the fact that GDC grains were covered and surrounded by the poorly conducting $GdCrO_3$ particles. Cr deposition within the GDC layer, taking place under current loading, is in clear contrast with the absence of Cr deposition observed within the GDC layer during OCV test [64] (Chapter 3). Under the electrochemical operation the local oxygen partial pressure (PO_2) within GDC layer is estimated to be in the range of 10^{-8}–10^{-10} atm. Lower partial pressure of oxygen combined with electrochemically enhanced reaction might explain the observed massive Cr deposition within GDC layer. Concluding, it seems that the blocking effect for the ionic transport caused by Cr-rich particles within GDC layer contributed to the increase of R_{ohmic}.

To the best knowledge of the authors, the present study reports, for the first time in the literature, that Cr-poisoning affected not only the cathode material (LNF) but also the barrier layer (GDC).

The electrochemical reaction mechanism for the reduction of oxygen by the LNF cathode is probably restricted mainly to the TPB region (similarly to LSM). This is suggested by the (minor) deposition of Pt at the interfaces and a very low bulk ionic

conductivity of LNF [32, 83, 84]. Therefore, the oxygen reduction reaction (ORR) is localized and restricted to the TPB, unlike for the LSCF cathode (which is a MIEC cathode, hence its comparatively high bulk ionic conductivity broadens the ORR region [85, 86]). An ORR region severely limited to the TPB will most likely cause a steep gradient in PO_2 near or at the LNF/GDC interface (local drop in PO_2) which could enhance Cr deposition and subsequent reaction with GDC. This is in clear contrast with measurements at OCV [64], where no reaction of Cr-species with GDC was observed. The larger Cr-deposition in the doped ceria layer, compared with the LNF cathode layer, suggests indeed that the electrode reaction model is restricted to the TPB and that volatile Cr-species can easily reach the TPB area, similar to what has been observed for the LSM cathodes [12].

The different chemical nature of LNF, compared to LSM or LSCF, in terms of the absence of the Cr-nucleating-agents [5] (like Mn^{2+} and/or SrO [12, 13, 15]) results in different Cr-poisoning behavior. The main characteristic feature of LNF as cathode material is that it does not contain Sr, hence no formation of $SrCrO_4$ occurs, which has been reported frequently for the Cr-poisoning of LSCF cathodes [13, 15]. It seems therefore that the lower LNF-reactivity with Cr-species allows the Cr-containing vapors to reach to the TPB and react further with the GDC barrier layer. Cr reactivity with the GDC layer has not been previously reported for GDC/LSCF cathodes.

The present study should be regarded as an accelerated Cr-poisoning test (owing to a porous Fe-Cr interconnect foam with a high Cr-release rate) allowing for the insight into the Cr-poisoning mechanism after relatively short testing period. However, a comparative study, in practical and reproducible IT-SOFC stack conditions, with other SOFC cathodes is needed to provide a realistic Cr-tolerance evaluation.

A composite LNF:GDC interlayer (with low Gd content) might be an interesting research direction to increase and spread the TBP region thus avoiding a localized high overpotential zone (with locally very low PO_2) hence possibly significantly reducing Cr-poisoning impact on the Sr- and Mn-free LNF cathode material.

5.6 Conclusions

The absence of degradation for the $LaNi_{0.6}Fe_{0.4}O_3$ (LNF) cathode, when tested in Cr-free atmospheres, confirmed the intrinsic electrochemical stability of LNF. However, extrinsic degradation, due to volatile Cr-species, caused LNF cathode performance loss.

Based on the presented observations the following mechanism has been derived for Cr-poisoning of $LaNi_{0.6}Fe_{0.4}O_3$ cathodes under current load:

(1) Overpotential and impedance increase was due to reaction of volatile Cr-species with both LNF grains and the GDC barrier layer.

(2) R_{ohmic} increase was caused by a decrease of the in-plane electronic conductivity of the LNF layer, due to Cr incorporation and Ni removal from LNF, and a

deterioration of the ionic conductivity of the GDC layer, due to formation of a $GdCrO_3$ phase.

(3) R_{pol} increase was caused by a decrease of electrochemical activity of the LNF surface towards oxygen reduction reaction at the TPB, due to Cr presence in the outer shell of the LNF grains.

(4) Chemical reaction and electrochemically-driven reaction of volatile Cr-species with LNF and GDC contributed to degradation of LNF cathodes under current load.

Acknowledgements

This work was partly supported by the European Commission, as part of the European Project SOFC600 (SES6-CT-2006-020089), and partly supported by funding from ECN. Wim Haije and Paul Cobden are thanked for discussions and comments. Sebastian Molin is acknowledged for performing the van der Pauw measurements and useful discussions. ECN Engineering & Services (Materials Testing & Consultancy group) is thanked for the SEM and ICP-OES analysis. ECN Engineering & Services (MT & C and Realisation) is acknowledged for development of the laser trimming process and various laser cutting assistance. Philips Innovation Services (MiPlaza) is acknowledged for materials analysis. Especially, Carlo Manders is thanked for the SEM-WDX measurements and Marcel Verheijen is gratefully acknowledged for the STEM analyses.

6 Applicability of the LNF material in IT-SOFC systems

6.1 Introduction

Due to its favorable properties, LNF can be used for various features of IT-SOFC systems. The beneficial properties of LNF include: high electronic conductivity, matched thermal expansion coefficient, and good structure stability [32]. Furthermore, claimed high Cr-resistance of LNF [11, 14, 16] enables its use in the IT-SOFC stacks, where relatively cost-effective interconnect materials such as chromia-forming ferritic stainless steels are used. The potential foreseen applicability of LNF perovskite ($LaNi_{0.6}Fe_{0.4}O_3$) in an IT-SOFC stack, is shown in Fig. 6.1, and describes the following possible features:

- current collecting layer
- interconnect protective coating
- electrochemically active cathode layer.

All these potential LNF applications require a thorough understanding of the interaction between LNF and Cr-species that originate from the Fe-Cr metallic interconnect. The generally assumed Cr-tolerance of the LNF material is quite debatable considering the findings presented in Chapters 2-5.

The knowledge gained and described in Chapters 2-4, allows recommendations to be made for a feasible non-electrochemical application of LNF. The recommendations include a proper tailoring of the LNF properties and operating conditions for using LNF as a current collecting layer, as discussed in Section 2, and as an interconnect protective coating, as discussed in Section 3.

In order to make recommendations for the use of LNF as an electrochemically active cathode layer further experiments were necessary. In Chapter 5 it was revealed that it is not only the impact of Cr-species on the LNF-cathode that may negatively influence the electrochemical performance, but also the reactivity of Cr-species with

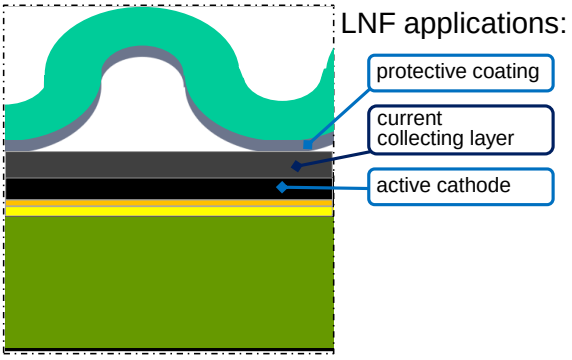

Figure 6.1: Possible applications of LNF material in an IT-SOFC stack (as shown in Fig. 1.4).

the underlying GDC barrier layer [87]. Section 4 below provides further discussion, offering suggestions for reliable operation of an LNF cathode under realistic IT-SOFC stack conditions.

Recommendations for the application of LNF material in IT-SOFC systems will be presented as a function of LNF microstructure (especially grain size), operating temperature, and concentration of Cr-species in the cathode gaseous environment. These parameters have been explored in the determination of the extent of Cr-tolerance of the LNF material, as discussed in the previous chapters. An optimum must be found in these parameters to enable successful implementation of the LNF material in IT-SOFC systems.

6.2 Applicability of the LNF material as a current collecting layer

A current collecting layer should posses good electronic conductivity that minimizes the in-plane resistance losses [2–4, 6]. LNF as a current collecting layer exhibits very high electronic conductivity (Chapter 3, Section 3.3.2), and also shows long-term phase stability at the operating temperatures (Chapter 2, Section 2.3.1). However, for the use of LNF in a Cr-containing environment of a cathode compartment in an IT-SOFC stack, further requirements must be met. Figure 6.2 presents schematically the recommendations for the optimization of the operating conditions and the LNF microstructure. Following such recommendations would allow the use of LNF as a current collecting layer when the combination with an Fe-Cr interconnect is required. The optimizations are listed below:

(*i*) *Operating temperature should be lower than 800° C, preferably about 600° C.*

The detrimental impact of Cr-species, on the crystal structure (Chapter 2) and

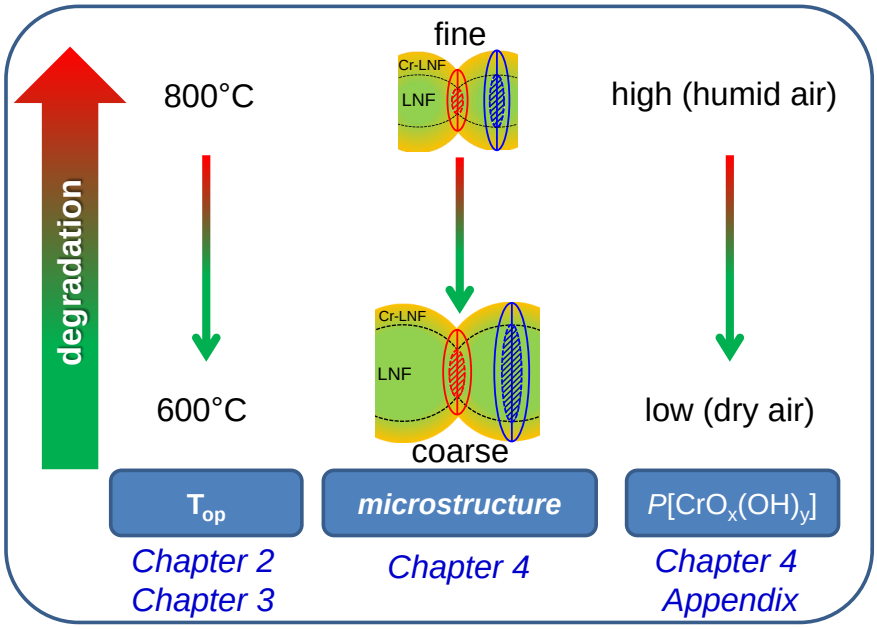

Figure 6.2: Recommendations for the LNF microstructure properties and operating conditions (temperature and concentration of volatile Cr-species) for the non-electrochemical applications of the LNF material (i.e. current collecting layer and/or interconnect protective coating).

the electronic conductivity (Chapter 3) of LNF, was significantly smaller at 600°C compared to 800°C.

(*ii*) *Gas atmosphere should be dry and gas should be provided at high velocities.*

Only dry air should be provided to the cathode compartment of the IT-SOFC stack, as humid air significantly accelerated Cr-poisoning (Chapter 4 Appendix). The velocity of the gas flow should be increased, which would lower the residence time of Cr-species above the LNF-cathode and therefore hinder the Cr-incorporation into LNF. Higher gas flows might reduce the local concentration of Cr-species above the ferritic steel. Hence, a high cathode flow is preferred as long as the operating limits of the system, with respect to cooling and system efficiency, are fulfilled. Stagnant air conditions are highly undesirable (e.g. during the thermal cycling) as the Cr-background pressure increases. Hence continuous air flow is recommended.

(*iii*) *LNF microstructure should be coarse.*

The LNF microstructure with coarse particles (large grains with thick necks) and low porosity showed the smallest increase of the in-plane resistance and the lowest

Cr accumulation, when exposed to Cr-poisoning conditions under OCV (Chapter 4). For these reasons, a coarse LNF microstructure is recommended for the non-electrochemical application of LNF as a current collecting layer.

6.3 Applicability of the LNF material as an interconnect protective coating

Additional requirements are needed in order to use LNF as an interconnect protective coating, next to fulfilling the proposed recommendations for the LNF application as the current collecting layer (Section 2).

The aim of using an interconnect protective coating is to prevent evaporation of Cr-species from the Fe-Cr interconnect. At the same time protective coating should maintain low contact resistance between the interconnect and the current collecting layer. For this purpose the LNF protective coating should be made dense and sufficiently thick. The thickness of the dense LNF layer should be properly chosen. The adjustment should allow a certain layer thickness to become a reaction zone of LNF with the Cr-oxide scale growing on the ferritic steel surface.

The reaction products between the ferritic steel and the LNF protective coating (Chapter 2) exhibit sufficiently high electronic conductivity [4, 6, 42] hence not increasing considerably the contact resistance. The reaction products comprise a LaCr-rich perovskite (with general composition $La(Cr,Ni,Fe)O_3$) and a spinel (generally described as $(Ni,Fe)(Fe,Cr)_2O_4$). N.B. $LaCrO_3$ was used as a HT interconnect material in Generation 1 of SOFCs (Fig. 1.3) due its conductivity and stability. Taking into account high electronic conductivity of reaction products, such a reaction layer does not contribute significantly to the increase of resistance losses. Hence this layer maintains low contact resistance with low degradation. Last but not least, the reaction zone bonds Cr in the La-chromite. Consequently, further outward diffusion of Cr towards the cathode compartment of the IT-SOFC stack is inhibited.

When feasible the operating temperature should be lowered towards 600°C (as recommended for the LNF application as a current collecting layer). It has been shown in Chapter 2 that the solid-state reactivity within the reaction zone of adjacent LNF and Cr-containing interconnect is kinetically hindered at lower temperatures.

6.4 Applicability of the LNF material as an electrochemically active SOFC cathode

Chapter 5 provided explanation of the Cr-poisoning mechanism taking place under current load in the accelerated Cr-poisoning conditions. It was established that volatile Cr-species, originating from the Fe-Cr interconnect, cause electrochemical performance degradation of LNF cathodes under current load conditions at 800°C. The performance loss, observed as an increase of the cathode overpotential and cell impedance, is due to reaction of Cr-species with both LNF-cathode and GDC barrier layer.

It seems, therefore, that a Cr-tolerant cathode might not be sufficient to assure the absence of Cr-poisoning of the SOFC because the reactivity of Cr-species with the underlying GDC barrier layer could be of greater significance.

With the help of in-situ EIS measurements it was not possible to distinguish between the contribution of the Cr-poisoned LNF and of the GDC-layer on the performance degradation. It was also not possible to establish the exact influence of Cr incorporation into the LNF grains at the TPB and the role of Cr-reaction with GDC. Concerning the Cr-reaction with LNF a question to be answered is whether Cr-incorporation into LNF surface has effect on R_{pol}? With respect to Cr-reaction with GDC the following open questions remain: Was only R_{ohmic} affected or R_{pol} as well? What would be a percentage contribution of Cr-poisoned GDC to the overall performance loss?

Another question that should be addressed is the exact influence of the overpotential on the Cr-poisoning process. Is there any upper limit for the cathode overpotential below which no reaction with GDC would occur? The absence of Cr-reaction with GDC observed at OCV suggests that it was the overpotential, thus lower PO_2 at TPB, that triggered the Cr-reactivity with GDC.

6.4.1 Suggestions for a possible Cr-tolerance improvement of LNF cathode

In order to avoid very low PO_2 at the TPB, which might trigger the Cr-reactivity with GDC, the cathode overpotential should not be high. An LNF cathode with a good initial electrochemical performance, hence a low overpotential, might be achieved by implementing a very fine microstructure of the LNF active cathode layer. This would increase the amount of TPB assuring a low overpotential.

A step further would be to design a double layer cathode structure. It should comprise a fine composite LNF:doped-ceria interlayer and a coarse LNF current collecting layer. A composite interlayer of LNF:doped-ceria might be an interesting research direction for increasing and spreading the TBP region, thus avoiding a localized high overpotential zone (with locally very low PO_2). The dopant of ceria should preferably make the ceria more robust against Cr-reactivity within a larger overpotential range. This would prevent a rapid reaction of Cr-species with doped-ceria barrier layer and doped-ceria in the composite layer. A coarse LNF current collecting layer on top of LNF:doped-ceria interlayer would provide lowest increase of the in-plane resistance and lowest Cr-accumulation, upon exposure to Cr-species. This would assure efficient electrons supply for the oxygen reduction process spread over the electrochemically active TPB sites in the LNF:doped-ceria interlayer.

Similarly, as recommended in Section 2, the gas atmosphere should be dry and gas should be provided at high velocities, as long as the operating limits of the system are fulfilled.

6.4.2 Outlook on further research

Further investigation should be devoted to the special role of the GDC barrier layer in the Cr-poisoning process. Especially the relation between the Gd/Ce ratio and the reaction rate of Cr with the GDC layer under various overpotentials is of importance.

The research on the type and the concentration of a ceria dopant is also highly recommended. It is especially desirable in the view of a possible Cr-poisoning suppression by using a composite LNF:doped-ceria interlayer implemented in the double layer LNF cathode concept (Section 4.1).

The benefits of reduced operation temperature for the non-electrochemical LNF applications, as presented in Section 2 and 3, are not at all straightforward in the case of electrochemical LNF application. Lowering operating temperature below 800°C would mean deterioration of the electrochemical activity of the LNF cathode causing overpotential increase (when maintaining the same load). This would lead to enhanced Cr reactivity due to reduced PO_2. A concept of a double layer cathode structure (Section 4.2) could provide an acceptable electrochemical performance at reduced temperatures below 800°C. This would possibly result in a negligible Cr-poisoning impact on such a double layer LNF cathode.

6.5 Conclusions

Cr-poisoning may not be fully avoidable in the IT-SOFC systems, where chromia-forming ferritic stainless steels are used as interconnects. However, a synergetic approach may be undertaken in order to reduce the Cr-poisoning impact:

➪ **minimize the presence of volatile Cr-species:**

- interconnect protective coatings
- dry air at high flow velocities

➪ **adjust the LNF microstructure according to the application:**

- coarse microstructure for non-electrochemical use
- fine microstructure for electrochemically active cathode layer

➪ **seek for a more Cr-tolerant cathode/barrier layer combination:**

- concept of a double layer LNF cathode structure.

Bibliography

[1] BBC. *Population seven billion: UN sets out challenges* (2011-10-26).

[2] L. Carrette, K. Friedrich and U. Stimming. *Fuel Cells Fundamentals and Applications.* FUEL CELLS, **1**, 1 (2001).

[3] J. Larminie and A. Dicks. *Fuel Cell System Explained.* Wiley press (2003).

[4] W. E. Vielstich, A. E. Lamm and H. A. E. Gasteiger. *Handbook of Fuel Cells: Fundamentals, Technology, Applications.* Wiley press (2003).

[5] F. de Bruijn. *The current status of fuel cell technology for mobile and stationary applications.* Green Chemistry, **7**, 132–150 (2005).

[6] S. Singhal and K. Kendall. *High-temperature Solid Oxide Fuel Cells: Fundamentals, Design and Applications.* ELSEVIER (2003).

[7] O. Yamamoto. *Solid oxide fuel cells: fundamental aspects and prospects.* Electrochimica Acta, **45**, 2423–2435 (2000).

[8] T. Araki, T. Ohba, S. Takezawa, K. Onda and O. Y. Sakaki. *Cycle analysis of planar SOFC power generation with serial connection of low and high temperature SOFCs.* Journal of Power Sources, **158**, 52–59 (2006).

[9] J. Y. Kim, N. L. Canfield, L. A. Chick, K. D. Meinhardt and V. L. Sprenkle. *Chromium Poisoning Effects on Various Cathodes.* Ceramic Engineering and Science Proceedings, **26**, 129 (2005).

[10] M. C. Tucker, H. Kurokawa, C. P. Jacobson, L. C. De Jonghe and S. J. Visco. *A fundamental study of chromium deposition on solid oxide fuel cell cathode materials.* J. Power Sources, **160**, 130–138 (2006).

[11] Y. D. Zhen, A. I. Y. Tok, S. P. Jiang and F. Y. C. Boey. *La(Ni,Fe)O_3 as a cathode material with high tolerance to chromium poisoning for solid oxide fuel cells.* J. Power Sources, **170**, 61–66 (2007).

[12] S. Jiang, J. Zhang and X. Zheng. *A comparative investigation of chromium deposition at air electrodes of solid oxide fuel cells.* Journal of the European Ceramic Society, **22**, 361–373 (2002).

[13] S. Jiang, S. Zhang and Y. Zhen. *Deposition of Cr Species at (La,Sr)(Co,Fe)O_3 Cathodes of Solid Oxide Fuel Cells.* J. Electrochem. Soc., **153**, A127–A134 (2006).

[14] T. Komatsu, H. Arai, R. Chiba, K. Nozawa, M. Arakawa and K. Sato. *Cr Poisoning Suppression in Solid Oxide Fuel Cells Using LaNi(Fe)O_3 Electrodes.* Electrochem. Solid-State Lett., **9**, A9–A12 (2006).

[15] S. Jiang. *Development of lanthanum strontium manganite perovskite cathode materials of solid oxide fuel cells: a review.* J. Mater. Sci., **43**, 6799–6833 (2008).

[16] G. Y. Lau, M. C. Tucker, C. P. Jacobson, S. J. Visco, S. H. Gleixner and L. C. DeJonghe. *Chromium Transport by Solid State Diffusion on Solid Oxide Fuel Cell Cathode.* J. Power Sources, **195**, 7540–7547 (2010).

[17] J. P. Ouweltjes, M. K. Stodolny and F. P. F. van Berkel. ECN Internal Communication (2008).

[18] N. Dekker, A. Janssen, G. Schoemakers and G. Rietveld. ECN Internal Communication (2006).

[19] M. Stanislowski, J. Froitzheim, L. Niewolak, W. Quadakkers, K. Hilpert, T. Markus and S. L. *Reduction of chromium vaporization from SOFC interconnectors by highly effective coatings.* Journal of Power Sources, **164**, 578–589 (2007).

[20] E. Konysheva, U. Seeling, A. Besmehn, L. Singheiser and K. Hilpert. *Chromium vaporization of the ferritic steel Crofer22APU and ODS Cr5Fe1Y_2O_3 alloy.* Journal of Materials Science, **42**, 5778–5784 (2007).

[21] W. Glatz and G. Kunschert. Electrochemical Society Proceedings, **1,**, 2005–07 (2005).

[22] K. Hilpert, D. Das, M. Miller, D. H. Peck and R. Weiss. *Chromium Vapor Species over Solid Oxide Fuel Cell Interconnect Materials and Their Potential for Degradation Processes.* J. Electrochem. Soc, **143**, 3642 (1996).

[23] S. Taniguchi, M. Kadowaki, H. Kawamura, T. Yasuo, Y. Akiyama, Y. Miyake and S. T. *Degradation phenomena in the cathode of a solid oxide fuel cell with an alloy separator.* J. Power Sources, **55**, 73 (1995).

[24] S. Badwal, R. Deller, K. Foger, Y. Ramprakash and J. Zhang. *Interaction between chromia forming alloy interconnects and air electrode of solid oxide fuel cells.* Solid State Ionics, **99**, 297–310 (1997).

[25] Y. Matsuzaki and I. Yasuda. *Electrochemical properties of a SOFC cathode in contact with a chromium-containing alloy separator.* Solid State Ionics, **132**, 271–278 (2000).

[26] M. Kornely, N. H. Neumann, A. amd Menzler, A. Leonide, A. Weber and E. Ivers-Tiffée. *Degradation of anode supported cell (ASC) performance by Cr-poisoning.* J. Power Sources, **196**, 7203–7208 (2011).

[27] E. Konysheva, H. Penkalla, E. Wessel, J. Mertens, U. Seeling, L. Singheiser and K. Hilpert. *Chromium Poisoning of Perovskite Cathodes by the ODS Alloy Cr5Fe1Y_2O_3 and the High Chromium Ferritic Steel Crofer22APU.* J. Electrochem. Soc., **153**, A765–A773 (2006).

[28] S. Paulson and V. Birss. *Chromium Poisoning of LSM-YSZ SOFC Cathodes I. Detailed Study of the Distribution of Chromium Species at a Porous, Single-Phase Cathode.* J. Electrochem. Soc., **151**, A1961–A1968 (2004).

[29] H. Yokokawa, T. Horita, N. Sakai, K. Yamaji, M. E. Brito, Y. P. Xiong and H. Kishimoto. *Thermodynamic considerations on Cr poisoning in SOFC cathodes.* Solid State Ionics, **177**, 3193–3198 (2006).

[30] J. Fergus. *Effect of cathode and electrolyte transport properties on chromium poisoning in solid oxide fuel cells.* Int. J. Hydrogen Energy, **32**, 3664–3671 (2007).

[31] S. Jiang and Y. D. Zhen. *Mechanism of Cr deposition and its application in the development of Cr-tolerant cathodes of solid oxide fuel cells.* Solid State Ionics, **179**, 1459 (2008).

[32] R. Chiba, F. Yoshimura and Y. Sakurai. *An investigation of $LaNi_{1-x}Fe_xO_3$ as a cathode material for solid oxide fuel cells.* Solid State Ionics, **124**, 281–288 (1999).

[33] M. K. Stodolny. *Chromium-Resistant Cathode and Cerium-Modified Perovskite Anode for Solid Oxide Fuel Cells.* Master's thesis, Gdansk University of Technology (2008).

[34] F. P. F. van Berkel, M. Stodólny, M. Sillessen and J. P. Ouweltjes. *Performance Optimisation of Chromium Resistant LNF Cathode.* Proceedings of the 8^{th} European Solid Oxide Fuel Cell Forum, **A0621**, 1–9 (2008).

[35] A. Le Bail, H. Duroy and J. L. Fourquet. *Ab-initio structure determination of $LiSbWO_6$ by X-ray powder diffraction.* Mat. Res. Bull., **23**, 447 (1988).

[36] C. J. Howard and B. A. Hunter. A Computer Program for Rietveld Analysis of X-Ray and Neutron Powder Diffraction Patterns, Lucas Heights Research Laboratories (1998).

[37] H. Falcón, A. E. Goeta, G. Punte and R. E. Carbonio. *Crystal Structure Refinement and Stability of $LaFe_xNi_{1-x}O_3$ Solid Solutions.* J. Solid State Chem., **133**, 379–385 (1997).

[38] T. Komatsu, H. Arai, R. Chiba, K. Nozawa, M. Arakawa and K. Sato. *Long-Term Chemical Stability of $LaNi(Fe)O_3$ as a Cathode Material in Solid Oxide Fuel Cells.* J. Electrochem. Soc., **154 (4)**, B379–B382 (2007).

[39] T. Hashimoto *et al. Analysis of crystal structure and phase transition of $LaCrO_3$ by various diffraction measurements.* Solid State Ionics, **132**, 183–190 (2000).

[40] R. D. Shannon. *Revised effective ionic radii and systematic studies of interatomic distances in halides and chalcogenides.* Acta Crystallogr., Sect. A: Cryst. Phys., Diffr., Theor. Gen. Crystallogr., **32**, 751–767 (1976).

[41] J. Cheng, A. Navrotsky, X. Zhou and H. U. Anderson. *Enthalpies of formation of $LaMO_3$ perovskites (M=Cr, Fe, Co, and Ni).* J. Mater. Res., **20 (1)**, 191–200 (2005).

[42] H. E. Höfer and R. Schmidberger. *Electronic Conductivity in the La(Cr,Ni)O_3 Perovskite System.* J. Electrochem. Soc., **141**, 782 (1994).

[43] M. C. Tucker. *Progress in metal-supported solid oxide fuel cells: A review.* J. Power Sources, **195**, 4570–4582 (2010).

[44] H. Orui, K. Watanabe, R. Chiba and M. Arakawa. *Application of LaNi(Fe)O_3 as SOFC Cathode.* Journal of The Electrochemical Society, **151 (9)**, A1412–A1417 (2004).

[45] M. K. Stodolny, F. P. F. van Berkel and B. A. Boukamp. *La(Ni,Fe)O_3 Stability in the Presence of Cr-Species – Solid State Reactivity Study.* ECS Transactions, **25 (2)**, 2915–2922 (2009). Chapter 2 of this thesis.

[46] M. K. Stodolny, B. A. Boukamp, D. H. A. Blank and F. P. F. van Berkel. *La(Ni,Fe)O_3 Stability in the Presence of Cr-Species – Solid State Reactivity Study.* J. Electrochem. Soc., **158 (2)**, B112 (2011). Chapter 2 of this thesis.

[47] J. P. Ouweltjes, M. van Tuel, M. Sillessen and G. Rietveld. *Redox Tolerant SOFC Anodes with High Electrochemical Performance.* Fuel Cells, **9**, 873 (2009).

[48] J. Chen, J. Rebello, V. Vashook, D. Trots, S. Wang, T. Wen, J. Zosel and U. Guth. *Thermal stability, oxygen non-stoichiometry and transport properties of $LaNi_{0.6}Fe_{0.4}O_3$.* Solid State Ionics, **192 (1)**, 424–430 (2011).

[49] W. Glatz, G. Kunschert and M. Janousek. *Proc. 6th European Solid Oxide Fuel Cell Forum.* In *M. Mogensen, Editor, European Fuel Cell Forum, Switzerland,* (2004).

[50] M. Abramoff, P. Magelhaes and S. Ram. *Image processing with ImageJ.* Biophoton. Int., **11**, 36 (2004).

[51] M. Bevilacqua, T. Montini, C. Tavagnacco, G. Vicario, P. Fornasiero and M. Graziani. *Influence of synthesis route on morphology and electrical properties of $LaNi_{0.6}Fe_{0.4}O_3$.* Solid State Ionics, **177**, 2957–2965 (2006).

[52] E. Konysheva and J. S. T. Irvine. *Electronic conductivity of modified $La_{0.95}Ni_{0.6}Fe_{0.4}O_{3-\delta}$ perovskites.* Journal of Power Sources, **193**, 175–179 (2009).

[53] R. Koc and H. U. Anderson. *Electrical and Thermal Transport Properties of (La,Ca)(Cr,Co)O_3.* Journal of the European Ceramic Society, **15**, 867–874 (1995).

[54] K. Iwasaki, T. Ito, M. Yoshino, T. Matsui, T. Nagasaki and Y. Arita. *Power factor of $La_{1-x}Sr_xFeO_3$ and $LaFe_{1-y}Ni_yO_3$.* Journal of Alloys and Compounds, **430**, 297–301 (2007).

[55] A. Berenov, E. Angeles, J. Rossiny, E. Raj, J. Kilner and A. Atkinson. *Structure and transport in rare-earth ferrates.* Solid State Ionics, **179**, 1090–1093 (2008).

[56] F. P. F. van Berkel, G. Schoemakers and G. Rietveld. ECN Internal Communication.

[57] I. Beszeda, D. L. Beke and Y. Kaganovskii. *Kinetics of growth and lateral spreading of a spinel layer around NiO particles on Al_2O_3 substrate.* Surface Science, **569(1-3)**, 5–11 (2004).

[58] R. T. Grimley, R. P. Burns and M. G. Inghram. *Thermodynamics of the Vaporization of Nickel Oxide.* J. Chem. Phys., **52(2)**, 551 (1961).

[59] G. R. Belton and A. S. Jordan. *The Gaseous Hydroxides of Cobalt and Nickel.* J. Phys. Chem., **71(12)**, 4114–4120 (1967).

[60] W. S. Chang, P. Shen and S. Chen. Materials Science and Engineering, **A148**, 145 (1991).

[61] S. Miyoshi and M. Martin. *B-Site cation diffusivity of Mn and Cr in perovskite-type $LaMnO_3$ with cation-deficit nonstoichiometry.* Phys. Chem. Chem. Phys., **11**, 3063 (2009).

[62] M. K. Stodolny, B. A. Boukamp, D. H. A. Blank and F. P. F. van Berkel. *Impact of Cr-poisoning on the conductivity of different $LaNi_{0.6}Fe_{0.4}O_3$ cathode microstructures.* Solid State Ionics, accepted for publication, DOI: 10.1016/j.ssi.2012.04.004. Chapter 4 of this thesis.

[63] M. K. Stodolny, F. P. F. van Berkel and B. A. Boukamp. *Impact of the Volatile Cr-species Attack on the Conductivity of La(Ni,Fe)O_3.* ECS Transactions, **35 (1)**, 2035–2043 (2011). Chapter 3 of this thesis.

[64] M. K. Stodolny, B. A. Boukamp, D. H. A. Blank and F. P. F. van Berkel. *Impact of Cr-poisoning on the conductivity of $LaNi_{0.6}Fe_{0.4}O_3$.* J. Power Sources, **196**, 9290–9298 (2011). Chapter 3 of this thesis.

[65] J. Montes, F. Cuevas and J. Cintas. *Porosity effect on the electrical conductivity of sintered powder compacts.* Appl. Phys. A„ **92**, 375 (2008).

[66] D. Pérez-Coll, E. Sánchez-López and G. C. Mather. *Influence of porosity on the bulk and grain-boundary electrical properties of Gd-doped ceria.* Solid State Ionics, **181**, 10331042 (2010).

[67] M. Nagata, Y. Itoh and H. Iwahara. *Dependence of observed overvoltages on the positioning of the reference electrode on the solid electrolyte.* Solid State Ionics, **67**, 215 (1994).

[68] F. van Berkel, F. van Heuveln and J. Huijsmans. *Characterization of solid oxide fuel cell electrodes by impedance spectroscopy and IV characteristics.* Solid State Ionics, **72**, 240 (1994).

[69] S. Adler. *Reference Electrode Placement in Thin Solid Electrolytes.* J. Electrochem. Soc., **149**, E166 (2002).

[70] J. Rutman and I. Riess. *Placement of reference electrode in solid electrolyte cells.* Electrochimica Acta, **52**, 6073–6083 (2007).

[71] E. Ivers-Tiffée, A. Weber, K. Schmid and V. Krebs. *Macroscale modeling of cathode formation in SOFC.* Solid State Ionics, **174**, 223232 (2004).

[72] J. Winkler, P. Hendriksen, N. Bonanos and M. Mogensen. *Geometric Requirements of Solid Electrolyte Cells with a Reference Electrode.* J. Electrochem. Soc., **145**, 1184 (1998).

[73] B. A. Boukamp. *A Nonlinear Least Squares Fit Procedure for Analysis of Immittance Data of Electrochemical Systems.* Solid State Ionics, **20 (1)**, 31–44 (1986).

[74] B. A. Boukamp. *A Package for Impedance/Admittance Data Analysis.* Solid State Ionics, **18&19**, 136–140 (1986).

[75] B. A. Boukamp. Equivalent Circuit (version 1.2), copyright 1985-2009, University of Twente/WisseQ.

[76] B. Boukamp and D. Blank. *High-precision impedance spectroscopy: a strategy demonstrated on PZT.* IEEE-TUFFC, **58 [12]**, 2521–2530 (2011).

[77] R. Chiba, Y. Tabata, T. Komatsu, H. Orui, K. Nozawa, M. Arakawa and H. Arai. *Property change of a $LaNi_{0.6}Fe_{0.4}O_3$ cathode in the initial current loading process and the influence of a ceria interlayer.* Solid State Ionics, **178**, 1701–1709 (2008).

[78] S. Adler, J. Lane and B. Steele. *Electrode Kinetics of Porous Mixed-Conducting Oxygen Electrodes.* J. Electrochem. Soc., **143 (11)**, 35543564 (1996).

[79] F. van Heuveln and H. Bouwmeester. *Electrode Properties of Sr-Doped $LaMnO_3$ on Yttria-Stabilized Zirconia II: Electrode kinetics.* Journal of Electrochemical Society, **144 (1)**, 135–140 (1997).

[80] S. Geng, Y. Li, Z. Ma, L. Wang, L. Li and F. Wang. *Evaluation of electrodeposited FeNi alloy on ferritic stainless steel solid oxide fuel cell interconnect.* Journal of Power Sources, **195**, 3345–3358 (2010).

[81] Z. Tianshu, P. Hing, H. Huang and J. Kilner. *Ionic conductivity in the CeO_2-Gd_2O_3 system (0.05⩽Gd/Ce⩽0.4) prepared by oxalate coprecipitation.* Solid State Ionics, **148**, 567–573 (2002).

[82] V. V. Kharton, A. A. Yaremchenko and E. N. Naumovich. *Research on the electrochemistry of oxygen ion conductors in the former Soviet Union. II. Perovskite-related oxides.* Journal of Solid State Electrochemistry, **3 (6)**, 303–326 (1999).

[83] M. Gazda, P. Jasinski, B. Kusz, B. Bochentyn, K. Gdula-Kasica, T. Lendze, W. Lewandowska-Iwaniak, A. Mielewczyk-Gryn and S. Molin. *Perovskites in Solid Oxide Fuel Cells.* Solid State Phenomena, **65**, 183 (2011).

[84] J. Chen, J. Rebello, V. Vashook, D. Trots, S. Wang, T. Wen, J. Zosel and U. Guth. *Thermal stability, oxygen non-stoichiometry and transport properties of $LaNi_{0.6}Fe_{0.4}O_3$.* Solid State Ionics, **192 (1)**, 424–430 (2011).

[85] J. Molenda, K. Świerczek and W. Zajac. *Functional materials for the IT-SOFC.* J. Power Sources, **173**, 657–670 (2007).

[86] A. Weber and E. Ivers-Tiffée. *Materials and concepts for solid oxide fuel cells (SOFCs) in stationary and mobile applications.* J. Power Sources, **127**, 273–283 (2004).

[87] M. K. Stodolny, B. A. Boukamp, D. H. A. Blank and F. P. F. van Berkel. *Cr-poisoning of a $LaNi_{0.6}Fe_{0.4}O_3$ cathode under current load.* J. Power Sources, **209C**, 120–129 (2012). Chapter 5 of this thesis.

Summary

This thesis deals with a study on the Cr-tolerance of the $LaNi_{0.6}Fe_{0.4}O_3$ (LNF) material. LNF is being considered for use as a current collecting layer, an interconnect protective coating and/or an electrochemically active solid oxide fuel cell (SOFC) cathode layer in an intermediate temperature IT-SOFC stack. The desired cost-effectiveness of the IT-SOFC systems can be achieved by using relatively cheap interconnect materials such as chromia forming ferritic stainless steels. However, the use of such interconnects triggers Cr-poisoning of the state-of-the-art SOFC cathodes, hence new Cr-tolerant materials are needed. The $LaNi_{0.6}Fe_{0.4}O_3$ material is considered as a promising candidate. Favorable properties of LNF, including high electronic conductivity, matched thermal expansion coefficient and claimed high Cr-resistance have encouraged studies described herein.

The research aim of this thesis is to understand the chemical stability of the $LaNi_{0.6}Fe_{0.4}O_3$ in the presence of Cr-species, which ultimately results in a thorough understanding of the degradation mechanisms of the LNF cathode under Cr-poisoning conditions. A final goal is to recommend feasible solutions to the Cr-poisoning issue. To meet these goals, firstly a solid-state reactivity between LNF and chromia is investigated in **Chapter 2**. Secondly, the influence of volatile Cr-species on the electrical properties of LNF is studied in **Chapter 3**. Thirdly, the impact of Cr-poisoning on the conductivity of different LNF microstructures is described in **Chapter 4**. Finally, Cr-poisoning of a $LaNi_{0.6}Fe_{0.4}O_3$ cathode under current load is discussed in **Chapter 5**. Last but not the least, recommendations for a feasible application of the LNF material in IT-SOFC systems are presented in **Chapter 6**.

Chapter 2 presents a solid-state reactivity study between LNF and chromia. It has been established that the LNF is chemically unstable at 800°C, when it is in direct solid-solid contact with Cr_2O_3. The main finding is that Cr-cations enter the perovskite phase, replacing first Ni- and then Fe-cations. As a consequence the perovskite transforms from a rhombohedral to an orthorhombic symmetry on the exchange of Ni and Fe with Cr. The stability of LNF in the presence of chromia improves significantly when the exposure temperature is lowered from 800°C to 600°C.

Chapter 3 deals with the effect of Cr substitution on the electrical properties of the LNF cathodes. In a simple experimental set-up it has been possible to clearly observe a detrimental impact of volatile Cr-species on the in-plane electronic conductivity of the $LaNi_{0.6}Fe_{0.4}O_3$ layer. The main finding of this research is that Cr-vapor species attack the porous LNF layer at the IT-SOFC operating temperatures (600-800°C). The Cr-attack results in a replacement of Ni by Cr in the LNF perovskite

lattice. Furthermore, the Cr-rich phase transforms from a rhombohedral to an orthorhombic crystal structure. The drop in the electronic conductivity of LNF is due to formation of a low conductive Cr-rich phase. It has been observed that the segregated Ni forms Ni-rich metal oxide particles in the pores. The Cr-poisoning impact on the LNF conductivity decline has been determined to be significantly smaller at 600°C than at 800°C.

Chapter 4 shows that Cr-poisoning, in terms of resistance increase and Cr accumulation, is more enhanced for LNF electrode microstructures with smaller particles and hence a larger surface area. In **Section 4.5** the rate of Cr-poisoning of the LNF layers is studied as a function of moisture and oxygen content in the supplied cathode gas. The results show the extreme impact of the humid conditions on the deterioration of the LNF conductivity due to enhanced Cr-poisoning. This emphasizes the need for moisture removal from the cathode gas stream.

Chapter 5 provides an insight into Cr-poisoning of an LNF cathode under current load. In order to unambiguously observe the degradation of the Cr-exposed LNF cathode under electrochemical operation, a sophisticated set-up is required. For reliable impedance studies it is essential that the electrodes have a very high degree of alignment. This has been obtained with a precise laser-ablation trimming of the edges of the electrodes. The major finding of this accelerated degradation study is the experimental observation that volatile Cr-species cause degradation in electrochemical performance of the LNF cathodes under current load conditions, resulting in an increase in cathode overpotential and impedance. The observed increase in both ohmic and polarization resistance can be attributed to the reaction of the $LaNi_{0.6}Fe_{0.4}O_3$-cathode and the $Gd_{0.4}Ce_{0.6}O_{1.8}$ (GDC)-barrier layer with Cr-species. The ohmic resistance increases due to both a drop in the LNF conductivity and a loss in the GDC ionic transport. The polarization resistance increases due to a loss of LNF electrochemical activity at the triple phase boundary.

Based on the experimental findings presented in **Chapters 2-5** of this thesis, it is possible to provide recommendations for a feasible application of the LNF material in IT-SOFC systems. **Chapter 6** contains such recommendations as a function of LNF microstructure, operating temperature, and concentration of Cr-species in the cathode gaseous environment. These parameters have been explored in the determination of the extent of Cr-tolerance of the LNF material. An optimum must be found in these parameters to enable successful implementation of the LNF material in IT-SOFC systems. Following the recommendations of **Sections 6.2-6.3** for the optimization of both operating conditions and LNF microstructure would allow successful non-electrochemical applications of LNF as a current collecting layer and/or an interconnect protective coating when used in combination with an Fe-Cr interconnect. The optimizations comprise: (*i*) Operating temperature should be lower than 800°C, preferably about 600°C; (*ii*) Gas atmosphere should be dry and gas should be provided at high velocities; (*iii*) LNF microstructure should be coarse. In order to provide recommendations for the use of LNF as an electrochemically active

cathode layer further experiments are necessary. **Chapter 5** reveals that it is not only the impact of Cr-species on the LNF-cathode that may negatively influence the electrochemical performance, but also the reactivity of Cr-species with the underlying GDC barrier layer. **Section 6.4** offers suggestions for reliable operation of an LNF cathode under realistic IT-SOFC stack conditions.

Based on the findings presented in this thesis it can be concluded that Cr-poisoning may not be fully avoidable in the IT-SOFC systems, where chromia forming ferritic stainless steels are used as interconnects. However, a synergetic approach may be undertaken in order to reduce the Cr-poisoning impact: From an operational perspective - the presence of volatile Cr-species should be minimized by applying interconnect protective coatings and providing dry air at high flow velocities. From an LNF microstructural perspective - the microstructure should be adjusted according to the application: a coarse microstructure is preferred for non-electrochemical use, i.e. as a current collecting layer and/or an interconnect protective coating, and a fine microstructure is the preferred choice for an electrochemically active cathode layer.

Samenvatting

In dit proefschrift wordt de Cr-tolerantie van het materiaal $LaNi_{0.6}Fe_{0.4}O_3$ (LNF) onderzocht. LNF wordt overwogen voor gebruik als stroomdistributie laag, als beschermende coating voor de scheidingsplaat (interconnect) en als elektrochemisch actieve kathode-laag in een vaste stof brandstofcel systeem met een verlaagde gebruikstemperatuur (IT-SOFC stack). De gewenste kostenvermindering van deze IT-SOFC systemen kan worden bereikt door het gebruik van relatief goedkope chroomoxide vormende ferritische, roestvaste staalsoorten als scheidingsplaat. Het gebruik van zulke scheidingsplaten veroorzaakt chroomvergiftiging in de 'state of the art' SOFC kathodes, daarom is er behoefte aan nieuwe Cr-tolerante materialen. $LaNi_{0.6}Fe_{0.4}O_3$ wordt beschouwd als een veelbelovend materiaal. De gunstige eigenschappen van LNF zoals hoge elektrische geleidbaarheid, gelijkwaardige thermische uitzettingscoëfficiënt, goede structurele stabiliteit en een vermeende hoge Cr-resistentie vormden de aanmoediging voor de in dit proefschrift beschreven studies.

De onderzoeksdoelstelling van dit proefschrift is een diepgaand begrip van de chemische stabiliteit van $LaNi_{0.6}Fe_{0.4}O_3$ in de aanwezigheid van Cr-species om te komen tot een gedegen kennis van het degradatiemechanisme van aan Cr-vergiftiging blootgestelde LNF kathodes. Het uiteindelijke doel is om tot bruikbare aanbevelingen te komen waarmee de Cr-vergiftiging kan worden geminimaliseerd. Om deze doelstellingen te bereiken wordt eerst in **Hoofdstuk 2** de reactiviteit tussen LNF en chroomoxide in de vaste stof fase bestudeerd. Vervolgens wordt in **Hoofdstuk 3** de invloed van gasvormige Cr-species op de elektrische geleiding van LNF onderzocht, waarna in **Hoofdstuk 4** de invloed van Cr-vergiftiging op verschillende LNF microstructuren wordt beschreven. Tenslotte wordt in **Hoofdstuk 5** het effect van Cr-vergiftiging op een $LaNi_{0.6}Fe_{0.4}O_3$ kathode onder stroomdoorvoer besproken. Uiteindelijk worden in **Hoofdstuk 6** aanbevelingen gedaan voor een bruikbare toepassing van het LNF materiaal in 'IT-SOFC' systemen.

In **Hoofdstuk 2** wordt de studie van de vaste stof reactiviteit tussen LNF en chroomoxide gepresenteerd. Er is vastgesteld dat LNF chemisch instabiel is wanneer het bij 800°C in direct contact wordt gebracht met Cr_2O_3. De belangrijkste observatie is dat Cr-kationen in de Perovskiet fase worden opgenomen waarbij eerst de Ni en vervolgens de Fe kationen worden vervangen. Als gevolg hiervan transformeert het Perovskietrooster van een rhomboëdrische naar een orthorhombische symmetrie door de uitwisseling van Ni en Fe met Cr. De stabiliteit van LNF in aanwezigheid van chroomoxide verbetert aanzienlijk wanneer de reactie temperatuur wordt verlaagd van 800°C naar 600°C.

Hoofdstuk 3 behandelt het effect van de Cr-substitutie op de elektrische geleidbaarheid van de LNF kathodes. Het was mogelijk om in een eenvoudige experimentele opstelling duidelijk de schadelijke invloed aan te tonen van vluchtige Cr-species op de laterale elektrische geleiding van een poreuze $LaNi_{0.6}Fe_{0.4}O_3$ laag. Het belangrijkste resultaat van dit onderzoek is dat gasvormige Cr-species de poreuze $LaNi_{0.6}Fe_{0.4}O_3$ laag aantasten over het gebied van werktemperaturen van de IT-SOFC (600-800°C). De Cr-aantasting resulteert in een vervanging van Ni door Cr in het LNF Perovskietrooster. Bovendien transformeert de Cr-rijke fase van een rhombodrische naar een orthorhombische kristalstructuur. De sterke verlaging van de elektrische geleiding van de LNF laag wordt veroorzaakt door de vorming van Cr-rijke fase met een lage elektronische geleidbaarheid. Ook werd gevonden dat het uitgescheiden nikkel Ni-rijke metaaloxide deeltjes in de poriën vormt. Tenslotte bleek dat de invloed van de Cr-vergiftiging op de LNF geleidingsafname duidelijk kleiner is bij 600°C dan bij 800°C. **Hoofdstuk 4** laat vervolgens zien dat Cr-vergiftiging, in termen van weerstandstoename en Cr ophoping, veel sterker is in LNF elektrodes met een microstructuur met kleinere deeltjes en dus een groter intern oppervlak. In **Sectie 4.5** werd de snelheid van de Cr-vergiftiging van de LNF lagen bestudeerd als functie van waterdamp- en van zuurstofconcentratie in de toegevoerde kathodegasstroom. De resultaten laten de extreme invloed van vochtigheid zien op de verslechtering van de geleidbaarheid van de LNF laag door een toegenomen Cr-vergiftiging. Dit toont duidelijk de noodzaak aan voor het verwijderen van vocht uit de kathodegasstroom.

Hoofdstuk 5 verschaft inzicht in de Cr-vergiftiging van een LNF kathode onder stroomdoorvoering. Om ondubbelzinnig de degradatie van een aan Cr-species blootgestelde LNF kathode tijdens elektrochemische belasting te volgen is een geavanceerde meetcel vereist. Voor een betrouwbare impedantie meting is het essentieel dat de elektroden ten opzichte van elkaar exact zijn uitgelijnd. Dit wordt bereikt door middel van een precieze laser ablatie bewerking van de randen van de elektrodes. De belangrijkste bevinding van deze versnelde degradatiestudie is dat vluchtige Cr-species de degradatie van de LNF kathodes tijdens stroomdoorvoer veroorzaken, resulterend in een toename van de kathode overpotentiaal en de impedantie. De waargenomen toename van de schijnbare elektrolytweerstand en polarisatieweerstand kan toegekend worden aan de reactie van de $LaNi_{0.6}Fe_{0.4}O_3$ kathode en $Gd_{0.4}Ce_{0.6}O_{1.8}$ (GDC) barri?re laag met de Cr-species. De schijnbare elektrolytweerstand neemt toe door zowel de afname in de geleidbaarheid van LNF als het verminderde zuurstofionen transport in de GDC laag. De polarisatieweerstand neemt toe ten gevolge van verlies van elektrochemische activiteit aan de driefasen grens.

Met behulp van de resultaten zoals gepresenteerd in **Hoofdstukken 2-5** van dit proefschrift is het mogelijk om aanbevelingen te geven voor een bruikbare toepassing van LNF in IT-SOFC systemen. In **Hoofdstuk 6** worden deze aanbevelingen gegeven in relatie tot de LNF microstructuur, gebruikstemperatuur en concentratie van Cr-species in het kathode gas. Deze parameters zijn onderzocht om te bepalen in welke mate het LNF materiaal Cr-tolerant is. Het vinden van een optimum voor deze parameters is nodig voor een succesvolle toepassing van LNF materialen in IT-

SOFC systemen. Opvolgen van de aanbevelingen in **Secties 6.2-6.3** zou succesvolle toepassing van LNF mogelijk moeten maken in niet-elektrochemische toepassingen zoals stroom distributie laag en/of beschermende coating in combinatie met een Fe-Cr scheidingsplaat. De optimalisatie omvat: (i) werktemperatuur moet lager zijn dan 800°C, bij voorkeur rond 600°C; (ii) gas atmosfeer moet droog zijn en een hoge doorvoersnelheid hebben; (iii) de LNF microstructuur moet grof zijn. Om tot aanbevelingen te komen voor het gebruik van LNF als elektrochemisch actieve kathodelaag zijn verdere experimenten nodig. In **Hoofdstuk 5** werd aangetoond dat Cr-species niet alleen een negatieve invloed hebben op de elektrochemische prestatie van de LNF kathode, maar dat deze ook reageren met de onderliggende GDC barriere laag. **Sectie 6.4** presenteert suggesties voor een betrouwbare werking van een LNF kathode onder realistische IT-SOFC stack condities.

Op basis van de in dit proefschrift gepresenteerde bevindingen kan worden geconcludeerd dat Cr-vergiftiging niet geheel te vermijden is in IT-SOFC systemen waarin chroomoxide vormend ferritische roestvaststaal wordt gebruikt als scheidingsplaat. Echter een synergetisch aanpak kan er voor zorgen dat de invloed van de Cr-vergiftiging zo veel mogelijk wordt gereduceerd: Ten aanzien van de bedrijfscondities verdient het aanbeveling de aanwezigheid van vluchtige Cr-species te verlagen door het toepassen van een beschermende coating op de scheidingsplaten en het gebruik van droge lucht met een hoge doorvoersnelheid. Ten aanzien van de LNF microstructuur verdient het aanbeveling deze aan te passen aan de de specifieke toepassing: bij voorkeur een grove microstructuur voor een beschermende coating en een stroomdistributielaag en een fijnkorrelige structuur voor de elektrochemisch actieve kathode laag.

Acknowledgements

When I look at my PhD in retrospect, now when all is neatly accomplished, it seems to be a great fascinating adventure!!!

However, during the last four years there were times, rough times, when my PhD was at stake.

For saving me and my work I wish to express my deepest gratitude to Frans - my supervisor, mentor and a good colleague at ECN.

Frans, thank you for maintaining faith in me and navigating me through the rough waters of the multiple ECN restructuring steps. I believe that owing to your words of wisdom towards our superiors it has been possible for me to finish this PhD successfully. Probably now you would smile on the thought of my persistence. But, I think, this persistence has been the key to finalize all the papers and it also added a lot of flavor to our scientific disputes. Our discussions were very fruitful indeed, though sometimes tough and fierce, but always inspiring to me - thanks a lot for your time, charisma, and a common way of thinking! *I wish you all the best.*

My PhD research at ECN was done in collaboration with UTwente. At IMS group I had close cooperation with Bernard Boukamp. Towards the end of the PhD my visits at Twente and meetings with Bernard intensified with a great outcome. Bernard, I wish to thank you for all these inspiring hours we talked, discussed and worked on the EIS data. You gave me a truly desired academia feeling regarding science. Thanks for that! Also, I would like to express my gratitude to Dave Blank for his supportive hand in times of troubles. Moreover, I wish to acknowledge my colleagues at IMS, especially Tomek and Nicolas, with whom I shared the SOFC passion.

My internship and the first year and a half of PhD remain in my memory as a time of undisturbed prosperity and joy in Petten. For this period I would like to thank especially Bert for the imparted trust, when he agreed on my stay at ECN (twice!). Also many thanks go to all ex-SOFC-ers: Mark, Ye, Frans, Marc, Jan Pieter, Loek, Guillaume, Alina, Pieter, Nico, Arno, Bart, Martin, Danny and Hans. The time we had together was simply brilliant! A nice example of the SOFC group spirit is the ongoing lunch club we still enjoy with Marc, Hans, Ye, Mark and Claire. This spirit extends well beyond the walls of the Institute:-) Thank you Claire for your delicious French cuisine. You know how much I enjoy eating and drinking at your place! Mark, I always enjoyed coffee breaks with your football stories! Ye thanks for

a nice cooperation within some projects. Ye and Mark, I appreciate a lot your support with my career-switch to Solar! Marc you were always my guru both in the lab and on the bike, keep it up! Jan Pieter thanks for your interesting genealogy stories and a valuable contribution to my papers. I also want to thank my office-mates: Alina and Guillaume, for the breathtaking traveling stories. Last but not the least: Hans! Honestly, I owe you an awful lot! Your precision and patience went hand in hand with my sophisticated experiments - thanks for your irreplaceable assistance. Hans, you made it possible to let my experiments run and at the same time to enjoy my beloved skiing, diving or traveling, business-related of course;-). Thanks also for bringing into my life a lot of technical novelties and funny stories. Your Friday's afternoon humor is always something to wait for! *Hartstikke bedankt!*

Adrien, you were my only and the best student. Thank you a lot for your dedication and unrivaled help in the lab. You used to joke that you were working with me and for me - both might be true indeed;-) I calm myself down it wasn't that bad as we still keep in touch. *Merci beaucoup!*

The great addition to the PhD work was the association of Jong-ECN with its multinational members. Through this network I met dozens of amazing young people! Countless outing for a beer, vodka, carting, pool, paintball, bowling, volleyball or football on the beach and so on felt like an extension of the party life from my studies in Gdańsk. Integration with Oranjes in Alkmaar was a wild pleasure. Our party team in the prosperity times counted even more than 40 people (memorable BBQ in Heiloo!). Here I would like to thank my closest friends: Raimo, Nicolas, Goulven, Tom and Ellen, Laurie and Manu, Gaga and BenH. The time spent with you guys has been and is always a great relaxation after work!!! Tom thanks for your colorful contribution to one of the important papers:)

After SOFC shutdown I joined HPCC and briefly SPT group. It was a great opportunity to meet new inspiring colleagues. For a warm welcome and exciting discussions that followed I wish to thank Soledad and Ozlem, Jan Wilco, Jean-Pierre, Eric, Li and Stephane. Further thanks go to Jurriaan, Saskia, Paul, Gerard, Daan, Henk and Marcel. For his native English fluency I'm grateful to Paul - now I'm certain my papers are more comprehensible to a wider audience. I wish to acknowledge Ruud and Yvonne for your ongoing support. With Wim, it seems, I had a kind of an intellectual agreement, saturated with a verbal skirmish, biting repartee, and still great scientific disputes. Thanks Wim for all that - it was a great time for me, hope you enjoyed as well;-)

I wish to thank all the people I had the pleasure to cooperated with. I sincerely acknowledge colleagues from ECN Engineering & Services: Erik, Marcel, Martijn, Gouwen, Marijke, and Peter. I wish to also thank Marcel and Carlo from Philips Innovation Services (MiPlaza). Many thanks go to Enrico from MESA+Institute NanoLab, University of Twente.

Chciałbym tutaj również podziękować naukowcom z Politechniki Gdańskiej za zaszczepienie we mnie pasji do ogniw paliwowych, dzięki czemu udało mi się trafić na wspaniały doktorat w renomowanym instytucie. Dziękuję serdecznie zwłaszcza Panu Kuszowi i Panu Jasińskiemu oraz ich bliskim współpracownikom. Specjalne podziękowania kieruję do Sebastiana, za pomoc w eksperymentach i za ciekawe dyskusje przez te wszystkie lata.

Kochani znajomi z Trójmiasta! Wydawać by się mogło, że dzielące nas ponad 1000 km będzie utrudniać naszą dalszą wspaniałą znajomość i przyjaźń z czasu studiów na PG. Jednak nie! Pokazaliśmy przez ostatnie 4 lata, że to żaden dystans dla naszej przyjaźni, wspólnych imprez i w Gdańsku i w Alkmaar, oraz dla planowania i uskuteczniania wojaży po świecie. Nasze naukowo-inżynierskie dyskusje nie ustały, a wręcz nabrały na sile pod wpływem nowych doznań na naszych doktoratach i w przemyśle. Staszku i Maju, Michale i Agatko, Jacku, Aniu - dziękuję Wam za to wszystko! Trzymam kciuki za Wasze doktoraty!!!

Podziękowania kieruję również dla naszej małej Polonii w Holandii: Magdy i Alicji. Dzięki za wiecznie wesołe dywagacje o sporach i nie tylko!

Najkochańsi Rodzice!!! Mamo Ewo, Tato Krzysiu!!!
Chciałbym Wam podziękować za tak wiele rzeczy!!! Dziękuję z całego serca za Waszą ogromną miłość! Dziękuję za wspaniałe i niezwykle umiejętne podejście do mnie, za moblizację i gratyfikację. Przez te wszystkie lata edukacji byliście wspaniałym wsparciem i ostoją spokoju dla mnie. Wasza ogromna wiara w moje możliwości i słowa otuchy były dla mnie najlepszym dopalaczem. *Dziękuję!*

Siostrzyczko! Kochana Moniu! Dziękuję za wszystko!!! *Jesteś najlepsza na świecie:)*

Kochane Babcie! Babciu Wandziu, Babciu Halinko! Wielki buziak za nieustające zainteresowanie moimi postępami i tymi naukowymi i tymi bardziej życiowymi. Dziekuję także za niesamowite wsparcie w czasach szkolno-studenckich! Sto lat!!!

Rodzicom Anety: Danucie i Leszkowi, Inusi, Arkowi i Asi pragnę serdecznie podziękować za szczere zainteresowanie moimi postępami naukowymi i nie tylko.

Kochanie, Anetko, Chrumciu! Dziękuję Ci za wspaniałe wsparcie i niewyobrażalną cierpliwość jaką mnie obdarzyłaś. Jestem Ci niezwykle wdzięczny za mobilizowanie mnie i przywoływanie do porządku, gdy tylko moje lenistwo zbytnio się ujawniało;p Dziękuję za Twoją wizję Latexa i jej wdrożenie w życie - oczywiście odpracuję;-) Dziekuję też za pomoc w dopinaniu wszystkich szczegółików tej książki na ostatni guziczek! Bawiły mnie bardzo nasze naukowe dysputy i dzielenie się doświadczeniami doktoranckimi. Życzę Ci abyś w przeciągu roku pisała te same słowa wieńczące Twoją rozprawę doktorską !!!

Maciej Stodolny, Alkmaar, April 2012

About the author

Maciej Krzysztof Stodólny was born in Sokółka, North-East Poland in 1984. After four years the family moved to Inowrocław, North-Central Poland, where he spent his childhood and attended primary school. In 2003 Maciej graduated with honors from Secondary School no.1 in Inowrocław in mathematics-physics class with advanced English. He bet on physics and studied at Gdańsk University of Technology on the Faculty of Applied Physics and Mathematics for 5 years. During his student times he did several scientific internships. The first was at University of Science and Technology, Faculty of Materials Science and Ceramics in Kraków, Poland. The second was at Italian National Agency for New Technologies, Energy and the Environment, ENEA in Casaccia, Italy. Maciej did his final internship at the Energy research Centre of the Netherlands (ECN). The latter visit gave him the opportunity for a PhD contract at ECN. In 2008 Maciej received his M.Sc. degree cum laude in Applied Physics. He obtained Best M.Sc. Dissertation Award from Polish Hydrogen and Fuel Cell Association for his work on the SOFC electrodes optimization. In 2008 he started his PhD research at ECN within Hydrogen and Clean Fossil Fuels unit in the SOFC group in cooperation with the Inorganic Materials Science group, Department of Science and Technology, MESA+ Institute for Nanotechnology at the University of Twente, the Netherlands. His PhD thesis dealt with Cr-tolerance of the La(Ni,Fe)O_3 material in the SOFC applications. In March 2012 Maciej obtained a permanent position as a Solid State Physicist/Material Scientist at the ECN Solar Energy unit in the Silicon-Photovoltaics Device Architecture group.